The University of Manchester

THEORY AND MODELLING OF ELECTROLYTES AND CHAIN MOLECULES

A THESIS
SUBMITTED TO THE UNIVERSITY OF MANCHESTER
FOR THE DEGREE OF
DOCTOR OF PHILOSOPHY (PHD)
IN THE FACULTY OF ENGINEERING AND PHYSICAL SCIENCES

MING LI

SCHOOL OF CHEMICAL ENGINEERING AND ANALYTICAL SCIENCE
2011

CONTENTS

Final word count: 37,658

LIST OF FIGURES

LIST OF TABLES

ABSTRACT

An aqueous solution of electrolytes can be modelled simplistically as charged hard spheres dispersed in a dielectric continuum. We review various classical theories for hard sphere systems including the Percus-Yevick theory, the mean spherical approximation, the Debye-Hückel theory and the hyper-netted chain theory, and we compare the predictions of the theories with simulation results.

The statistical associating fluid theory (SAFT) has proved to be accurate for neutral polymers. It is modified to cope with charged polyelectrolyte systems. A chain term for the charged reference fluid is introduced into the theory. Some well-established results are reproduced in this study and we also introduce new terms and discuss their effects. The results show that the SAFT is semi-quantitatively correct in predicting the phase behaviour of polyelectrolytes.

The electrostatic attraction between unlike charged particles at low temperature is very strong. The short-range attractions between unlike pairs are treated via an association theory while the remaining interactions are handled by hypernetted chain theory. This method works quite well with multiple associating sites. The phase prediction for the size and charge symmetric restricted primitive model is quantitatively correct as compared with simulation results. Furthermore, it also gives semi-quantitatively correct predictions for the phase behaviour of size- and charge-asymmetric cases.

Dissipative particle dynamics (DPD) is a powerful simulation technique for mesoscopic systems. Molecules with specific shapes (rods and spheres) are simulated using this technique. By tuning the density of the system, some liquid crystal phase transitions can be observed. The properties of spider silk fibroin are also modelled by DPD, indicating a possible route of forming spider silk.

DECLARATION

The University of Manchester

PhD by published work Candidate Declaration

Candidate Name: Ming Li

Faculty: Engineering and Physical Sciences

Thesis Title: Theory and Modelling of Electrolytes and Chain Molecules

Declaration to be completed by the candidate:

I declare that no portion of this work referred to in this thesis has been submitted in support of an application for another degree or qualification of this or any other university or other institute of learning.

Signed: Date: September 22, 2011

COPYRIGHT

ACKNOWLEDGMENTS

This thesis would not have been possible without the supervision and the support from my supervisor, Professor Andrew J. Masters. I would like to thank Andrew for his guidance in this project as well as for showing me the rigorous research attitude. This attitude will benefit me much more than this thesis itself.

I would also like to offer my gratitude to several individuals who helped me during this project:

Dr. Leo Lue and Dr. Robin Curtis, for discussing with me and giving me great suggestion about polyelectrolyte theories and about general statistical mechanics.

Dr. Patrick B. Warren, my industrial supervisor, for giving me in-depth view about the R&D in industry and also great helps in understanding the physics of electrolytes and dissipative particle dynamics.

Dr. James Magee, for the helpful discussion about coding and for the shared interest in modelling of the mafia game.

Dr. Ben Embley, Dr. Matthew Dennison and Dr. Marcus Bannerman, for all sorts of interesting discussions and sport/social events they have arranged.

Dr. Argyrios Karatrantos and Ms. Dorota Roberts, for all the cooperations and discussions about the project.

Mr. Tom Rodgers, Mr. James Winterburn, Mr. Robert Sargant and everyone else in the MMS group and in office C19.

I would like to thank Marie Curie European Commission for providing the financial support for the project.

Last but not least, I want to give my thanks to my parents and my girlfriend for all their supports during my study, as well as to all my supportive friends.

CHAPTER

ONE

INTRODUCTION

A polyelectrolyte is a special type of polymer in which the repeating units bear an ionisable group. The ionisable group dissociates in aqueous solutions and therefore makes the polymer charged. Because of this, polyelectrolytes have quite different properties to non-charged polymers. Polypeptides (and thus all proteins) and DNA are all polyelectrolytes. Together with many other synthetic ones (such as polyacrylic acid and poly(sodium-styrene-sulphonate)), polyelectrolytes are used in a variety of industries.

The thermodynamic properties of polyelectrolyte solutions have been widely studied experimentally but the theoretical understanding is still quite limited. Current computer simulation results also show discrepancies with the theoretical predictions. The aim of this research is to find better theoretical descriptions for both electrolytes and polyelectrolytes.

Many polyelectrolyte theories have, as a basis, an electrolyte theory. Extra perturbation terms are then added to describe the formation of chains. However, current theoretical predictions for electrolyte systems show large deviations from Monte-Carlo simulation results for the restricted primitive model(RPM). Therefore we are looking for a new theory to better describe hard sphere electrolyte systems. After reviewing the classical fluid theories for hard spheres, we choose Wertheim's association theory plus the hypernetted chain equations to build up our theory for electrolytes. The association theory works particularly well with short-ranged strong attractions. The hypernetted chain theory gives generally good descriptions of fluid systems. By combining the two, we generate our own association theory.

Statistical Association Fluid Theory (SAFT) is quite a new fluid theory which well describes the solution behaviour of neutral polymers. It is a theory which takes account of every type of interaction in solution on a statistical mechanical basis. This theory shows good consistency

for neutral polymers. Some researchers have developed an additional electrostatic term to make SAFT effective for polyelectrolytes. We have also applied such a theory to the study of polyelectrolytes. In addition, some modifications and implementations have been made for a better description of the charged system. The results are compared with those from Monte-Carlo simulations.

We also performed some simulation studies based on Dissipative Particle Dynamics (DPD) for colloids. This work was started during an industrial placement and was subsequently pursued as part of this thesis. One aim of this work was to study the phase behaviour of binary mixtures of rods and spheres. It is, of course, possible to study this system using hard particle models, but, especially at one high density, equilibration becomes a serious problem. As DPD particles interact via a soft repulsive potential, considerably more movement of the particles is possible at these high densities and equilibration problems are considerably less severe. By tuning the interaction parameters, some liquid crystal phase transitions are observed. We have also modelled systems consisting of soft and hard segments (as di-block, tri-block or multi-block copolymers). The simulation results indicate a possible route for the formation of the spider silk from fibroins.

CHAPTER

TWO

SIMULATION METHODS AND CONDITIONS

In this thesis, hard sphere systems with different inter molecular potentials are simulated using standard Monte-Carlo techniques [1]. Throughout the whole thesis we compare our own simulation results with the theoretical predictions unless otherwise stated.

2.1 Canonical Ensemble

A canonical ensemble is a collection of systems having the same number of particles (N), volume (V) and temperature (T), which is often referred as an NVT ensemble. The equilibrium probability density for a classical system of identical, spherical particles is

$$f^{(N)}(\mathbf{r}^N, \mathbf{p}^N) = \frac{1}{h^{3N} N!} \frac{\exp(-\beta \mathbf{H})}{Q_N} \tag{2.1.1}$$

where, $\mathbf{r}^N \equiv \mathbf{r_1}, \ldots, \mathbf{r_N}$ represents the $3N$ positional coordinates and $\mathbf{p}^N \equiv \mathbf{p_1}, \ldots, \mathbf{p_N}$ specifies the $3N$ momenta of all N particles in the system. h is Planck's constant, $\beta = (k_B T)^{-1}$ is the inverse temperature, where k_B is Boltzmann's constant and T is the temperature. $\mathbf{H}$ is the the Hamiltonian of the system, which includes the kinetic energy and inter molecular interactions for the system. We do not consider any external fields.

Q_N is the canonical partition function, defined by

$$Q_N = \frac{1}{h^{3N} N!} \iint \exp(-\beta \mathbf{H}) \, \mathrm{d}\mathbf{r}^N \, \mathrm{d}\mathbf{p}^N \tag{2.1.2}$$

By integrating $f^{(N)}(\mathbf{r}^N, \mathbf{p}^N)$ over all possible momenta, one obtains the N-particle positional

probability density, $\rho^{(N)}(\mathbf{r}^N)$. This is given by

$$\rho^{(N)}(\mathbf{r}^N) = \frac{1}{h^{3N}N!}\frac{\exp(-\beta V(\mathbf{r}^N))}{Z_N} \tag{2.1.3}$$

where $V(\mathbf{r}^N)$ is the potential energy of the system and Z_N is the configurational integral

$$Z_N = \frac{1}{h^{3N}N!}\int \exp(-\beta V(\mathbf{r}^N))\,\mathrm{d}\mathbf{r}^N \tag{2.1.4}$$

All non-ideal contributions to the thermodynamic variables are given in terms of $\rho^{(N)}$ and Z_N, and it is these upon which we focus.

2.2 Monte-Carlo Simulation

The standard Monte-Carlo simulation technique in an NVT ensemble is as follows:

1. For a given state (m) of the system, calculate the total potential energy, $V_N(m)$
2. Make a random displacement of a particle and calculate the new total potential energy at this new state (n), $V_N(n)$
3. If $V_N(n) \leq V_N(m)$, the trial move is accepted. Otherwise it is accepted with a probability of $\exp(-\beta\Delta V_N)$, where $\Delta V_N = V_N(n) - V_N(m)$.
4. Return to Step 1.

This practice was first proposed and proved in the paper by Metropolis et. al [2]. This algorithm produces a distribution of states corresponding to Eq.(2.1.3). where we can ensure at equilibrium, the energy states in the simulation system corresponds to the probability density distribution given in Eq.(2.1.1).

2.3 Simulation Parameters

In our simulations, 512 particles with unit diameter are used to simulate the restricted primitive model (RPM) in the NVT ensemble. For different system densities, we vary the length of

the cubic box but keep the total number of particles constant. Periodic boundary condition is used to simulate the bulk fluid[1].

All the simulation results are based on 1 million sweeps. A sweep means one attempted trial move per particle for each particle in the box. Therefore all the Monte-Carlo simulation results are based on 512 million trial moves.

For hard sphere particles, the trial move will be rejected if the two particles overlap, i.e. if

$$r_{ij} < (\sigma_i + \sigma_j)/2 \tag{2.3.1}$$

where r_{ij} is the distance between the centres of particle i and j, σ_i is the diameter of particle i. For pure hard sphere systems, this is the only criterion for the trial moves. For systems with more general inter-particle potentials, the trial moves are accepted/rejected on the basis of the system energy change as described in the previous section.

2.4 References

[1] M.P. Allen and D.J. Tildesley. *Computer Simulation of Liquids*. Clarendon Press, Oxford, 2002. See pp. 17, 19.

[2] N. Metropolis et al. “Equation of State Calculations by Fast Computing Machines”. In: *The Journal of Chemical Physics* 21 (1953), pp. 1087–1092. See p. 18.

CHAPTER

THREE

THEORIES FOR HARD SPHERE SYSTEMS

3.1 Introduction

The study of monomer systems forms the theoretical basis for the study of polymers. In this chapter, some classical distribution function theories of liquids are reviewed. The results from the theoretical calculations are compared with Monte-Carlo simulation results for hard sphere systems. In addition, these theories are applied to more complicated primitive models. Their advantages and disadvantages are discussed.

3.2 Distribution Function Theories and Integral Equations

In statistical mechanics, the equilibrium probability densities and molecular distribution functions are of great importance in describing the thermodynamic properties. We consider a simple liquid system composed of a homogeneous, isotropic mixture of particles that interact via spherically-symmetric potentials. A starting point is the Ornstein-Zernike equation, which is given by [1]

$$h_{ij}(r_{12}) - c_{ij}(r_{12}) = \int \sum_k c_{ik}(r_{13}) \rho_k h_{kj}(r_{32}) \, \mathrm{d}\mathbf{r_3} \tag{3.2.1}$$

$c_{ij}(r)$ is the direct correlation function. $h_{ij}(r)$ is the pair correlation function given by

$$h_{ij}(r) = g_{ij}(r) - 1 \tag{3.2.2}$$

and $g_{ij}(r)$ is the radial distribution function. The subscripts i, j and k label the different species in the system. ρ_k is the number density of species k. The Ornstein-Zernike equation describes the pair correlation function between two particles (e.g. 1 and 2) as being partly due to their direct correlation and also via correlations mediated by the intermediate particles (e.g.$3, 4 \ldots$). For an isotropic and translational invariant system, the Ornstein-Zernike equation for a one-component fluid can be simplified to [1]

$$h(r) - c(r) = \rho \int c(|r - r'|)h(r')\,\mathrm{d}\mathbf{r'} \tag{3.2.3}$$

Taking the Fourier Transformation of both sides of Eq. (3.2.3), we can get the Ornstein-Zernike equation in k-space:

$$\hat{h}(k) - \hat{c}(k) = \rho\hat{h}(k)\hat{c}(k) \tag{3.2.4}$$

Eq. (3.2.4) gives a simple relation between $\hat{c}(k)$ and $\hat{h}(k)$. If the direct correlation function is known, the pair correlation function and other structure-related functions can be easily calculated. If, as is normally the case, the direct correlation function is not known, a second relationship between $h(r)$ and $c(r)$ is required. This is normally called a closure relation. In order to solve Ornstein-Zernike equation which contains two unknowns ($h(r)$ and $c(r)$), one more closure relation is needed. Different closures will be discussed in the following sections.

In the following sections, we consider a pair potential given by

$$u_{ij}(r) = u_{ij}^{(0)}(r) + w_{ij}(r) \tag{3.2.5}$$

where i and j represent the species of the particles, $u_{ij}^{(0)}(r)$ is the reference pair potential, $w_{ij}(r)$ is the additional pair potential and $u_{ij}(r)$ is the total pair potential.

3.2.1 Hard Sphere System and the Percus-Yevick Solution

The hard sphere model has been widely studied [2]. Here we assume all the particles have the same diameter σ, and therefore the inter-particle potential is defined by:

$$u^{hs}(r) = \begin{cases} +\infty & r < \sigma \\ 0 & r > \sigma \end{cases} \tag{3.2.6}$$

An advantage of this approximation is that the Percus-Yevick (PY) closure with a pair potential $u(r)$ shown below can be solved analytically [1, 3]. In general, the PY closure for a one-component system can be written as

$$c(r) = g(r) - \exp(\beta u(r))g(r) = f(r)y(r) \tag{3.2.7}$$

Here $f(r) = \exp(-\beta u(r)) - 1$ is the Mayer-f function and $y(r) = g(r)\exp(\beta u(r))$ is the cavity correlation function. Again, $\beta = 1/k_B T$ is the inverse thermodynamic energy, where T is the absolute temperature and k_B is Boltzmann's constant. For the hard sphere potential, the PY closure takes the form

$$g(r) = 0, \qquad r < \sigma \tag{3.2.8}$$

$$c(r) = 0, \qquad r > \sigma \tag{3.2.9}$$

This, combining with the Ornstein-Zernike relation (3.2.3), gives two equations for two unknowns.

Thiele [4] and Wertheim [5] have independently given the solution for the Percus-Yevick approximation and the result for the direct correlation function is:

$$c(x) = \begin{cases} -\lambda_1 - 6\eta\lambda_2 x - \frac{1}{2}\eta\lambda_1 x^3 & x < 1 \\ 0 & x > 1 \end{cases} \tag{3.2.10}$$

where $x = r/\sigma$ and $\eta = \pi\rho\sigma^3/6$ is the packing fraction, meaning the proportion of the total

volume occupied by the particles. The two parameters λ_1 and λ_2 are defined as:

$$\lambda_1 = (1+2\eta)^2/(1-\eta)^4 \tag{3.2.11}$$

$$\lambda_2 = -(1+\frac{1}{2}\eta)^2/(1-\eta)^4 \tag{3.2.12}$$

The results of the Percus-Yevick approximation can be used to generate two equations of state, the compressibility equation and the virial equation [1, 4]. These are

$$\frac{\beta P^c}{\rho} = \frac{1+\eta+\eta^2}{(1-\eta)^3} \tag{3.2.13}$$

$$\frac{\beta P^v}{\rho} = \frac{1+2\eta+3\eta^2}{(1-\eta)^2} \tag{3.2.14}$$

where P^c is the pressure calculated using the compressibility route and P^v is the pressure according to the virial route.

The difference between the two calculation routes is due to the approximate nature of the Percus-Yevick equations. Further study [6] shows that the accurate Carnahan-Starling equation hard sphere of state is obtained by adding $\frac{2}{3}$ of Eq.(3.2.13) and $\frac{1}{3}$ of Eq.(3.2.14):

$$\begin{aligned}\frac{\beta P}{\rho} &= \frac{2}{3}\frac{\beta P^c}{\rho} + \frac{1}{3}\frac{\beta P^v}{\rho} \\ &= \frac{1+\eta+\eta^2-\eta^3}{(1-\eta)^3}\end{aligned} \tag{3.2.15}$$

These approaches may also be applied to hard sphere mixture, given as the Boublík-Mansoori-Carnahan-Starling-Leland (BMCSL) [7, 8] equation.

3.2.2 Mean Spherical Approximation

The mean spherical approximation (MSA) applies to hard sphere particles with an additional interaction [1, 9]. The MSA closure is written as

$$g(r) = 0, \qquad r < \sigma \tag{3.2.16}$$

$$c(r) = -\beta w(r), \qquad r > \sigma \tag{3.2.17}$$

It is obvious that Eq.(3.2.16) is an exact relation for hard spheres. Eq.(3.2.17) is clearly a significant approximation. Supplemented by the Ornstein-Zernike equation, the biggest benefit of MSA is that it can be solved analytically for various interactions, such as charged hard-sphere systems. A special case of the MSA is the pure hard sphere system where $w_{ij} = 0$. The MSA approximation then becomes the Percus-Yevick approximation, and, as described in Section3.2.1, there exists an analytical solution.

With such a benefit, MSA plays an important part in hard sphere systems where particles have long-range interactions, e.g. electrostatic interactions. This will be discussed in later chapters.

3.2.3 Hypernetted Chain

The Hypernetted Chain (HNC) approximation is often derived via diagrammatic expansions of the pair functions [1, 9]. The closure may be written as:

$$c(r) = -\beta u(r) + h(r) - \log(h(r) + 1) \tag{3.2.18}$$

Rearranging Eq.(3.2.18) and taking the exponential on both sides, we get:

$$g(r) = \exp(h(r) - c(r) - \beta u(r)) \tag{3.2.19}$$

HNC has been widely used in the study of various systems, especially the one component plasma [10], but for the pure hard sphere system, it is not as accurate as the Percus-Yevick approximation. If we expand the term $\log(h(r) + 1)$ in a Taylor series and set $u(r) = 0$ for $r > \sigma$, we find:

$$c(r) = \sum_{i=2}^{\infty} \frac{(-1)^{(i-1)} h^i(r)}{i} = -\frac{h^2(r)}{2} + \frac{h^3(r)}{3} + \ldots, \qquad r > \sigma \tag{3.2.20}$$

At low densities, $h(r) \to 0$ outside the hard core as the RHS of Eq. (3.2.20) tends to zero, which equals the Percus-Yevick equations. However this tiny tail resulted from the logarithmic term in Eq.(3.2.18) generates a significant difference at high densities. Another disadvantage of HNC is that its solutions are highly numerical, unlike MSA which could be solved analytically. A final problem is that occasionaly no real solution existes to the HNC equations, even in physically

reasonable situations.

3.2.4 Results and Discussions for Pure Hard Sphere Systems

Here we compare the results from different theories with the "exact" results from Monte-Carlo simulation. Our Monte-Carlo results are consistent with Ref.[2]. Fig. (3.1) shows that at low densities, both HNC and PY predict the radial distribution function quite well. At low densities, the RHS of Eq. (3.2.20) is small, since we are approaching an ideal gas limit for which $h(r) = 0(r > \sigma)$, and the HNC corresponds to PY. However, when the density goes up, the discrepancies between the three routes become big. Fig. (3.2) shows clearly that at a high density $\rho^* = 0.8$, the MSA underestimates the first peak of the radial distribution function while HNC does the opposite. In a pure hard sphere system, the value of $g(\sigma)$ is directly related to the virial-route pressure, so the underestimate of the first peak leads to errors. On the other hand, the HNC tail given in Eq. (3.2.20) effectively strengthens the first peak, but overestimates it.

Another defect of HNC is that the oscillations of $g(r)$ are out of phase with MC results. The oscillation decreases much faster than MC result. As a contrast, $g(r)$ from MSA is in line with MC results.

Fig. (3.3) shows the significant difference of the total pressure given by different routes. The Carnahan-Starling equation is in a very good agreement with the real Monte-Carlo simulations [1] (not shown in the figure). Either MSA or HNC gives a poor prediction at high densities due to the discrepancies in $g(r)$.

3.3 Binary Hard Sphere Electrolytes and the Restricted Primitive Model (RPM)

Electrolytes are a special type of system as the constituent particles interact via a long-ranged electrostatic interaction. People have been studying the theory of electrolytes for over a century but the results are only qualitatively or semi-quantitatively correct [11, 12]. The most widely studied electrolyte model is the Restricted Primitive Model (RPM) [12]. In this model, the particles are described as hard spheres with an identical diameter σ and either a positive elementary charge $(+e)$ or a negative elementary charge $(-e)$. The solvent is modelled as a

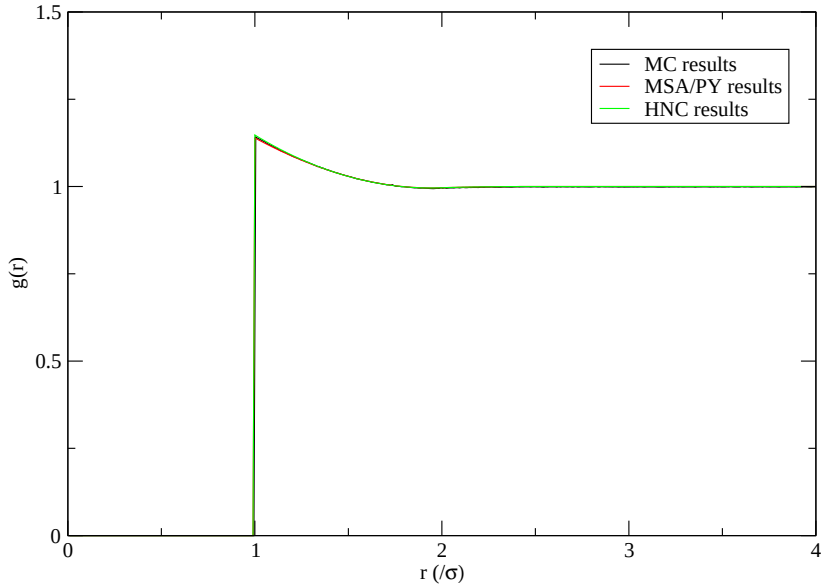

Figure 3.1: Radial distribution function given by Monte-Carlo simulation, Mean Spherical Approximation and Hypernetted Chain for a pure hard sphere system with a reduced density $\rho^* = \rho\sigma^3 = 0.1$.

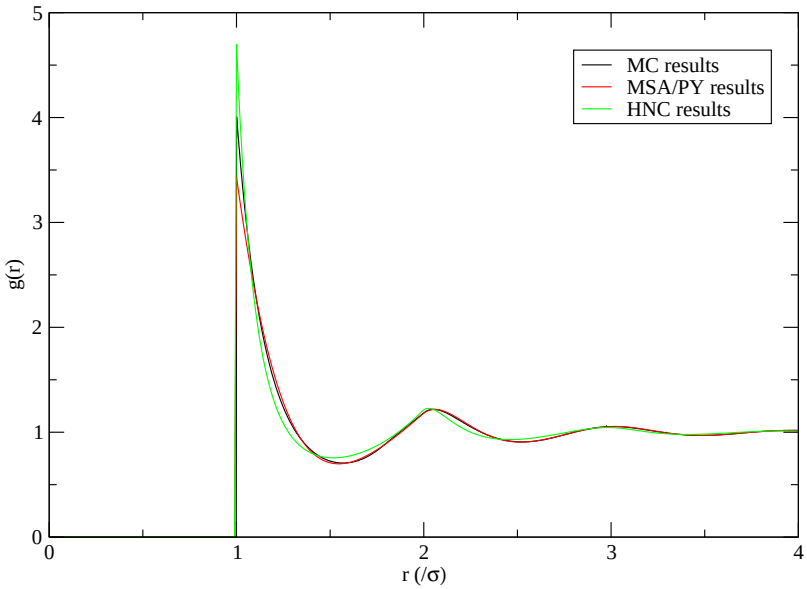

Figure 3.2: Radial distribution function given by Monte-Carlo simulation, Mean Spherical Approximation and Hypernetted Chain for a pure hard sphere system with a reduced density $\rho^* = \rho\sigma^3 = 0.8$

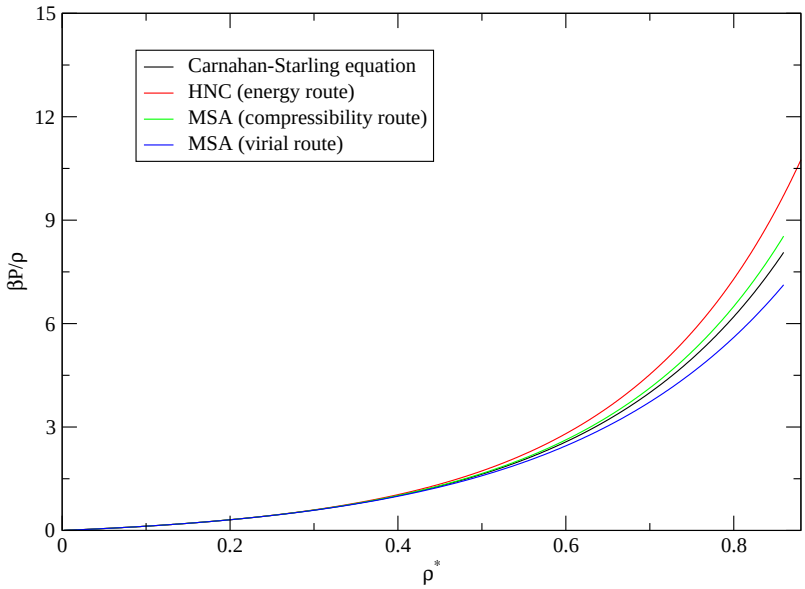

Figure 3.3: Total pressure given by Mean Spherical Approximation (virial route and compressibility route), Hypernetted Chain and Carnahan-Starling equation for pure hard sphere systems, $\rho^* = \rho\sigma^3$.

homogeneous dielectric continuum with a dielectric constant of ϵ. One key factor in the RPM model is the Bjerrum length [12], defined as:

$$l_B = \frac{\beta e^2}{\epsilon} \tag{3.3.1}$$

The physical meaning of the Bjerrum length is that it is the distance at which the electrostatic interaction is equal to the thermal energy $k_B T$. Hence, the pair potential between two particles 1 and 2 is described as:

$$\beta u_{ij}(r_{12}) = \begin{cases} +\infty, & r_{12} < \sigma \\ \frac{z_i z_j l_B}{r_{12}}, & r_{12} > \sigma \end{cases} \tag{3.3.2}$$

where z_i is the charge number for species i (either $+1$ or -1).

The first theory of the RPM was given by Debye and Hückel (DH) [11] which gives quite good agreement with 'real' experimental results for dilute solutions. The theory first clearly described the effect of electrostatic screening and has been extended by other researchers [12].

3.3.1 The Debye-Hückel (DH) Theory

Starting with an RPM model, the electrostatic neutrality condition gives:

$$\rho_+ = \rho_- = \rho/2 \tag{3.3.3}$$

where ρ_+ and ρ_- are the number densities of the $+$ and $-$ ions respectively, and ρ is the total number density.

Again, each electrolyte carries a charge that equals to $\pm q,\ (q = ze)$. In the case of no external fields, the electrostatic potential $\Phi(r)$, about an ion fixed at the origin, satisfies the Poisson equation

$$\bigtriangledown^2\ \Phi(r) = -\frac{4\pi}{\epsilon}\rho_e(r) \tag{3.3.4}$$

where $\rho_e(r)$ is the charge density at a distance r. The effective charge density in the system can be given in terms of the radial distribution functions $g_{ij}(r)$, where in the RPM model we have $g_{++}(r) = g_{--}(r)$ and $g_{+-}(r) = g_{-+}(r)$. Thus for a central positive ion,

$$\rho_{\mathbf{e}}(r) = \frac{\rho q(g_{++}(r) - g_{+-}(r))}{2} \tag{3.3.5}$$

The radial distribution functions can be written in terms of the potential of mean force $w_{ij}^f(r)$, viz

$$g_{ij}(r) = \exp(-\beta w_{ij}^f(r)) \tag{3.3.6}$$

where the potential of mean force represents the total work needed to bring ions i and j from infinity to a separation of r. Debye and Hückel made the approximation

$$w_{ij}^f(r) = q_j\Phi_i(r) \tag{3.3.7}$$

$\Phi_i(r)$ is defined as the electrostatic potential as distance r from ion i fixed at the origin $r = 0$.

With this approximation, Debye and Hückel obtained the Poisson-Boltzmann equation

$$\bigtriangledown^2 \Phi = \frac{4\pi\rho q}{\epsilon} \sinh(\beta q \Phi) \tag{3.3.8}$$

If we only consider situations in which $\beta q\Phi \ll 1$, Eq. (3.3.8) can be linearised to give

$$\bigtriangledown^2 \Phi(r) = \kappa_{\mathbf{D}}^2 \Phi(r) \tag{3.3.9}$$

$$\kappa_{\mathbf{D}} = \sqrt{4\pi l_B \rho} \tag{3.3.10}$$

where $\kappa_{\mathbf{D}}$ is called the inverse Debye length, and plays an important role in the theory of electrostatic systems.

After some mathematics, the electrostatic potential inside the core is found to be

$$\Phi(r) = \frac{q}{\epsilon r} - \frac{q\kappa_{\mathbf{D}}}{\epsilon(1+\kappa_{\mathbf{D}}\sigma)}, r < \sigma \tag{3.3.11}$$

and outside, it is expressed as:

$$\Phi(r) = \frac{q\theta(\kappa_{\mathbf{D}}\sigma)\exp(-\kappa_{\mathbf{D}} r)}{\epsilon r}, r > \sigma \tag{3.3.12}$$

where $\theta(x) = \frac{\exp(x)}{1+x}$, Eq. (3.3.11) consists of two term: the first term is obviously due to the central ion, and the second term is induced by the surrounding electrostatic cloud. The Helmholtz energy density, f^{el}, contributed by the electrostatic interaction is given by [11]

$$\beta f^{el} = -\frac{1}{4\pi\sigma^3}\left[\ln(\kappa_{\mathbf{D}}\sigma + 1) - \kappa_{\mathbf{D}}\sigma + \frac{(\kappa_{\mathbf{D}}\sigma)^2}{2}\right] \tag{3.3.13}$$

If the system is very dilute, we obtain the famous Debye limiting law

$$\beta f^{el} \approx -\frac{\kappa_{\mathbf{D}}^3}{12\pi} \sim -\left(\frac{\rho}{T}\right)^{3/2} \tag{3.3.14}$$

The total Helmholtz energy for the system is simply the electrostatic contribution (3.3.13) plus

the ideal gas contribution which is given by

$$\beta f^{id} = \rho \ln\left(\frac{\rho\Lambda^3}{2}\right) - \rho \tag{3.3.15}$$

where Λ is the de Broglie thermal wavelength [1]. In order to locate the phase co-existence (for two phases α and β), the pressures and the chemical potentials of the two phases should be equal. Therefore we have

$$\begin{cases} P_\alpha = P_\beta \\ \mu_\alpha = \mu_\alpha \end{cases} \tag{3.3.16}$$

Here we define some reduced units (reduced density ρ^*, reduced temperature T^* and reduced pressure P^*) which are commonly used in the following chapters.

$$\rho^* = \sum_i \rho_i \sigma_i^3 \tag{3.3.17}$$

$$T^* = \frac{\sigma}{l_B} \tag{3.3.18}$$

$$P^* = \beta P \sigma^3 T^* \tag{3.3.19}$$

Due to the analytical nature of the DH solution, we can easily find the critical point within DH theory. This is given by

$$\begin{cases} T_c^* = 0.0625 \\ \rho_c^* = \frac{1}{64\pi} \end{cases} \tag{3.3.20}$$

Originally, DH theory did not take the hard sphere Helmholtz energy contribution into account. If we turn off the charges on the particles, the total DH Helmholtz energy becomes that of an ideal gas. In reality, we should get a pure hard sphere system where the total Helmholtz energy should be that of an ideal gas plus the hard spheres. Therefore later theories [12, 13] have added the hard core (HC) term into the expression for the total Helmholtz energy density, f, viz, $f = f^{id} + f^{el} + f^{hc}$. This is called DHHC theory and this slightly changed the critical properties. The significance of DH theory is that the theory gives an analytical expression

of the electrostatic screening effect due to the large amount of ions forming the ionic cloud outside the central ionic particle. DH theory has been extended in many ways[12], where other complementary terms are added, including Bjerrum association (Bj)[11, 14], the dipole-ion (DI)[13] interaction and cluster-ion interactions (CI) [12].

3.3.2 Mean Spherical Approximation for Binary Hard Sphere Electrolytes

The mean spherical approximation (MSA) has proved to be accurate for the pure hard sphere system. For binary hard sphere electrolytes, it can also be solved analytically using Baxter's method [1]. The solution was firstly given by Blum [15] and Waisman [16]. For the RPM model, the final solution appears to be quite simple. Subsequently, Blum et. al. extended the method to size-asymmetric and charge-asymmetric primitive models [15, 17].

To review this work, we rewrite the Ornstein-Zernike equation in matrix form for a multi-component fluid

$$\mathcal{H}(r) - \mathcal{C}(r) = \int \mathcal{H}(r)\boldsymbol{\rho}\mathcal{C}(r)\,\mathrm{d}\mathbf{r} \tag{3.3.21}$$

where $\mathcal{H}(r)$, $\mathcal{C}(r)$ and $\boldsymbol{\rho}$ are matrices. In the RPM model, they are defined as:

$$\mathcal{H}(r) = \begin{pmatrix} h_{++}(r) & h_{+-}(r) \\ h_{-+}(r) & h_{--}(r) \end{pmatrix} \tag{3.3.22}$$

$$\mathcal{C}(r) = \begin{pmatrix} c_{++}(r) & c_{+-}(r) \\ c_{-+}(r) & c_{--}(r) \end{pmatrix} \tag{3.3.23}$$

$$\boldsymbol{\rho} = \begin{pmatrix} \rho_+ & 0 \\ 0 & \rho_- \end{pmatrix} \tag{3.3.24}$$

Within the MSA, for any pair of ions (i, j), the following conditions should be satisfied

$$h_{ij}(r) = -1, \quad r < \sigma_{ij} \tag{3.3.25}$$

$$\begin{aligned} c_{ij}(r) &= -\beta u_{ij}(r) \\ &= -\frac{z_i z_j l_B}{r}, \quad r > \sigma_{ij} \end{aligned} \tag{3.3.26}$$

where

$$\sigma_{ij} = (\sigma_i + \sigma_j)/2 \tag{3.3.27}$$

is the closest distance that two hard core particles can approach. In the RPM model, $\sigma_i = \sigma_j = \sigma_{ij} = \sigma$ and $\rho_+ = \rho_- = \rho/2$.

The scaling parameter Γ is a key quantity in the solution of the MSA. It is given as the solution of the two equations:

$$\Gamma^2 = \pi l_B \sum_s \rho_s \left(\frac{1}{1+\Gamma\sigma_s}\right)^2 \left(z_s - \frac{\pi P_n \sigma_s^2}{2\Delta}\right)^2 \tag{3.3.28}$$

$$P_n = \sum_s \frac{\rho_s \sigma_s z_s}{1+\Gamma\sigma_s} \left(1 + \frac{\pi}{2\Delta} \sum_s \frac{\rho_s \sigma_s^3}{1+\Gamma\sigma_s}\right) \tag{3.3.29}$$

where $\Delta = 1 - \pi\rho^*/6$, and the sums are over all species, 's', in the system. In the RPM model, the situation becomes very simple, since for an equal size system $P_n = 0$ due to electroneutrality. For an infinitely dilute solution, the scaling diameter 2Γ approaches the limit of the Debye inverse screening length $\kappa_{\mathbf{D}}$. After some mathematical calculations, the Helmholtz energy due to the electrostatic interaction is given by[15, 17]

$$\beta f^{el} = -l_B \left[\sum_s \frac{\rho_s z_s}{1+\Gamma\sigma_s} \left(\Gamma z_s + \frac{\pi P_n \sigma_s}{2\Delta}\right)\right] + \frac{\Gamma^3}{3\pi} \tag{3.3.30}$$

which reduces to $-l_B \left(\frac{\rho\Gamma}{1+\Gamma\sigma}\right) + \frac{\Gamma^3}{3\pi}$ for RPM. Similarly, the pressure due to the electrostatic interactions is

$$\begin{aligned} \beta P^{el} &= -\frac{\Gamma^3}{3\pi} - \frac{\pi l_B}{2} \left(\frac{P_n}{\Delta}\right)^2 \\ &= -\frac{\Gamma^3}{3\pi} \end{aligned} \tag{3.3.31}$$

the latter equality applying for the equal-size system.

When the temperature is sufficiently low, a phase separation of the RPM is also predicted by the MSA, with reasonably good agreement with the Monte-Carlo results [18]. The critical

temperature is found to be $T_c^* = 0.0786$ and the critical density is $\rho_c^* = 0.0144$ [11].

3.3.3 Results and Discussions

In this section, the results of various theories are compared with the Monte-Carlo results. Their advantages and disadvantages are discussed.

Behaviours at a Moderate Temperature

At a moderate temperature, e.g. T=298K which is usually set as the room temperature($25°C$), and the corresponding relative dielectric constant $\epsilon_r = 78.5$, for a hard sphere electrolyte system with $\sigma = 0.714$nm, the Bjerrum length is calculated to be $l_B/\sigma \approx 1.0$.

Fig. (3.4) shows the behaviour of $g(r)$ in the low density regime. It is clear that the HNC result is superior to that of the MSA. The results obtained from HNC are quite consistent with the Monte-Carlo results. The MSA underestimates both of the first peaks for g_{++} and g_{+-}. The radial distribution functions from DH theory are given as:

$$g_{ij}(r) = \exp(-\beta w_{ij}^f(r)), \qquad r > \sigma \tag{3.3.32}$$

$$g_{ij}(r) = 0, \qquad r < \sigma \tag{3.3.33}$$

For this state, DH results are semi-quantitatively correct, especially for $g_{+-}(r)$. Fig.(3.5) shows the radial distribution function of the binary system at a higher density $\rho^* = 0.7$. Due to the high density, there is a strong electrostatic screening effect. Therefore, the repulsion between like pairs is strongly affected by the hard sphere interaction. The results given by HNC again overestimate the first peaks in both cases as in the pure hard sphere system. The MSA results appears to be a better match with the Monte-Carlo results. Note that the DH results are not shown here due to the fact that at such high density, the linearising approximations no longer hold. As Eq. (3.3.32) suggests, the DH theory cannot predict any hard sphere effects. $g(r)$ from DH theory is a monotonically decaying function.

Fig. (3.6) shows the total pressure calculated via the virial route at various densities. At low densities, all of the three theories work consistently, since $l_B = \sigma$ corresponds to a weak electrostatic interaction system. At high densities, the deficiency of HNC in characterising the

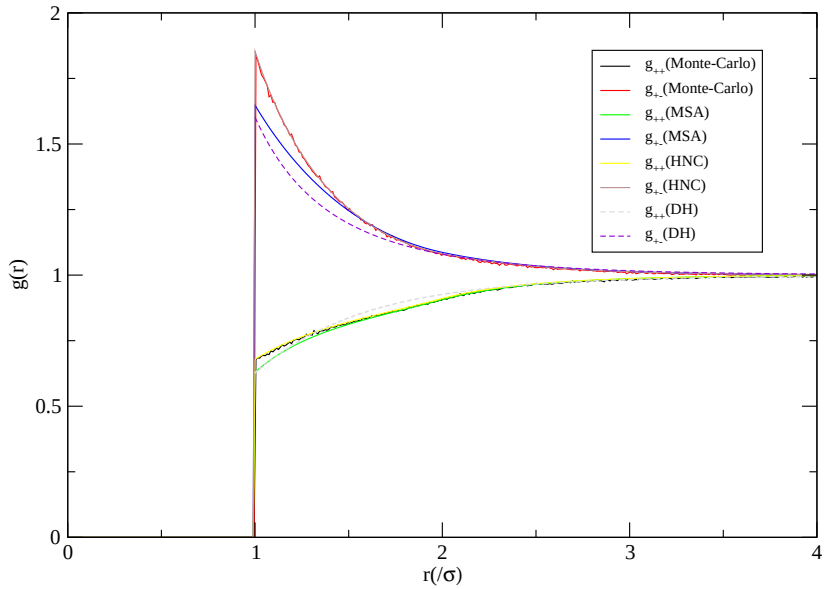

Figure 3.4: Radial distribution functions of the RPM given by Monte-Carlo simulation, MSA, HNC and DH. System: $l_B/\sigma = 1.0, \rho^* = 0.1$.

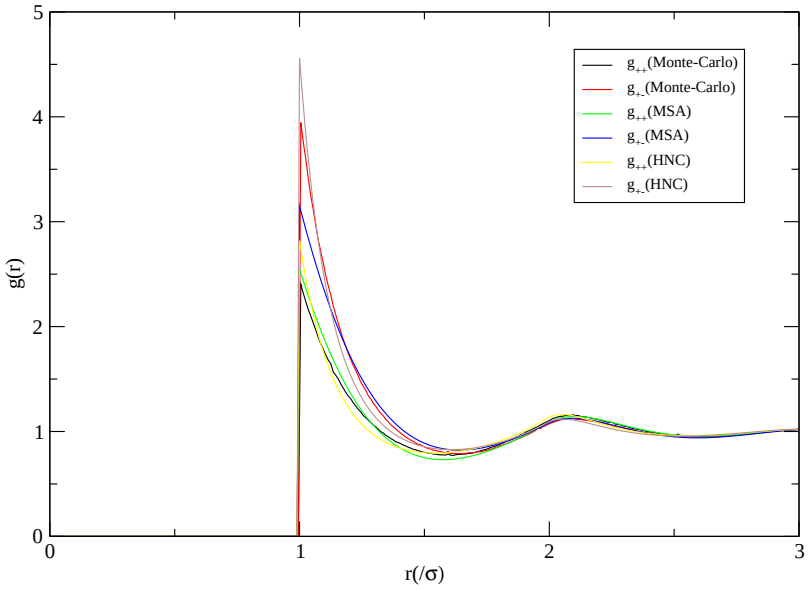

Figure 3.5: Radial distribution functions of the RPM given by Monte-Carlo simulation, MSA and HNC. System: $l_B/\sigma = 1.0, \rho^* = 0.7$.

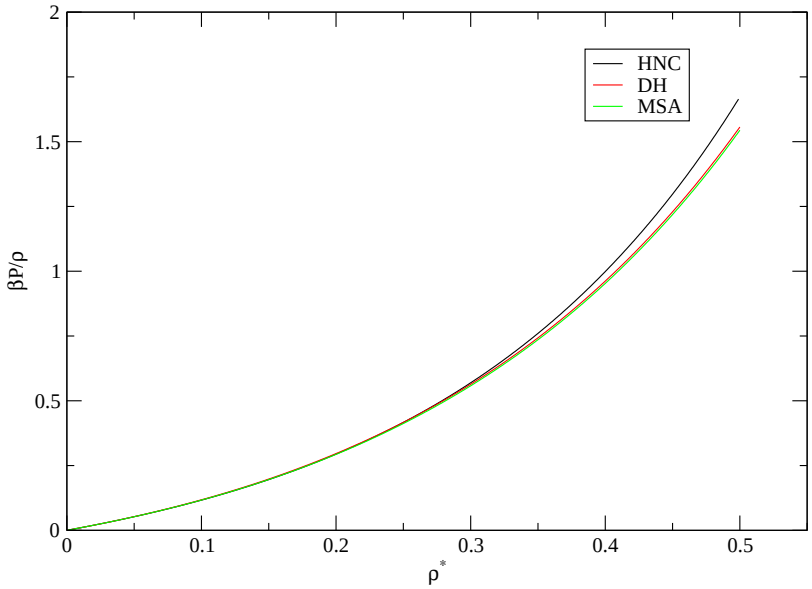

Figure 3.6: The pressure of the RPM system via virial route given by DH, MSA and HNC. The temperature is fixed by $l_B = \sigma$.

hard sphere system appears again. (Note: In DH calculations, we have added the missing hard sphere term (given by BMCSL theory) into the original DH theory. The total Helmholtz energy density of the system is given by $f^{Total} = f^{id} + f^{hs} + f^{el}$.)

Behaviours at a Low Temperature

At a lower temperature, much bigger discrepancies start to show between simulation and theory. In the system shown in Fig. (3.7), where $l_B = 5.0\sigma, \rho^* = 0.1$, HNC gives a very good prediction for $g(r)$, in good agreement with the Monte-Carlo results. Even in the region where $2\sigma < r < 3\sigma$, HNC predicts perfectly the 'inversely charging zone' [19] where $g_{++}(r) > g_{+-}(r)$. MSA, on the contrary, works poorly at such a temperature and density. The $g_{+-}(r)$ from MSA largely underestimates the first peak, while $g_{++}(r)$ shows a negative value at the first peak which is totally unphysical. DH theory gives a reasonable prediction for the first peaks for the like and unlike pairs but misses the details of the inversely charging zone.

The reason for the poor prediction of MSA can be found in Blum's [15] solutions for $g(\sigma)$. These take the form

$$g_{ij}(\sigma) = \frac{1}{\Delta} + \frac{\pi\rho^*}{4\Delta^2} - \frac{\Gamma^2 a_i a_j}{4\pi^2\sigma l_B} \tag{3.3.34}$$

$$a_k = \frac{2\pi l_B z_k}{\Gamma(1+\Gamma\sigma)} \tag{3.3.35}$$

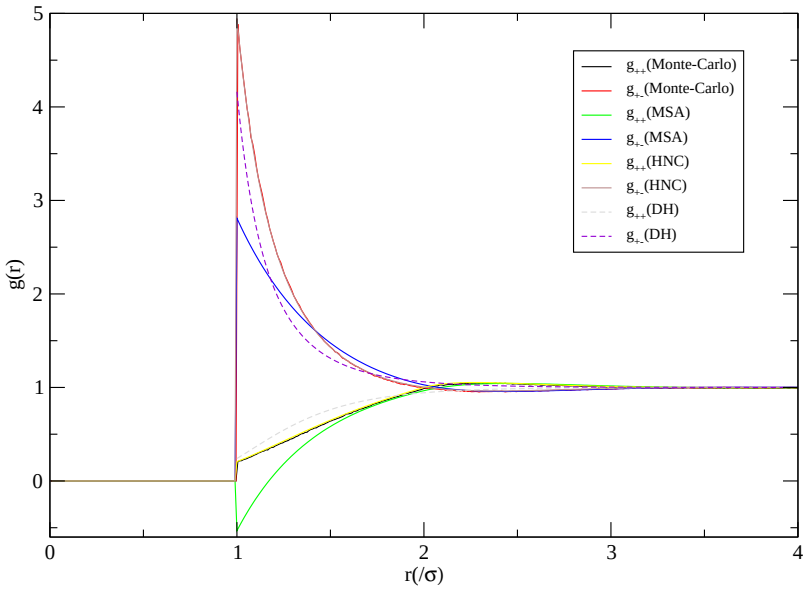

Figure 3.7: Radial distribution functions of the RPM given by Monte-Carlo simulation, MSA and HNC. System: $l_B/\sigma = 5.0, \rho^* = 0.1$.

The three terms on the right-hand-side of the Eq. (3.3.34) describe $g(\sigma)$. The first two terms result from the hard core of the particles while the third term describes the effect of the electrostatic interactions. Though $g(\sigma)$ for the pure hard sphere system is always positive, $g_{++}(\sigma)$ can easily go negative when l_B is large or the scaling parameter is small (indicating a low density).

However, the discrepancy in the macroscopic properties, such as pressure, is not so large. Fig. (3.8) shows the pressure at various densities with $l_B = 5.0\sigma$. In fact, HNC and MSA show good agreement at low densities despite the big discrepancies in the prediction of $g(r)$. One reason is that the expression for the excess internal energy U^{ex} involves $(g_{+-}(r) - g_{++}(r))$, and this is used to calculate pressure via the virial route. This difference is very similar for both HNC and MSA, and this makes the reduced pressure similar also.

Predictions of Phase Behaviours

When the temperature is sufficiently low, a phase separation occurs in the binary electrolyte system. This has been observed in simulations [20].

Though HNC has been the best theory so far in predicting $g(r)$ for charged systems at a low density, unfortunately, there is no real solution for any temperature below a certain value, i.e. $l_B > 10.0\sigma$. Thus no phase coexistence can be predicted. A similar state of affairs exist for many other systems, such as a system interacting via a Lennard-Jones pair potential [21]. The

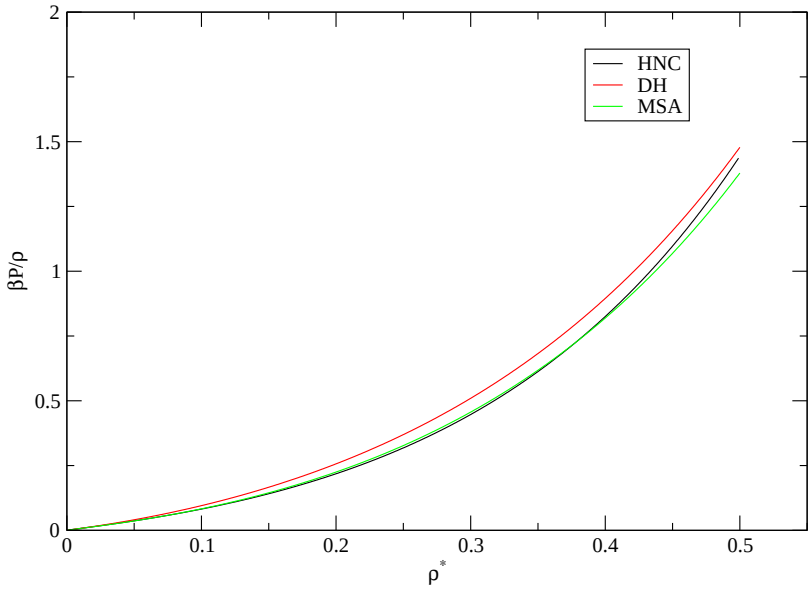

Figure 3.8: Pressures of the RPM via virial route given by DH, MSA and HNC. The temperature is fixed by $l_B/\sigma = 5.0$.

HNC approximation together with Ornstein-Zernike equation can only be solved in the complex plane instead of giving real solutions [22]. These complex solutions have no physical meanings. Some modifications of HNC have been proposed which will improve the theoretical prediction of the radial distribution function for various fluid systems. A major modification is to include a family of bridge functions [23], however the region of no solution is at least partially inherited from the original HNC approximation.

However, DH and MSA both predict a phase transition at low temperature. As seen in Fig. (3.9), they only give qualitatively correct predictions as compared with MC results. The MC co-existence curve [24, 25] shows a broad plateau when the temperature is close to the critical point, while both theories are of a mean-field type which gives a sharper curve in the critical region. Both the theories predict the gas phase rather poorly, especially the MSA. This is thought to be a result of the complicated ionic clustering which neither theory treats well.

Other Approaches

There are some other theories which can be used to characterise the binary electrolyte solution. Examples are, the Random Phase Approximation (RPA) and the Exponential approxima-

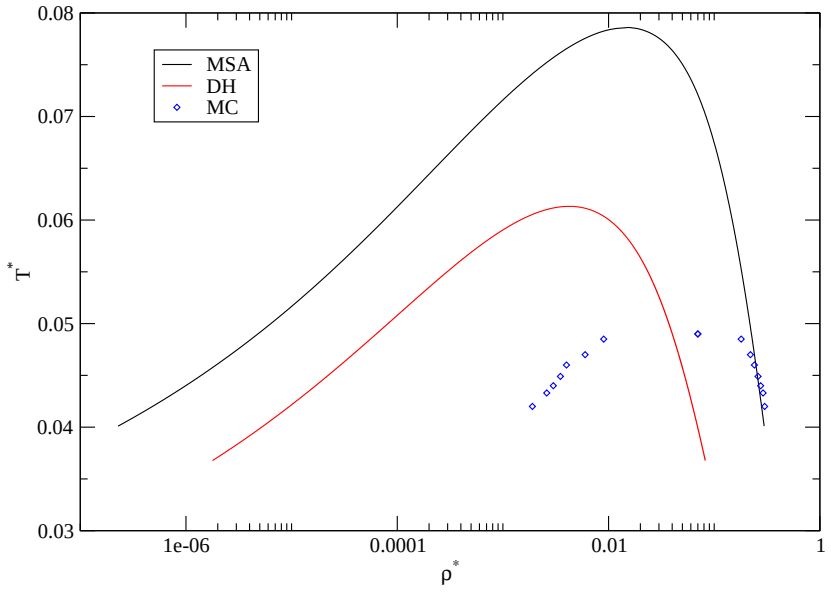

Figure 3.9: Phase behaviour for RPM electrolytes predicted by DH and MSA (Monte-Carlo results are reproduced from Panagiotopolous[24]).

tion (EXP). RPA and EXP are both based on the perturbation theory [1]. The RPA assumes

$$c(r) = c_0(r) - \beta w(r) \tag{3.3.36}$$

where $c_0(r)$ denotes a known reference direct correlation function (typically a hard sphere system). This expression for $c(r)$ is asymptotically correct. However, there are two restrictions for RPA [1]: 1) The perturbation should be sufficiently weak; 2) The density should be low enough. The RPA can be derived via diagrammatic methods as follows:

First of all, we write the Ornstein-Zernike equation for a one-component fluid as

$$h(\mathbf{r_1}, \mathbf{r_2}) - c(\mathbf{r_1}, \mathbf{r_2}) = \int c(\mathbf{r_1}, \mathbf{r_3})\rho(\mathbf{r_3})h(\mathbf{r_3}, \mathbf{r_2})\,\mathrm{d}\mathbf{r_3} \tag{3.3.37}$$

We write the Ornstein-Zernike equation in the position-dependent form in order to show the connection between the integrals and the diagrams. The pair correlation function $h(\mathbf{r_1}, \mathbf{r_2})(= h(r_{12})$ for an isotropic fluid) can be solved recursively as

$$\begin{aligned} h(\mathbf{r_1}, \mathbf{r_2}) =& c(\mathbf{r_1}, \mathbf{r_2}) + \int c(\mathbf{r_1}, \mathbf{r_3})\rho(\mathbf{r_3})c(\mathbf{r_3}, \mathbf{r_2})\,\mathrm{d}\mathbf{r_3} \\ &+ \iint c(\mathbf{r_1}, \mathbf{r_3})\rho(\mathbf{r_3})c(\mathbf{r_3}, \mathbf{r_4})\rho(\mathbf{r_4})c(\mathbf{r_4}, \mathbf{r_2})\,\mathrm{d}\mathbf{r_3}\mathrm{d}\mathbf{r_4} + \ldots \end{aligned} \tag{3.3.38}$$

This recursion can be expressed in a diagram expansion as:

$h(\mathbf{r_1}, \mathbf{r_2}) =$ 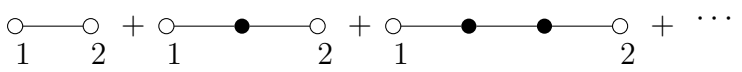

where each chain diagram consists of two terminal white circles labelled 1 and 2 (representing $\mathbf{r_1}$ and $\mathbf{r_2}$ respectively), black $\rho-$ circles and $c-$ bonds.

Other pair functions can be expanded in a similar diagrammatic way. For the RPA, the approximation to get the radial distribution function is that

$$g(\mathbf{r_1}, \mathbf{r_2}) \approx g_0(\mathbf{r_1}, \mathbf{r_2}) + C(\mathbf{r_1}, \mathbf{r_2}) \tag{3.3.39}$$

where $C(\mathbf{r_1}, \mathbf{r_2})$ is given by

$$\begin{aligned} \rho^2 C(\mathbf{r_1}, \mathbf{r_2}) = [&\text{all chain diagrams consisting of two terminal white} \\ &\rho - \text{circles labelled 1 and 2, black } \rho\text{−circles,} \\ &\Psi - \text{bonds and } h_0\text{−bonds, where no two successive } h_0\text{−bonds are allowed}] \end{aligned} \tag{3.3.40}$$

$h_0(\mathbf{r_1}, \mathbf{r_2})$ is the pair correlation function for the reference fluid and $\Psi(\mathbf{r_1}, \mathbf{r_2}) = -\beta w(\mathbf{r_1}, \mathbf{r_2})$

We may group the chain diagrams according to their $\Psi-$ bonds number n, so that we write

$$\rho^2 C(\mathbf{r_1}, \mathbf{r_2}) = \rho^2 \sum_{n=1}^{\infty} C^{(n)}(\mathbf{r_1}, \mathbf{r_2}) \tag{3.3.41}$$

Let $C^{(n)}(\mathbf{r_1}, \mathbf{r_2})$ denote the chain diagrams containing n $\Psi-$bonds. In this way, we have

$\rho^2 C^{(1)}(\mathbf{r_1}, \mathbf{r_2}) =$ 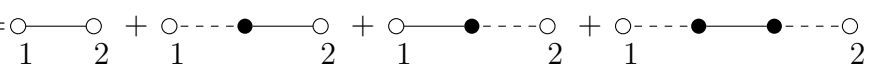

and so on (the solid lines represent the $\Psi-$bonds while the dashed lines represent the h_0-bonds). For binary mixtures, RPA gives the same diagrammatic form but the $\Psi-$ and h_0- bonds can be between different species. In this case, the RPA for the binary electrolyte system is then reduced to the linearised DH theory.

On the other hand, the EXP approximation assumes

$$g_{ab}(\mathbf{r_1}, \mathbf{r_2}) = g_{ab,0}(\mathbf{r_1}, \mathbf{r_2}) \exp\left[C_{ab}(\mathbf{r_1}, \mathbf{r_2})\right] \tag{3.3.42}$$

where $g_0(r)$ is the radial distribution function obtained in the reference system. Commonly the hard sphere system is chosen to be the reference system. This gives the correct behaviour of the hard sphere core condition: $g(\mathbf{r_1}, \mathbf{r_2}) = 0$ for $r < \sigma$. For Eq.(3.3.34), we find that the first two terms of $g(\sigma)$ given by MSA describe the hard sphere effect. While only the third term describes the electrostatic effect (if $z_+ = z_- = 0$, the third term is 0). As a result, the MSA result for RPM can be expressed in terms of $g_{ij}(\sigma) = g_{ij,0}(\sigma) + C_{ij}(\sigma)$.
Therefore we have

$$g_{ij,0}(\sigma) = \frac{1}{\Delta} + \frac{\pi\rho^*}{4\Delta^2} \tag{3.3.43}$$

$$C_{ij}(\sigma) = -\frac{\Gamma^2 a_i a_j}{4\pi^2 \sigma l_B} \tag{3.3.44}$$

The EXP approximation gives a better description of the ionic system than the MSA [26]. Fig. (3.10) shows the improvement of $g(\sigma)$ when we change MSA to EXP. The EXP shows a satisfactory prediction over the whole range while MSA fails badly at low densities.

RPM model is an idealised theoretical model for investigating the properties of electrolyte systems. It does suffer, however, from a lack of realism. As a simple example, an aqueous sodium chloride solution at 298K has a particle size $\sigma = 0.857$nm, dielectric constant $\epsilon_r = 78.5$. These parameters give the Bjerrum length $l_B = 0.833\sigma$ and a reduced temperature $T^* \approx 1.2$. When the system falls into the critical region, according to the RPM model, $T^* \approx 0.05$. This corresponds to a real temperature of about 13K. At such temperatures a real solvent will have already solidified. For colloid systems, the result is more meaningful as colloids are much bigger than simple ions.

3.4 Bjerrum Association and Ternary Systems

DH theory introduced the fruitful concept of screened electrostatic interactions between the ions, though its prediction of the phase co-existence curve shows a large discrepancy from simulation results. In order to improve the work, Bjerrum proposed a supplementary association concept [11, 14]. At low temperatures, the electrostatic interaction is much stronger than the thermal energy for any pairs separated by a short distance. Bjerrum's postulate is that when two oppositely charged particles are separated by a distance shorter than some characteristic

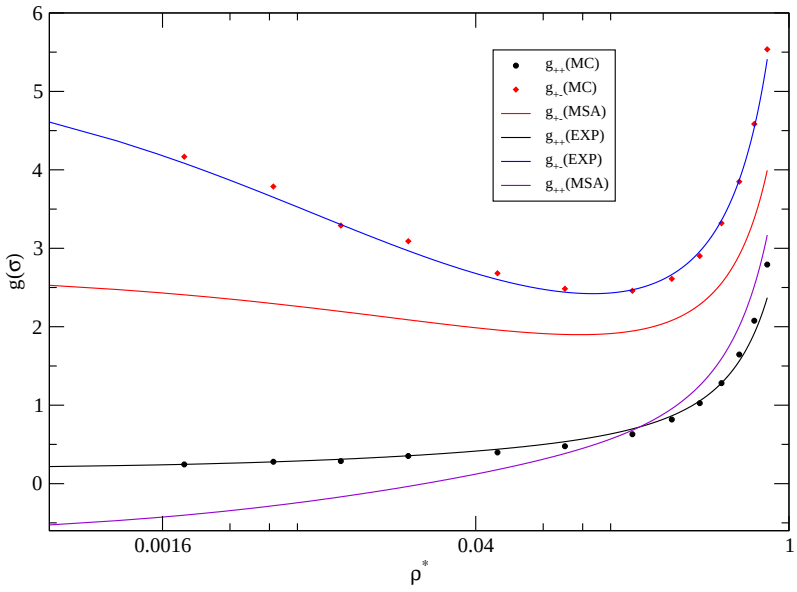

Figure 3.10: The comparison of $g(\sigma)$ between MSA and EXP, $l_B = 0.833\sigma$.

length R, the two particles form an associated pair which may be treated approximately as an ideal non-interactive particle. We denote the total density of the system as ρ, the density of associated pairs as ρ_o, and the densities of the charged particles as ρ_+ and ρ_- respectively. In this case, the densities satisfy:

$$\rho = \rho_+ + \rho_- + 2\rho_o \tag{3.4.1}$$

According to the law of mass action,

$$K = \frac{\rho_o}{\rho_+ \rho_-} \tag{3.4.2}$$

where the equilibrium constant K is defined as

$$K = 4\pi \int_\sigma^R \exp(l_B/r) r^2 \, \mathrm{d}r \tag{3.4.3}$$

The characteristic length, R, in Bjerrum's association theory was chosen arbitrarily to be half of the Bjerrum length [14]. In this theory, the driving force for phase separation is still the electrostatic forces between the charged particles while the non-interactive associated pairs only change the total density of the system. Therefore, Bjerrum's association theory does not change the critical temperature from that given in DH theory but it increases the critical density to

$\rho_c^* \approx 0.045$ [11] which is much closer to the critical density $\rho_c^* = 0.0786$ observed in Monte-Carlo simulations [24].

3.4.1 Numerical Results and Discussions

In this section, we consider a mixture of neutral hard spheres with the electrolytes. All the particles in the system have hard sphere potentials:

$$u_{ij}(r) = u^{\text{hs}}(r), r < \sigma \tag{3.4.4}$$

$$\tag{3.4.5}$$

Outside the hard sphere core, the pair potentials are defined by:

$$\beta u_{ij}(r)(r > \sigma) = \begin{cases} 0, i \text{ or } j = \text{neutral} \\ l_B/r, \text{charged like-pair} \\ -l_B/r, \text{charged unlike-pair} \end{cases} \tag{3.4.6}$$

The neutral particle is denoted by the subscript 'o' while the charged particles are either '+' or '-' depending on their sign of their charge.

We study this system both by Monte-Carlo simulations and by theoretical calculations. The reasons why we consider this ternary system are:

1. We want to test the quality of the classical theories for the more general system;
2. We want to see whether or not the hard spheres in a charged system is 'non-interactive', as Bjerrum treating the 'neutral pairs' to be non-interactive.
3. This particular mixture is likely to be an important reference system when applying SAFT to polyelectrolytes.

First of all, we focus on the special pairs of "neutral-neutral" and "neutral-charge". The neutral hard spheres in the ternary system should be non-interactive according to Bjerrum [14]. However, the MC results exhibit a difference in the radial distribution functions between the two pairs. At high temperatures, the difference between $g_{oo}(\sigma)$ and $g_{o+}(\sigma)$ is tiny and therefore

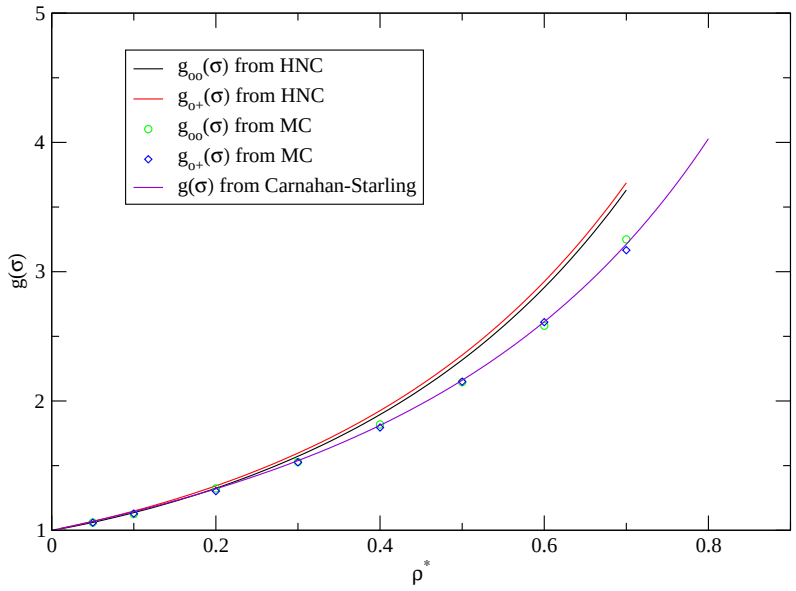

Figure 3.11: The comparison of $g_{oo}(\sigma)$ and $g_{o+}(\sigma)$ in the ternary system: $\rho_+^* = \rho_-^* = \rho_o^* = \rho^*/3$, $l_B/\sigma = 1.0$.

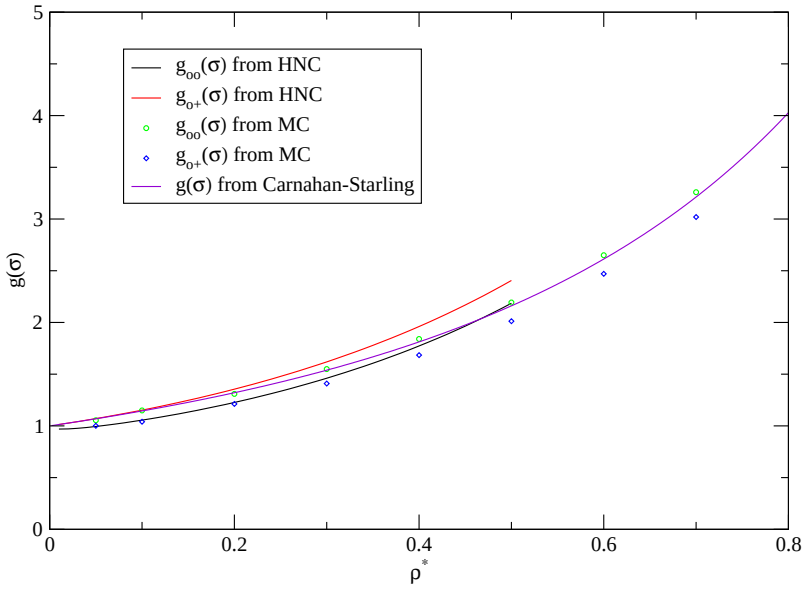

Figure 3.12: The comparison of $g_{oo}(\sigma)$ and $g_{o+}(\sigma)$ in the ternary system: $\rho_+^* = \rho_-^* = \rho_o^* = \rho^*/3$, $l_B/\sigma = 5.0$.

may be negligible as shown in Fig. (3.11). But as the temperature drops, the difference starts to become significant. Fig (3.12) clearly shows the difference between the two radial distribution function at contact. This difference can be predicted by HNC calculation at low densities while MSA cannot give a proper prediction. The prediction becomes poor when the density goes up. This is reasonable since HNC works poorly for dense hard sphere systems. Based on the MC results, the critical temperature of the RPM model corresponds to a Bjerrum length approximately $l_B/\sigma \approx 20$. At that temperature, the difference on $g(\sigma)$ between the two types of pairs is expected to be very significant.

Fig. (3.13) shows the direct correlation functions of "neutral-neutral" pairs and "neutral-charge" pairs from HNC. From the figure, it is clear that the direct correlation function is different between the two pairs both inside the core and outside the core. For neutral-neutral pairs, we can see that the direct correlation function is slightly positive outside the core. The neutral-charged pair has its direct correlation function very close to zero. This helps to explain why $g_{oo}(\sigma)$ is slightly bigger than $g_{o+}(\sigma)$: If we treat the direct correlation function in both cases as a reference hard core plus a weak perturbation, the positive tail for $c_{oo}(r)$ shows a weak attraction between the neutral-neutral pair as compared with the neutral-charged pair. This also suggests the Bjerrum's postulate could be further improved: even if some of the particles can be treated as neutral couples, they should not be treated as "non-interactive"(pure hard sphere). The physical reason why $g_{oo}(\sigma)$ has a greater value than $g_{o+}(\sigma)$ may be due to the steric hindrance of the different particles. A charged particle easily attracts an oppositely charged particle, therefore when a neutral particle approaches it, the nearest space may already be occupied by the oppositely charged particle.

3.4.2 Flaws in Random Phase Approximation

As mentioned in last section, MSA and some other theories such as RPA could not predict correctly the difference between the "neutral-neutral" pair and the "neutral-charge" pair. Here we give a brief discussion.

We start from the RPA. Assume a system containing equal amount of particles with charge of $z_+ = +e$, $z_- = -e$ and $z_o = 0$ (neutral) respectively, the density for each type of particle is

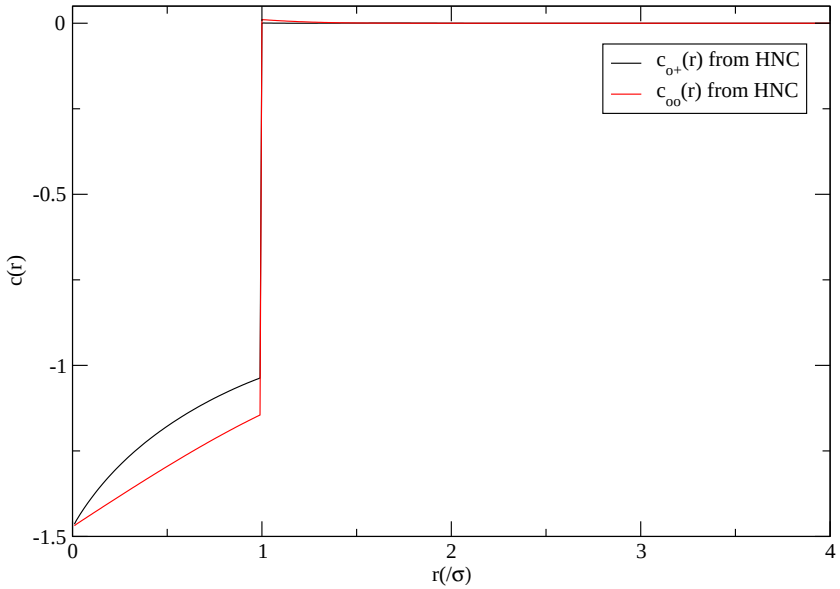

Figure 3.13: The comparison of $c_{oo}(r)$ and $c_{o+}(r)$ in the ternary system: $\rho_+^* = \rho_-^* = \rho_o^* = 0.1/3$, $l_B/\sigma = 5.0$.

therefore

$$\rho_+ = \rho_- = \rho_o = \rho/3 \tag{3.4.7}$$

We denote the direct correlation function from a reference hard sphere system as $c^{\text{hs}}(r)$. The corresponding potential between the different pairs outside the hard-core are denoted as $u_{ij}(r)$ such that

$$u_{++}(r) = u_{--}(r) = -u_{+-}(r) \tag{3.4.8}$$

$$u_{+o}(r) = u_{-o}(r) = u_{oo}(r) = 0 \tag{3.4.9}$$

The corresponding direct correlation functions in the ternary system are

$$c_{ij}(r) = c^{\text{hs}}(r) - \beta u_{ij}(r) \tag{3.4.10}$$

Therefore for the neutral-related particle pairs, we have

$$c_{o+}(r) = c_{o-}(r) = c_{oo}(r) = c^{\text{hs}}(r) \tag{3.4.11}$$

By extending the Ornstein-Zernike equation, we have

$$\begin{aligned} h_{oo}(r_{12}) - c_{oo}(r_{12}) = & \int c_{oo}(r_{13})\rho_o h_{oo}(r_{32})\,\mathrm{d}\mathbf{r_3} \\ & + \int c_{o+}(r_{13})\rho_+ h_{+o}(r_{32})\,\mathrm{d}\mathbf{r_3} \\ & + \int c_{o-}(r_{13})\rho_- h_{-o}(r_{32})\,\mathrm{d}\mathbf{r_3} \end{aligned} \tag{3.4.12}$$

$$\begin{aligned} h_{+o}(r_{12}) - c_{+o}(r_{12}) = & \int c_{+o}(r_{13})\rho_o h_{oo}(r_{32})\,\mathrm{d}\mathbf{r_3} \\ & + \int c_{++}(r_{13})\rho_+ h_{+o}(r_{32})\,\mathrm{d}\mathbf{r_3} \\ & + \int c_{+-}(r_{13})\rho_- h_{-o}(r_{32})\,\mathrm{d}\mathbf{r_3} \end{aligned} \tag{3.4.13}$$

Taking Eq. (3.4.11), Eq. (3.4.7) and the symmetry of subscripts, we can simplify the above equations such that

$$\begin{aligned} h_{oo}(r_{12}) - c^{\text{hs}}(r_{12}) = & \frac{1}{3}\int c^{\text{hs}}(r_{13})\rho h_{oo}(r_{32})\,\mathrm{d}\mathbf{r_3} \\ & + \frac{2}{3}\int c^{\text{hs}}(r_{13})\rho h_{+o}(r_{32})\,\mathrm{d}\mathbf{r_3} \end{aligned} \tag{3.4.14}$$

$$\begin{aligned} h_{+o}(r_{12}) - c^{\text{hs}}(r_{12}) = & \frac{1}{3}\int c^{\text{hs}}(r_{13})\rho h_{oo}(r_{32})\,\mathrm{d}\mathbf{r_3} \\ & + \frac{1}{3}\int \left(c_{++}(r_{13}) + c_{+-}(r_{13})\right)\rho h_{+o}(r_{32})\,\mathrm{d}\mathbf{r_3} \end{aligned} \tag{3.4.15}$$

Taking Eq. (3.4.10) into account, the perturbation terms in $c_{+-}(r)$ and $c_{++}(r)$ are exactly the same but with opposite signs. Therefore

$$c_{+-}(r) + c_{++}(r) = 2c^{\text{hs}}(r) \tag{3.4.16}$$

In this case, it is clear that $h_{oo}(r) = h_{o+}(r)$.

MSA shares the same definition of the direct correlation function outside the hard sphere. With the same $g(r)$ inside the core, our numerical calculation gives the same result that $h_{oo}(r) = h_{o+}(r)$ for MSA, but we have not established whether this is also an analytical result. However, Hall et. al.[27, 28] have used the MSA to approach the phase diagram for ternary systems. In particular systems, these phase diagrams [29] are in good agreement with the experimental results.

3.5 Conclusion

In this chapter, many classical theories have been reviewed and have been applied to the hard sphere electrolyte system. Among all the theories discussed, HNC is the best at giving accurate predictions of the structure-related properties of the systems at a low density. However, the HNC cannot predict the phase behaviour of the binary electrolyte system due to the lack of numerical solutions at low temperatures. On the other hand, the MSA can be solved analytically, but the accuracy is rather poor in describing the Coulombic system. Though widely studied, the theories for RPM model still can be further developed. These classical theories form a good theoretical basis for the study of electrolyte systems and also polyelectrolyte systems. In the following chapters, we will first use the RPM as a basis for a theory of polyelectrolytes. After that, we will try to improve the theoretical results for the RPM itself. This will give a good picture of better theoretical characterisation the (poly-)electrolyte fluid systems.

3.6 References

[1] J.P. Hansen and I.R. McDonald. *Theory of Simple Liquids*. Academic Press, 1976. See pp. 21–26, 31, 32, 39.

[2] J.A. Barker and D. Henderson. "Monte Carlo values for the radial distribution function of a system of fluid hard spheres". In: *Molecular Physics* 21 (1971), pp. 187–191. See pp. 23, 26.

[3] J.L. Lebowitz. "Exact Solution of Generalized Percus-Yevick Equation for a Mixture of Hard Spheres". In: *Phys. Rev. Lett.* 133.4A (1964), A895–A899. See p. 23.

[4] E. Thiele. "Equation of State for Hard Spheres". In: *The Journal of Chemical Physics* 39 (1963), pp. 474–479. See pp. 23, 24.

[5] M.S. Wertheim. "Exact Solution of the Percus-Yevick Integral Equation for Hard Spheres". In: *Physical Review Letters* 10 (1963), pp. 321–323. See p. 23.

[6] N.F. Carnahan and K.E. Starling. "Equation of State for Nonattracting Rigid Spheres". In: *The Journal of Chemical Physics* 51 (1969), pp. 635–636. See p. 24.

[7] T. Boublík. "Hard-Sphere Equation of State". In: *The Journal of Chemical Physics* 53 (1970), pp. 471–472. See p. 24.

[8] G.A. Mansoori et al. "Equilibrium Thermodynamic Properties of the Mixture of Hard Spheres". In: *The Journal of Chemical Physics* 54 (1971), pp. 1523–1525. See p. 24.

[9] J.A. Barker and D. Henderson. "What is "liquid"? Understanding the state of matter". In: *Reviews of Modern Physics* 48 (1976), pp. 587–671. See pp. 24, 25.

[10] K.C. Ng. "Hypernetted chain solutions for the classical one-component plasma up to Γ=7000". In: *The Journal of Chemical Physics* 61 (1974), pp. 2680–2689. See p. 25.

[11] Y. Levin. "Electrostatic correlations: from plasma to biology". In: *Reports on Progress in Physics* 65 (2002), pp. 1577–1632. See pp. 26, 28, 30, 32, 34, 41, 43.

[12] M.E. Fisher and Y. Levin. "Criticality in ionic fluids: Debye-Hückel theory, Bjerrum, and beyond". In: *Physical Review Letters* 71 (1993), pp. 3826–3829. See pp. 26, 28, 31, 32.

[13] J. Aqua, S. Banerjee, and M.E. Fisher. "Criticality in charge-asymmetric hard-sphere ionic fluids". In: *Phys. Rev. E.* 72 (2005), p. 041501. See pp. 31, 32.

[14] A. Travesset and D. Vaknin. “Bjerrum pairing correlation at charged interfaces”. In: *Europhyiscs Letters* 74 (2006), pp. 181–187. See pp. 32, 41–43.

[15] L. Blum. “Mean spherical model for asymmetric electrolytes. I. Method of solution”. In: *Molecular Physics* 30 (1975), pp. 1529–1535. See pp. 32, 33, 36.

[16] E. Waisman. “Solution of the mean spherical model for a mixture exhibiting phase separation”. In: *The Journal of Chemical Physics* 59 (1973), pp. 495–497. See p. 32.

[17] L. Blum and J.S. Hoye. “Mean spherical model for asymmetric electrolytes. 2. Thermodynamic properties and the pair correlation function”. In: *The Journal of Physical Chemistry* 81 (1977), pp. 1311–1316. See pp. 32, 33.

[18] A.Z. Panagiotopoulos. “Simulations of phase transition in ionic systems”. In: *Journal of Physics: Condensed Matter* 17 (2005), pp. 3205–3212. See p. 33.

[19] J. Sýs, S. Labík, and A. Malijevský. “Parameterization of the radial distribution function and thermodynamic properties of the restricted primitive model of electrolyte solutions”. In: *Czech. J. Phys. B* 33 (1983), pp. 763–771. See p. 36.

[20] M.P. Allen and D.J. Tildesley. *Computer Simulation of Liquids*. Clarendon Press, Oxford, 2002. See p. 37.

[21] A.G. Schlijper, M.M Telo da Gamma, and P.G. Ferreira. “Thermodynamic consistency in the hypernetted chain theory”. In: *Journal of Chemical Physics* 98 (1993), pp. 1534–1538. See p. 37.

[22] E. Lomba and J.L. Lòpez-Martin. “On the Solutions of the Hypernetted Chain Equation Inside the Gas-Liquid Coexistence Region”. In: *Journal of Statistical Physics* 80 (1995), pp. 825–839. See p. 38.

[23] Y. Rosenfeld and N.W. Ashcroft. “A New Theory of Simple Classical Fluids”. In: *Phys. Rev. A* 73 (1979), pp. 31–34. See p. 38.

[24] G. Orkoulas and A.Z. Panatiotopoulos. “Free energy and phase equilibria for the restricted primitive model of ionic fluids from Monte Carlo simulations”. In: *Journal of Chemical Physics* 101 (1994), pp. 1452–1459. See pp. 38, 39, 43.

[25] A.Z. Panagiotopoulos. “Molecular simulation of phase equilibria: simple, ionic and polymeric fluids”. In: *Fluid Phase Equilibria* 76 (1992), pp. 97–112. See p. 38.

[26] O. Bernard and L Blum. “Binding mean sperical approximation for pairing ions: An exponential approximation and thermodynamics”. In: *The Journal of Chemical Physics* 104 (1996), pp. 4746–4754. See p. 41.

[27] P.U. Kenkare and C.K. Hall. “Phase instabilities in charged hard-sphere mixtures. I. Binary mixtures of salt and hard spheres”. In: *Journal of Chemical Physics* 103 (1995), pp. 8098–8102. See p. 47.

[28] P.U. Kenkare and C.K. Hall. “Phase instabilities in charged hard-sphere mixtures. II. Binary mixtures of salts”. In: *Journal of Chemical Physics* 103 (1995), pp. 8111–8123. See p. 47.

[29] C. Caccamo and A. Giacoppo. “Liquid-liquid phase separation and critical exponents in ionic fluid mixtures”. In: *Phys. Rev. A* 42 (1990), p. 6285. See p. 47.

CHAPTER

FOUR

A STATISTICAL ASSOCIATING FLUID THEORY FOR POLYELECTROLYTES

4.1 Introduction

Polyelectrolytes are chains of charged monomers. They share some common properties with the electrolytes and, like them, theoretical descriptions are far from complete. In the previous chapter, we discussed some classical theories for hard sphere electrolyte systems. Here we re-visit some existing calculations for polyelectrolytes based on classical theories. Some attempted improvements are also discussed in this chapter. We present a statistical associating fluid theory (SAFT) [1–6] for polyelectrolyte solutions. The original SAFT theory is derived for molecules with short-range pair potentials and has been shown to be accurate for neutral polymers. Jiang et. al. have extended the SAFT theory to polyelectrolytes [7]. The polyelectrolyte chains are modelled as tangentially connected charged hard spheres. Therefore the polyelectrolyte system is modelled as a fluid of monomers plus an extra perturbation due to the chain connectivity. In this chapter, first we are going to reproduce the results given by Jiang et. al. [7] in Section(4.3). However, there are some inconsistencies in their theory. We try to replace some of the terms by consistent theoretical expressions. Our attempt to use Debye-Hückel (DH) terms in the SAFT theory is described in Section(4.4). We offer further discussions in Section(4.5).

4.2 Theory and Expressions

We consider a model polyelectrolyte composed of tangentially-bonded charged hard spheres along with neutralising couterions. The SAFT expression for the Helmholtz energy (A) of the

system is:

$$A^{Total} = A^{id} + A^{hs} + A^{el} + A^{chain} \tag{4.2.1}$$

where the superscripts 'id', 'hs', 'el' and 'chain' correspond to the ideal gas contribution, the hard sphere contribution, the electrostatic contribution and the chain connectivity contribution respectively. Instead of directly using the Helmholtz energy, the Helmholtz energy density $f(= A/V)$ is preferred, especially in calculations. The ideal gas contribution is given by Eq. (3.3.15). The hard sphere contribution comes from Boublik and Mansoori, etc [8–10], which is:

$$\beta f^{hs} = (\zeta_2^3/\zeta_3^2 - \zeta_0)\ln\Delta + \frac{\pi\zeta_1\zeta_2/2 - \zeta_2^3/\zeta_3^2}{\Delta} + \frac{\zeta_2^3/\zeta_3^2}{\Delta^2} \tag{4.2.2}$$

where $\zeta_n = \sum_i \rho_i \sigma_i^n$ and $\Delta = 1 - \pi\zeta_3/6$. We may notice that ζ_3 is in fact the reduced density ρ^* of the system and therefore $\Delta = 1 - \eta$ is the unoccupied volume of the system. The term f^{el} depends on the chosen theory and here we choose the MSA. The MSA expression for f^{el} is given in Eq.(3.3.30) in the last chapter.

The original concept of SAFT is that we start from a hard sphere system, and add the short-range pair potential as a perturbation. In this way we get the Helmholtz free energy for the monomer system. Then we use the monomer fluid as a reference system. The chain connectivity part of the Helmholtz free energy is introduced by requiring two particles to be tangentially connected. The polyelectrolyte chain and counterions are sketched in Fig.(4.1).

For polyelectrolytes, Jiang et. al. adapt a similar concept. As an analogy to the short-range potential, they treat the electrostatic potential as a perturbation to the reference hard sphere potential.

The chain connectivity contribution of the Helmholtz free energy for polyelectrolytes shares the same idea with the general SAFT for neutral polymers [5, 6, 11]. The Helmholtz energy density f^{chain} is given by:

$$f^{chain} = \frac{\rho_m}{r_n}(1 - r_n)\ln y_{mm}(\sigma_{mm}) \tag{4.2.3}$$

where ρ_m is the monomer density, r_n is the number of monomers in a polymer and $y_{ij}(r_{ij})$ is the cavity correlation function(CCF). This is taken to be given by Percus-Yevick approximation.

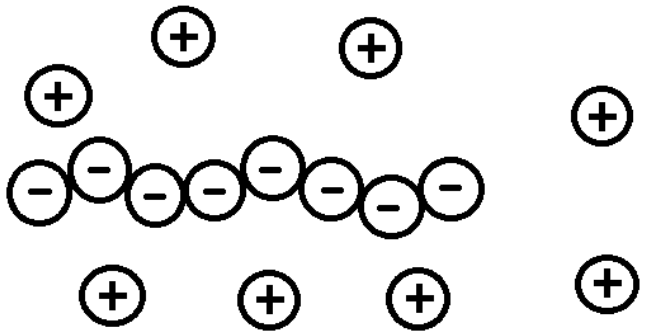

Figure 4.1: A schematic of the polyelectrolyte chain and counterions, $r_n = 8$.

Eq. (4.2.3) clearly indicates that the chain connectivity energy is proportional to the total number of bonds in the system (note that in a r_n-mer, there are $r_n - 1$ bonds). The free energy of each bond is given as a function of CCF which is defined as:

$$y_{ij}(r) = g_{ij}(r) \exp(\beta u_{ij}(r)) \tag{4.2.4}$$

where $u_{ij}(r)$ is the pair potential. For this study, $g_{ij}(r)$ is the EXP-theory result, given in Eq. (3.3.42), and Eq.(3.3.43). The advantage of EXP-theory is that it gives a very good prediction for $g_{ij}(r)$ and there is an explicit analytical expression for $g_{ij}(\sigma)$ which is a quantity we need[12, 13].

Accordingly, Jiang et. al. give the corresponding parts of the pressure as:

$$\beta P^{id} = \sum_s \rho'_s \tag{4.2.5}$$

$$\beta P^{hs} = \frac{\pi\zeta_0\zeta_3}{6} + \frac{\pi\zeta_1\zeta_2}{2\Delta^2} + \frac{\pi^2(2+\Delta)\zeta_2^3}{36\Delta^3} \tag{4.2.6}$$

$$\beta P^{el} = -\frac{\Gamma^3}{3\pi} - \frac{\pi l_B}{2}\left(\frac{P_n}{\Delta}\right)^2 \tag{4.2.7}$$

$$\beta P^{chain} = \frac{\rho_m}{r_n}(1 - r_n)\frac{\partial \ln y_{mm}(\sigma_m)}{\partial \ln \zeta_0} \tag{4.2.8}$$

Note that for the polyelectrolyte system, ρ'_s denotes the polymer density so that for counterions $\rho'_c = \rho_c$ but for the polymer $\rho'_p = \rho_m / r_n$.

The chain connectivity term is expressed in terms of a derivative. An analytical expression for this term can be found in [14]. In this study, the electrostatic interaction is given by the MSA while the $g(r)$ (and hence $y(r)$) used in chain connectivity is given by EXP.

The chemical potential of the canonical ensemble can be written as:

$$\mu = (f + P) / \sum_s \rho'_s \tag{4.2.9}$$

The activity coefficient γ for component s is defined as:

$$\ln \gamma_s = \beta(\mu_s^{ex} - \mu_s^{\ominus}) \tag{4.2.10}$$

where μ_s^{ex} is the excess chemical potential of species s, $\mu_s^{\ominus}$ is the excess chemical potential of species s in a infinite dilute system. In the RPM model, $\mu_s^{\ominus} = 0$. Therefore the activity coefficient γ of the system can also be divided into different parts with respect to different potentials.

$$\ln \gamma_s = \ln \gamma_s^{hs} + \ln \gamma_s^{ele} + \ln \gamma_s^{chain} \tag{4.2.11}$$

where the subscript 's' denotes the species of the particles ($s = p$ indicates the polymers while $s = c$ indicates the counterions). The constituent terms making up the activity coefficients are given by:

$$\ln \gamma_s^{hs} = \begin{cases} r_n \ln \gamma_m^{hs}, & s = p \\ \ln \gamma_c^{hs}, & s = c \end{cases} \tag{4.2.12}$$

The contributions from the monomers ($s = m$) and counterions ($s = c$) are written as:

$$\begin{aligned}\ln\gamma_s^{hs} =& -\ln\Delta + \frac{\pi\sigma_s^3(\beta P^{hs}+\zeta_0)}{6} + \frac{\pi\sigma_s(\sigma_s\zeta_1+\zeta_2)}{2\Delta} \\ &+ \frac{\pi^2\sigma_s^2\zeta_2^2}{8\Delta^2} + 3\left(\frac{\sigma_s\zeta_2}{\zeta_3}\right)^2\left(\ln\Delta + \frac{1-\Delta}{\Delta} - \frac{\pi^2\zeta_3^2}{72\Delta^2}\right) \\ &- \left(\frac{\sigma_s\zeta_2}{\zeta_3}\right)^3\left(2\ln\Delta + \frac{1-\Delta^2}{\Delta}\right)\end{aligned} \tag{4.2.13}$$

Similarly, the electrostatic contribution is:

$$\ln\gamma_s^{el} = \begin{cases} r_n \ln\gamma_m^{el}, & s = p \\ \ln\gamma_c^{el}, & s = c \end{cases} \tag{4.2.14}$$

where $\ln\gamma_s^{el}(s = m, c)$ given by

$$\begin{aligned}\ln\gamma_s^{el} =& \frac{\Gamma a_s z_s/2\pi - l_B z_s^2}{\sigma_s} \\ &- \frac{\sigma_s P_n(\Gamma a_s + \pi^2 l_B\sigma_s^2 P_n/3\Delta)}{4\Delta}\end{aligned} \tag{4.2.15}$$

$$a_s = \frac{2\pi l_B(z_s - \pi P_n\sigma_k^2/2\Delta)}{\Gamma(1+\Gamma\sigma_s)} \tag{4.2.16}$$

For more details on the notation, please refer to the last chapter.

For the chain connectivity term, we have:

$$\ln\gamma_s^{chain} = \begin{cases} (1-r_n)\left[\ln y_{mm}(\sigma_m) + \frac{\partial\ln y_{mm}(\sigma_m)}{\partial\ln\rho_m}\right], & s = p \\ (1-r_n)\frac{\rho_m}{r_n}\frac{\partial\ln y_{mm}(\sigma_m)}{\partial\rho_c}, & s = c \end{cases} \tag{4.2.17}$$

Hence the average activity coefficient is:

$$\ln\gamma_\pm = \frac{\rho_p\ln\gamma_p + \rho_c\ln\gamma_c}{\rho_p+\rho_c} \tag{4.2.18}$$

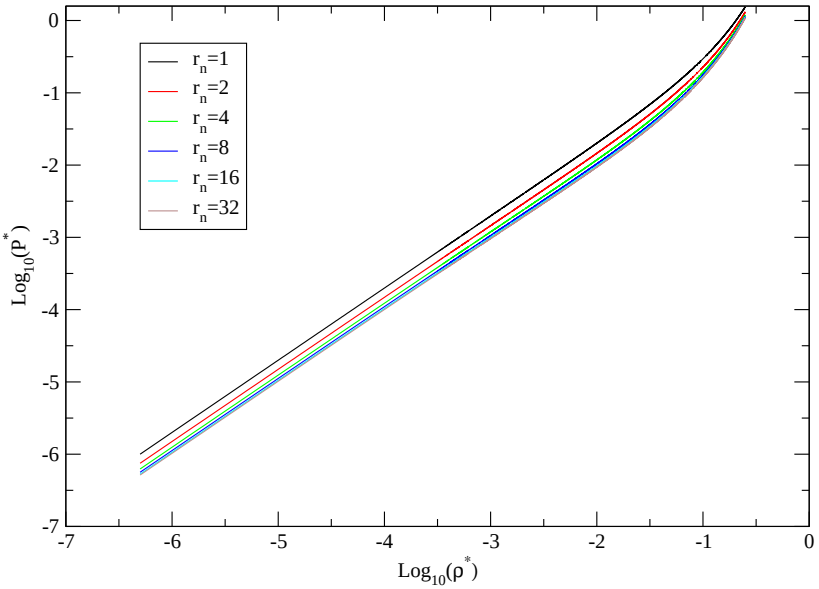

Figure 4.2: The density dependence of the pressure with various chain lengths, $l_B/\sigma = 0.833$.

4.3 Results and Discussions

In this section, we first check whether we can reproduce the results given in [7]. The pressure given by the theory is shown in Fig. (4.2). The corresponding Bjerrum length for the calculation is $l_B = 0.833\sigma$, which is a reasonable choice for a polyelectrolyte solution at room temperature. The density dependence of the pressure is measured by the the scaling parameter δ, where we have $P^* \sim (\rho^*)^\delta$. Odijk [15] has proposed this scaling theory for semi-dilute polyelectrolyte solutions based on the scaling theory by de Gennes [16] for the neutral polymers. The scaling theory predicts semi-quantitative power laws between macroscopic properties of the system (e.g. osmotic pressure) and the concentration of the polyelectrolytes. However, the power law is verified by neutron scattering and viscosity measurements experimentally. Recent Monte-Carlo studies [17] have also proved the correctness of the power law. According to Odijk [15], the scaling parameter for polyelectrolytes is 9/4 for semidilute solutions. For dilute solutions, Monte-Carlo results [17] suggest the scaling coefficient to be 9/8. For the RPM model, the osmotic pressure of the polyelectrolytes equals the total pressure of the system. From Fig. (4.2), if the cross-over density is chosen as $\log_{10}\rho^* \approx -1.1$ (by Jiang et. al. [7]), the scaling parameter δ is approximately 1.1 (slightly less than 1.1 for chains with $r_n < 16$) at low densities with various chain lengths. At high densities, the scaling parameter is approximately 2.0 for short chains and 2.1 for long chains. This result matches Odijk's prediction and is also in good

agreement with the simulation results [17, 18]. However, the choice of the crossover density is a bit arbitrary, and we will discuss this shortly. As we can see from the theory, when the chain length r_n goes to infinity, the only term that affects the result is the chain connectivity term, where we have $\lim_{r_n\to\infty}(1-r_n)/r_n = -1$. Physically, $r_n \to \infty$ indicates that only a single long chain exists in the solution.

Fig. (4.3) shows the density dependence of the polyion activity coefficient with various chain lengths. At the infinite-dilute limit, γ_P tends to be 1 as we expect for the ideal gas limit. As the density increases (before it reaches a certain critical density), γ_p keeps decreasing which means the attractive interaction gets stronger and stronger than the repulsive interaction. In the dilute and semi-dilute regime, $\gamma_p < 1$ shows that the attraction always overwhelms the repulsion. The crossover point on Fig. (4.3) corresponds to $\log_{10}\rho^* = -0.822$ and $\ln\gamma_p = 1.451$. At any lower density, short chains have a larger $\ln\gamma_P$ value than the long chains, while at higher densities the situation goes the other way. Therefore this crossover point seems a good choice to divide the dilute regime from the semi-dilute regime. Above this point, the activity coefficient increases drastically as a result of the hard sphere repulsion. The re-calculated scaling parameter is $\delta = 2.0$ for monomers and $\delta = 2.26$ for 32-mers. This result is in a very good agreement with Odijk's prediction [15]. The scaling parameter is fitted over $10,000$ points in the dilute regime ($\log_{10}\rho^* \sim (-6.3, -0.822)$) and $100,000$ points in the semi-dilute regime ($\log_{10}\rho^* \sim (-0.822, -0.6)$).

Fig. (4.4) demonstrates the density dependence of the counterion activity coefficient with various chain lengths. Note that $r_n = 1$ corresponds to the RPM model, so γ_c is exactly the same as γ_P. The behaviour of γ_c with chain length is similar: $\gamma_c \to 1$ in the infinite-dilute limit, γ_c goes down as the density increases in the dilute regime while in the semi-dilute and concentrate regime, γ_c increases as the density increases. The effect on γ_c due to the chain length is rather small compared with γ_P and again, as $r_n \to \infty$, γ_c will converge to a limiting value. The dependence of the average activity coefficient on density is shown in Fig. (4.5).

This theory can also predict the phase behaviour of polyelectrolytes. The binodal curves for various chain lengths are shown in Fig. (4.6). When $r_n = 1$, the system corresponds to the RPM model. In this case the chain connectivity term does not affect the results. The result for $r_n = 1$ is consistent with Fig.(3.9). The vapour-liquid equilibrium curves show that as r_n

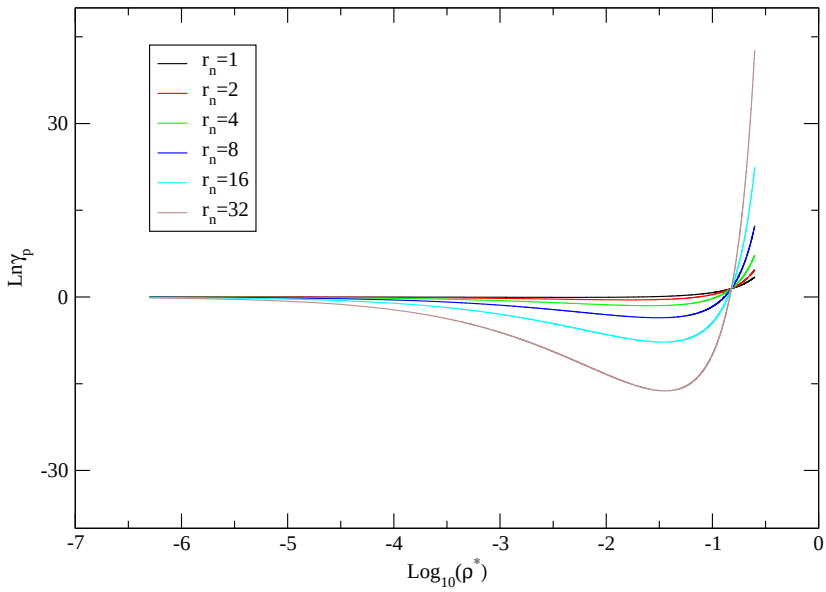

Figure 4.3: The density dependence of the polyion activity coefficient with various chain lengths, $l_B/\sigma = 0.833$.

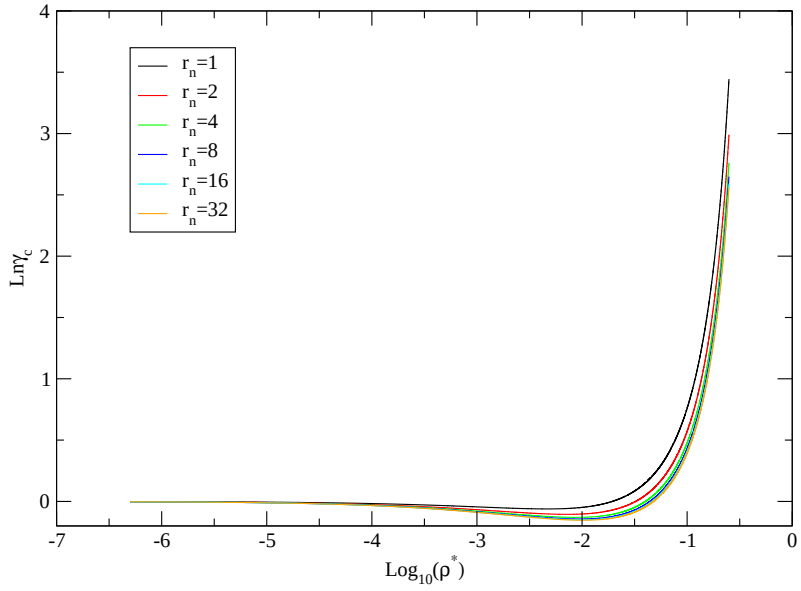

Figure 4.4: The density dependence of the counterion activity coefficient with various chain lengths, $l_B/\sigma = 0.833$.

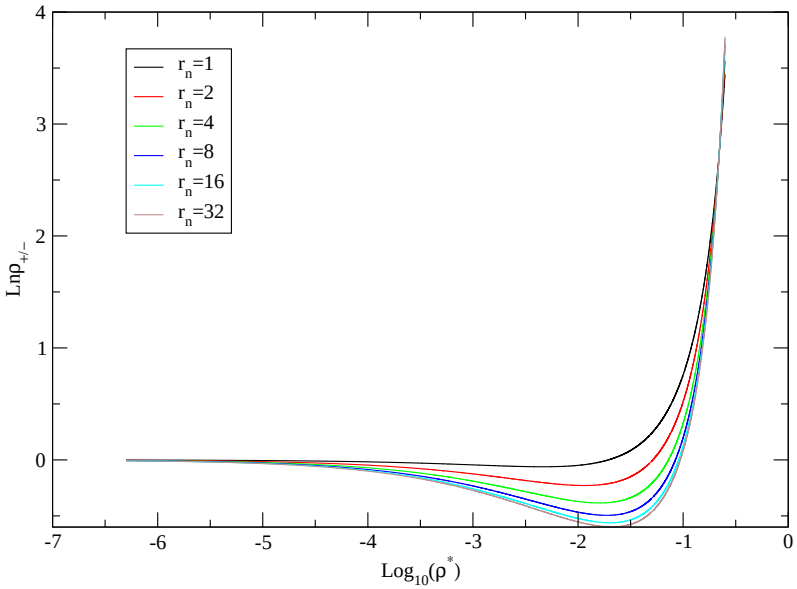

Figure 4.5: The density dependence of the average activity coefficient with various chain lengths, $l_B/\sigma = 0.833$.

increases, the phase separation happens at a higher temperature. The critical temperature raises as r_n increases. These conclusions are qualitatively correct comparing with the simulation results [19, 20]. MC results from [19] are for the RPM model. Results from [20] are molecular dynamics studies for chained particles with a soft-repulsive potential, while water is treated as dielectric continuum (as in the RPM model). However, the vapour pressure given by the theory is too high (see Fig. (4.7)).

4.4 Implementation of Debye-Hückel Theory

In the previous section, we discussed the SAFT-like theory proposed by Jiang et. al. for polyelectrolytes. The theory itself is not entirely consistent. The electrostatic interaction is treated by the mean spherical approximation while $g(r)$ in the chain connectivity term uses the EXP method. Here in this section, we are implementing the DH theory in both electrostatic term and the chain connectivity term. We may replace both MSA and EXP by the Debye-Hückel theory to make the whole theory consistent.

In the previous chapter, we have shown that DH theory gives a good prediction for $g(\sigma)$ for like-pairs. As long as the hard sphere effect is small (which indicates a low density), DH gives a good description for the electrolyte system. In addition, unlike MSA, $g(\sigma)$ provided by DH is

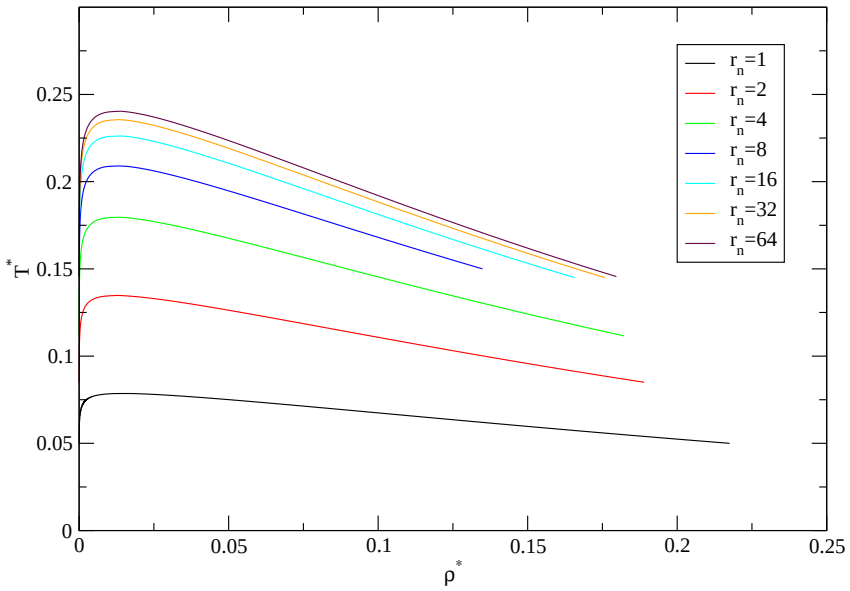

Figure 4.6: Binodal curves with various chain lengths by Jiang's theory.

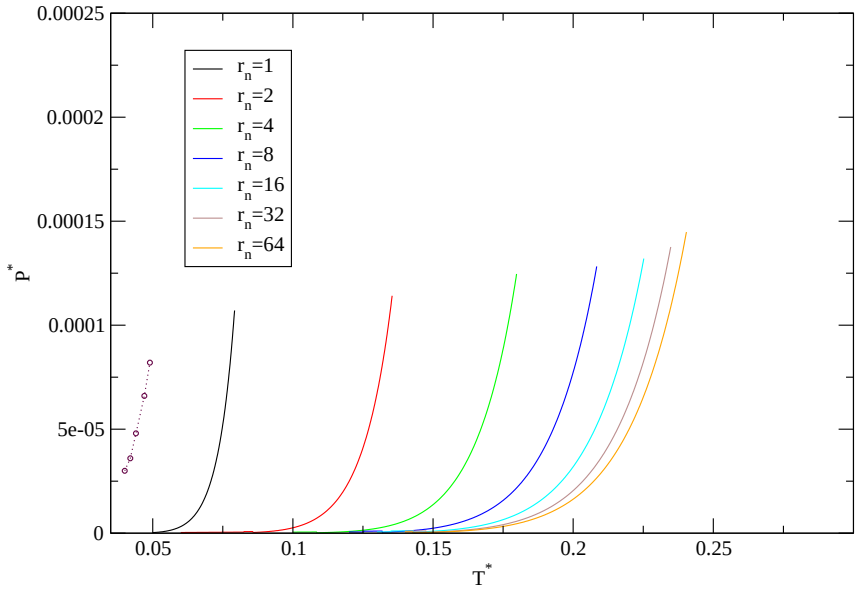

Figure 4.7: Vapour pressures with various chain lengths by Jiang's theory; dotted lines are from MC simulation results for RPM model by Panagiotopolous[19].

always positive and we can use it directly to calculate the chain contribution to the Helmholtz energy.

In the case of DH theory, the corresponding electrostatic terms should be changed to

$$\beta f^{el} = -\frac{1}{4\pi\sigma^3}\left[\ln(\kappa_{\mathbf{D}}\sigma + 1) - \kappa_{\mathbf{D}}\sigma + \frac{(\kappa_{\mathbf{D}}\sigma)^2}{2}\right] \tag{4.4.1}$$

$$\beta P^{el} = -\frac{1}{4\pi\sigma^3}\left[\ln(\kappa_{\mathbf{D}}\sigma + 1) - \frac{\kappa_{\mathbf{D}}\sigma}{2(\kappa_{\mathbf{D}}\sigma + 1)} - \frac{\kappa_{\mathbf{D}}\sigma}{2}\right] \tag{4.4.2}$$

while the chain terms are

$$\beta f^{chain} = \frac{\rho_m}{r_n}(r_n - 1)\frac{l_B}{\sigma}\exp(-\kappa_{\mathbf{D}}\sigma) \tag{4.4.3}$$

$$\beta P^{chain} = \frac{-\kappa_{\mathbf{D}}\sigma}{2}\beta f^{chain} \tag{4.4.4}$$

Correspondingly, the activity coefficient by the electrostatic interaction for RPM is given by

$$\ln\gamma_s^{el} = \begin{cases} r_n \ln\gamma_m^{el}, & s = p \\ \ln\gamma_c^{el}, & s = c \end{cases} \tag{4.4.5}$$

with $\ln\gamma_s^{el}(s = m, c)$

$$\ln\gamma_s^{el} = -\frac{(\sigma\kappa_{\mathbf{D}})^3}{8\pi\sigma^3\rho_s(1 + \kappa_{\mathbf{D}}\sigma)} \tag{4.4.6}$$

The term for the chain connectivity has the same form but we use the $g(r)$ from DH theory. However, the total activity coefficients for the polyelectrolyte chain with different chain lengths do not cross over a constant point (as in the case of Jiang's theory). Therefore we use the cross-over density in Jiang's theory as the boundary of dilute and semi-dilute system.

Fig. (4.8) shows the density dependence of pressure with various chain lengths obtained by the DH theory ($l_B/\sigma = 0.833$). The scaling parameter at low density is $\delta \approx 1.0$, which seems worse than MSA for various chain lengths. In the concentrated regime, $\delta \approx 2.2$ for short chains and $\delta \approx 2.4$ for long chains. This is a better result than the previous MSA+EXP method. However, DH theory should show a better behaviour at low densities rather than at high densities, as been discussed in the previous chapter. Further analysis shows that at low

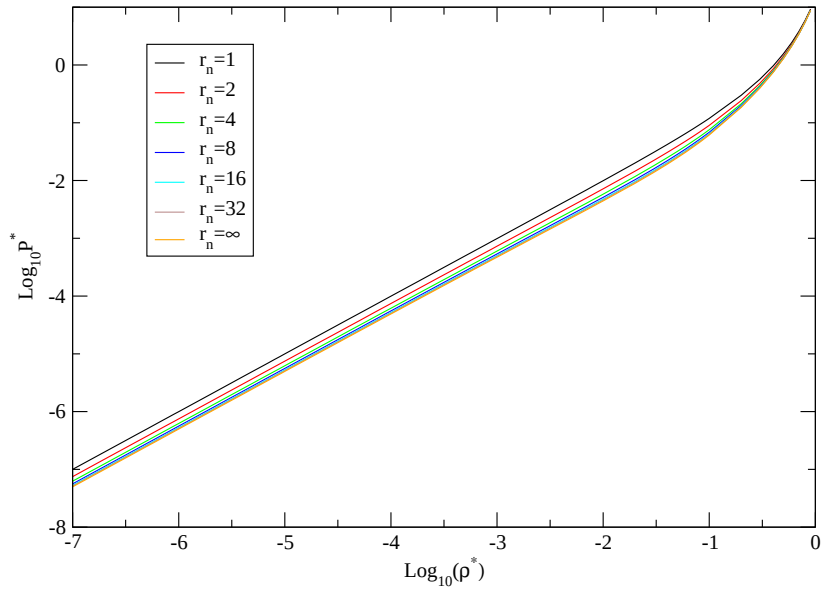

Figure 4.8: The density dependence of the pressure with various chain lengths, by DH theory, $l_B/\sigma = 0.833$.

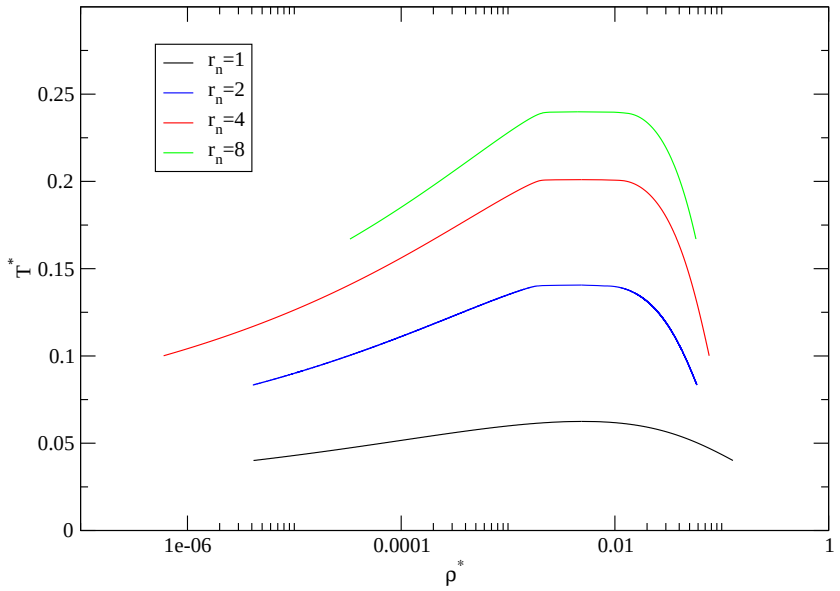

Figure 4.9: Binodal curves from DH theory with various chain lengths.

temperature, the main contribution to the total pressure comes from the ideal gas part. As the density increases, the electrostatic part and the chain part start to show their effects. As the density goes further up, the hard sphere part gives an overwhelming contribution to the other three.

The phase diagrams given by DH theory can also give a qualitatively correct prediction for different chain lengths. For $r_n = 1$, the system goes back to the RPM model and the critical density and critical temperature are the same as given by the DH theory for RPM model. However, just like DH theory is deficient for the RPM model, the critical density for chains is also too low compared with simulation results [19]. Further more, the critical temperature given by DH theory raises drastically as the chain length increases. As Fig. (4.9) shows, the liquid line gets very steep when r_n increases and the reduced critical density is on the magnitude of 10^{-3}. In the case of polyelectrolyte chains, e.g. the oct-mers, the reduced critical temperature is about 0.25, which seems too high [20], even comparing with the MSA results. For the RPM model, DH results are in better line with Monte-Carlo results than MSA results. However, as the chain length increases, the critical temperature goes even higher than the MSA predictions. One possible reason is that in the MSA, the attraction is stronger than in DH. This results in a lower critical temperature for DH theory than that of the in RPM model. But the chain connectivity gives a pure repulsive contribution to the total Helmholtz free energy. For the screened Coulomb potential as in DH theory, the repulsive electrostatic interaction is largely screened out due to low temperature. Therefore the chain connectivity has very limited repulsive contribution to the system. On the other hand, the chain connectivity contribution in the MSA largely cancels out the attractive interaction. This leads to the higher critical temperature for the polyelectrolyte chains in DH theory. In addition, the vapour pressure prediction seems better than MSA but still only semi-quantitatively correct (Fig. (4.10)). It seems that the better consistency in the theoretical treatment of the system does not necessarily bring about a better result.

4.5 Further Discussions

The chain term for a r_n-mer polyelectrolyte chain is calculated as

$$f^{chain} = -\rho_p \ln \left[g\left(\mathbf{r_1}, \mathbf{r_2}, \ldots, \mathbf{r_{r_n}}\right) \cdot \exp\left(\beta u(\mathbf{r_1}, \mathbf{r_2}, \ldots, \mathbf{r_{r_n}})\right) \right] \tag{4.5.1}$$

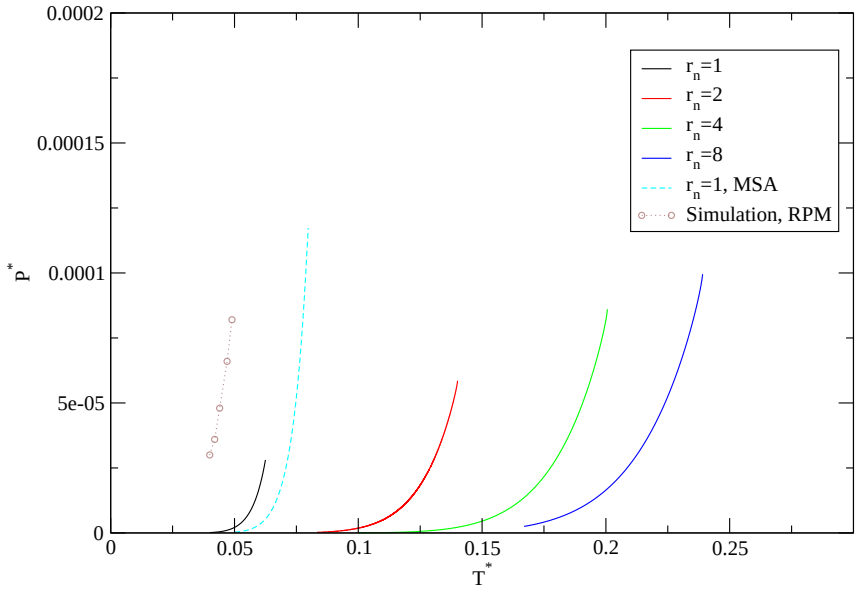

Figure 4.10: The vapour pressure given by DH theory with various chain lengths.

It means for a n-mer, the Helmholtz free energy needed for gathering the r_n particles into such a chain structure is directly related to the n-body distribution function and the r_n-body potential. SAFT makes the important assumption that

$$g(\mathbf{r_1}, \mathbf{r_2}, \ldots, \mathbf{r_{r_n}}) \approx g(\mathbf{r_1}, \mathbf{r_2}) g(\mathbf{r_2}, \mathbf{r_3}) \ldots g(\mathbf{r_{r_{n-1}}}, \mathbf{r_{r_n}}) = g(\sigma)^{n-1} \tag{4.5.2}$$

$$u(\mathbf{r_1}, \mathbf{r_2}, \ldots, \mathbf{r_{r_n}}) = u(\mathbf{r_1}, \mathbf{r_2}) + u(\mathbf{r_2}, \mathbf{r_3}) + \ldots u(\mathbf{r_{r_{n-1}}}, \mathbf{r_{r_n}}) \tag{4.5.3}$$

where we remember that the spheres in the chain are tangentially connected. Eq.(4.5.2) assumes the multibody distribution function can be approximated by the product of the pair distribution functions. In addition, the multibody potential can be described by the sum of all the pair potentials between the consecutive particles. This assumption is in the SAFT theory for neutral polymers [5, 6], where the total chain connectivity for a r_n-mer chain can be treated as the sum of $(r_n - 1)$ pairwise interactions. This seems to be a good assumption for neutral polymers where the interactions between neutral particles is short-ranged. Therefore in a linear chain molecule, we only calculate the free energy contribution by connecting particle pairs $(1, 2)$, $((2, 3) \ldots (r_{n-1}, r_n)$, altogether $r_n - 1$ pairs. Other interactions are ignored since particle 1 and i $(i \neq 2)$ are relatively far apart and the interaction between the two are negligible. However, this assumption is questionable for polyelectrolytes since the Coulombic interaction is a

long-range interaction. There are two obvious ways to improve this approximation. The first one is to bring in higher orders in the radial distribution function approximation:

$$\begin{aligned} g(\mathbf{r_1}, \mathbf{r_2}, \ldots, \mathbf{r_{r_n}}) =& g(\mathbf{r_1}, \mathbf{r_2}) g(\mathbf{r_2}, \mathbf{r_3}) \ldots g(\mathbf{r_{r_{n-1}}}, \mathbf{r_{r_n}}) \\ & \cdot g(\mathbf{r_1}, \mathbf{r_3}) g(\mathbf{r_2}, \mathbf{r_4}) \ldots g(\mathbf{r_{r_{n-2}}}, \mathbf{r_{r_n}}) \\ =& g(\sigma)^{n-1} \cdot g(r')^{n-2} \end{aligned} \tag{4.5.4}$$

where $g(r')$ denotes the radial distribution function between particle i and $i+2$. For the neutral polymers, the inter-particle interaction is so short-ranged that interaction between i and $i+2$ can be ignored. This can also be predicted using the value of $g(r')$. For a dilute neutral hard sphere system, $g(r)$ goes quickly to 1 outside the hard sphere diameter σ. Therefore the value of $g(r')$ is 1 for the dilute system, and Eq. (4.5.4) easily becomes Eq. (4.5.2). For the Coulombic system, $g_{++}(r)$ does not converge to 1 very quickly, even for a dilute system. It all depends on the Bjerrum length of the system. One obvious example is the peak for $g_{++}(r)$ at around 2σ. As Fig. (4.11) shows, for a system with a reduced density $\rho^* = 0.1$, $g_{++}(r)$ shows a clear peak at around $r = 2\sigma$ as the temperature goes down. The significance of Fig. (4.11) is that 1)Based on Eq. (4.5.1) and Eq. (4.5.4), the interaction between particles roughly 2σ away becomes favoured at a low temperature, while at high temperature, it is unfavoured; 2)The value of $g(2\sigma)$ shows that the probability of a particle appearing at 2σ becomes high compared with that of an ideal gas. This peak at this specific position implies that particles at roughly 2σ away with the same charge will contribute quite differently from that in an ideal gas. Therefore, if an RPM model is taken as the reference system, the interaction between particle i and $i+2$ cannot be ignored.

If we take Eq. (4.5.4) as the expression for the chain connectivity term, another issue arises. There is no analytical solution for $g_{++}(r)$ at a specific distance other than σ. Although the DH theory gives a full range of $g(r)$, the theory itself fails to predict the peak at low temperature. The numerical solution of HNC gives a good prediction but it fails at a low temperature. This issue should be further studied.

The other way of improvement is to modify the interaction term $u(\mathbf{r_1}, \mathbf{r_2}, \ldots, \mathbf{r_{r_n}})$ Instead of simply replacing the multibody potential by summing only the pair potential for the pair

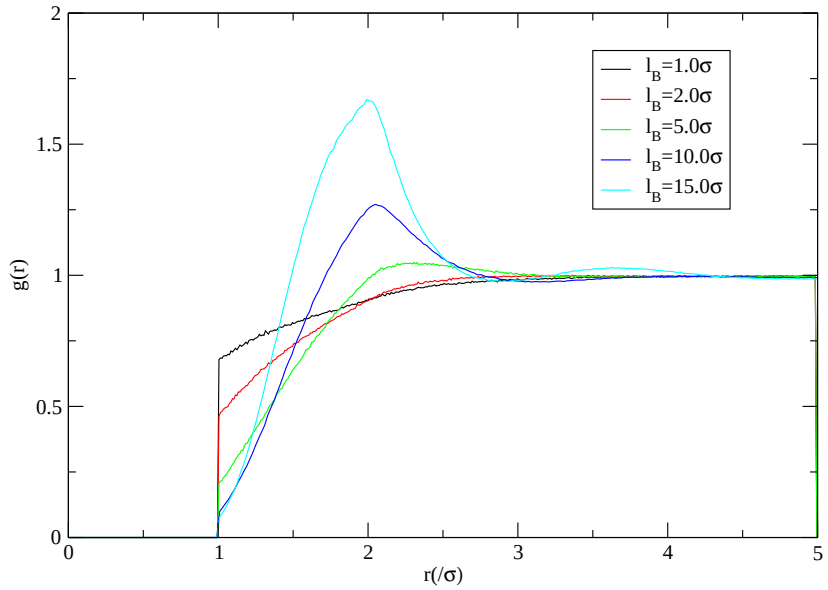

Figure 4.11: The radial distribution function for like-pair with different Bjerrum lengths, MC results for RPM model, $\rho^* = 0.1$.

consisting of consecutive particles in the chain, we can rewrite it as:

$$u(\mathbf{r_1}, \mathbf{r_2}, \ldots, \mathbf{r_n}) = u^{\mathbf{eff}}(\mathbf{r_1}, \mathbf{r_2}) + u^{\mathbf{eff}}(\mathbf{r_2}, \mathbf{r_3}) + \cdots + u^{\mathbf{eff}}(\mathbf{r_{n-1}}, \mathbf{r_n}) \tag{4.5.5}$$

where 'eff' indicates the effective interaction between each pairs. With such treatment, we may incorporate the pair potential by the pairs consisting of particles non-consecutively aligned in the chain (e.g. $u(\mathbf{r_1}, \mathbf{r_3})$). Due to the long range nature of the Coulombic interaction, the interaction term should certainly include the screened interaction between all pairs when being summed in the such a pairwise way.

However, the SAFT itself only gives a method in characterising the polyelectrolytes which is based on the RPM model. Hence the first priority is to get a good description of the RPM model which we will discuss in the next chapter.

4.6 Conclusion

In this section, we used a SAFT-like theory to describe the macroscopic thermodynamic properties of polyelectrolyte solutions. The Helmholtz energy of the system is calculated as the sum of four parts: the ideal gas contribution, the hard sphere contribution, the electrostatic interaction and the chain connectivity contribution. We reproduce the results by Jiang et. al.

who use the mean spherical approximation as the solution of the reference hard sphere electrolyte system and the EXP approximation to calculate the chain connectivity term. We also implement the Debye-Hückel theory into this SAFT-like theory. The total pressure prediction is better than the MSA in terms of the scaling parameter for the polyelectrolyte chains. It also predicts the phase separation of the polyelectrolyte chains, but in spite of the improved predictions for monomer, the critical temperature seems too high. Furthermore, a better assumption for the chain connectivity is proposed.

4.7 References

[1] M.S. Wertheim. “Fluids with Highly Directional Attractive Forces. I. Statistical Thermodynamics”. In: *Journal of Statistical Physics* 35 (1984), pp. 19–34. See p. 52.

[2] M.S. Wertheim. “Fluids with Highly Directional Attractive Forces. II. Thermodynamic Perturbation Theory and Integral Equations”. In: *Journal of Statistical Physics* 35 (1984), pp. 35–47. See p. 52.

[3] M.S. Wertheim. “Fluids with Highly Directional Attractive Forces. III. Multiple Attraction Sites”. In: *Journal of Statistical Physics* 34 (1986), pp. 459–476. See p. 52.

[4] M.S. Wertheim. “Fluids with Highly Directional Attractive Forces. IV. Equilibrium Polymerization”. In: *Journal of Statistical Physics* 42 (1986), pp. 477–492. See p. 52.

[5] E.A. Müller and K.E. Gubbins. “Molecular-Based Equations of State for Associating Fluids: A Review of SAFT and Related Approaches”. In: *Industry and Engineering of Chemical Research* 40 (2001), pp. 2193–2221. See pp. 52, 53, 65.

[6] A. Gil-Villegas et al. “Statistical associating fluid theory for chain molecules with attractive potentials of variable range”. In: *Journal of Chemical Physics* 106 (1997), pp. 4186–4204. See pp. 52, 53, 65.

[7] J.W. Jiang et al. “Thermodynamic properties and phase equilibria of charged hard sphere chain model for polyelectrolyte solutions”. In: *Molecular Physics* 99 (2001), pp. 1121–1128. See pp. 52, 57.

[8] N.F. Carnahan and K.E. Starling. “Equation of State for Nonattracting Rigid Spheres”. In: *The Journal of Chemical Physics* 51 (1969), pp. 635–636. See p. 53.

[9] T. Boublík. “Hard-Sphere Equation of State”. In: *The Journal of Chemical Physics* 53 (1970), pp. 471–472. See p. 53.

[10] G.A. Mansoori et al. “Equilibrium Thermodynamic Properties of the Mixture of Hard Spheres”. In: *The Journal of Chemical Physics* 54 (1971), pp. 1523–1525. See p. 53.

[11] P. Paricaud, A. Galindo, and G. Jackson. “Modeling the Cloud Curves and the Solubility of Gases in Amorphous and Semicrystalline Polyethylene with the SAFT-VR Approach and Flory Theory of Crystallization”. In: *Industry and Engineering of Chemical Research* 43 (2004), pp. 6871–6889. See p. 53.

[12] L. Blum. “Mean spherical model for asymmetric electrolytes. I. Method of solution”. In: *Molecular Physics* 30 (1975), pp. 1529–1535. See p. 54.

[13] L. Blum and J.S. Hoye. “Mean spherical model for asymmetric electrolytes. 2. Thermodynamic properties and the pair correlation function”. In: *The Journal of Physical Chemistry* 81 (1977), pp. 1311–1316. See p. 54.

[14] J. Jiang et al. “A molecular-thermodynamic model for polyelectrolyte solutions”. In: *The Journal of Chemical Physics* 108 (1998), pp. 780–784. See p. 55.

[15] T. Odijk. “Possible Scaling Relations for Semidilute Polyelectrolyte Solutions”. In: *Macromolecules* 12 (1979), pp. 688–693. See pp. 57, 58.

[16] P.G. de Gennes. *Scaling Concepts in Polymer Physics*. Cornell University Press, 1979. See p. 57.

[17] M.J. Stevens and K. Kremer. “The nature of flexible linear polyelectrolytes in salt free solution: A molecular dynamics study”. In: *Journal of Chemical Physics* 103 (1995), pp. 1669–1690. See pp. 57, 58.

[18] M.J. Stevens and K. Kremer. “Structure of Salt-Free Linear Polyelectrolytes”. In: *Physical Review Letters* 71 (1993), pp. 2228–2231. See p. 58.

[19] G. Orkoulas and A.Z. Panatiotopoulos. “Free energy and phase equilibria for the restricted primitive model of ionic fluids from Monte Carlo simulations”. In: *Journal of Chemical Physics* 101 (1994), pp. 1452–1459. See pp. 60, 61, 64.

[20] A. Karatrantos. PhD thesis. University of Manchester, 2010. See pp. 60, 64.

CHAPTER

FIVE

HYPERNETTED CHAIN AND ASSOCIATION THEORY

5.1 Introduction

In the last chapter, we described a reasonable method of treating the polyelectrolyte chains making use of a RPM model. However, as discussed in Chapter 3, current theories do not provide a good description of phase separation for the RPM model. In this section, we are going to propose a new approximate theory for the RPM model. Firstly, we will discuss the numerical solution of the hypernetted chain (HNC) equation. Secondly, we will review the association theory proposed by Wertheim [1, 2] for strong short-ranged attractive interactions. After that, a new approximate theory for the RPM system is proposed which combines HNC with association theory. This new theory gives good predictions for the phase separation behaviour as compared to Monte-Carlo simulations.

5.2 Theory and Expressions

5.2.1 Numerical Solution for Hypernetted Chain

To begin with, we recall the expression for the HNC closure [3]

$$g(r) = \exp\left[h(r) - c(r) - \beta u(r)\right] \tag{5.2.1}$$

If we define an auxillary function $e(r)$, where

$$e(r) = h(r) - c(r) \tag{5.2.2}$$

the radial distribution function can be written as

$$g(r) = \exp\left[e(r) - \beta u(r)\right] \tag{5.2.3}$$

In terms of diagrammatic expansions [3], $e(r)$ is the sum of all the nodal diagrams. The use of this auxilliary function is convenient in the numerical solution which will be discussed shortly.

HNC is widely used in the study of charged system [4, 5], especially for the one-component classical plasma (OCP) [6]. OCP consists of a large assembly of identical point charges with a uniform charged background to make the system electrically neutral. In OCP, we define the ion-sphere radius to be $a_{OCP} = (3/4\pi\rho)^{1/3}$. Since all the particles in OCP are point charges, a_{OCP} is the characteristic length describing the average distance between two point charges. An important parameter of the OCP system is $\Gamma_{OCP} = e^2/ak_BT$. As mentioned in previous chapters, HNC only works for binary electrostatic systems with a relatively short Bjerrum length. At low temperatures, HNC no longer has a real solution but only complex solutions which have no physical meaning [7]. However, when a solution can be found, HNC gives very good results in agreement with Monte-Carlo simulations. For the OCP system, Ng has proposed numerical techniques which allow HNC solutions to be found up to $\Gamma_{OCP} \sim 7000$. In this section we use some of the techniques which Ng has used for OCP systems [6], and these techniques work very well with binary Coulomb systems.

The Coulomb potential is long-ranged with a decay proportional to $1/r$. We divide the total interaction into two parts, the long-range part (denoted with a subscript 'l') and the short-range part (denoted with a subscript 's'). It has been established that as $r \to \infty$, $c(r)$ tends to $-\beta u(r)$, which indicates asymptotically $c_l(r) \to -\beta u_l(r)$.

According to the treatment by Stevens et. al.[8], we have

$$u(r) = u_s(r) + u_l(r) \tag{5.2.4}$$

$$e_s(r) = e(r) - u_l(r) \tag{5.2.5}$$

$$c_s(r) = c(r) + u_l(r) \tag{5.2.6}$$

The $u_l(r)$ is chosen to have the same asymptotic form as $e(r)$, so that we try to find solutions for the following functions:

$$\hat{e}_s(k) = \hat{c}(k)/[1 - \rho\hat{c}(k)] - \hat{c}_s(k) \tag{5.2.7}$$

$$g(r) = \exp\left[e_s(r) - \beta u_s(r)\right] \tag{5.2.8}$$

$$c_s(r) = h(r) - e_s(r) \tag{5.2.9}$$

With a careful choice of the split of the potential $u_s(r)$ and $u_l(r)$, the above equations can be solved numerically using the iteration methods. For our RPM system, we write the two parts of the Coulombic potential in the form

$$\beta u_l(r) = (l_B/r)\text{erf}(\kappa r) \tag{5.2.10}$$

$$\beta u_s(r) = (l_B/r)\text{erfc}(\kappa r) \tag{5.2.11}$$

where $\text{erf}(x)$ is the error function and $\text{erfc}(x)$ is the complementary error function, defined as

$$\text{erf}(x) = \frac{2}{\sqrt{\pi}} \int_0^x e^{-t^2}\, dt \tag{5.2.12}$$

$$\text{erfc}(x) = 1 - \text{erf}(x) \tag{5.2.13}$$

The reason for such a choice is that the Fourier transformation of the error function has a simple analytical expression. The Fourier transformation of the two parts are respectively

$$\beta\hat{u}_l(k) = (4\pi l_B/k^2)\exp(-k^2/4\kappa^2) \tag{5.2.14}$$

$$\beta\hat{u}_s(k) = (4\pi l_B/k^2)[1 - \exp(-k^2/4\kappa^2)] \tag{5.2.15}$$

Therefore, the short-range part decays very fast as the complementary error function decays quickly to 0. The choice of κ does not affect the final results since both parts of the Coulombic potental are used in the calculations. For the convenience of calculations, $\kappa\sigma$ usually takes the value between 0.5 to 2.0 [6]. Various regular iteration methods are available such as Picard's method and Newton-Raphson's method [9]. Ng [6] has proposed a new iteration methods which converges very quickly. A combination of Picard's method and Ng's method is applied in this study. The details can be found in Appedix A.

5.2.2 Association Theory

The association model is proposed by Wertheim [1, 2] in order to treat strong, short-ranged attractions between particles. This theory describes the system with highly directional attractive force. Various studies [1, 10] show that the shape of the molecules will affect the association, however, the association theory presented here is only applicable to spherical or nearly spherical molecules [10].

When the inter-molecular pair potential is small, one can calculate the thermodynamic properties of the system using perturbation theory [3]. However, when the interaction gets stronger, the perturbation theory fails and the association theory comes to the rescue [1, 10, 11].

The Helmholtz free energy density given by the association theory is expressed as

$$\begin{aligned}\beta f^{assoc} =& \beta f^{total} - \beta f^{ref} \\ =& \sum_{\alpha} \rho_{\alpha} \left[\sum_{B \in \Gamma^{(\alpha)}} \left(\ln X_B^{(\alpha)} - \frac{X_B^{(\alpha)}}{2} \right) + \frac{1}{2} n(\Gamma^{(\alpha)}) \right]\end{aligned} \tag{5.2.16}$$

The Greek letter α indicates the component α, therefore ρ_α is the number density of component α. The English letter B indicates the association site on the molecules. $X_B^{(\alpha)}$ is the fraction of component α **not** bonded at site B and $n\left(\Gamma^{(\alpha)}\right)$ is the number of bonding sites in the set $\Gamma^{(\alpha)}$. As shown in Eq. (5.2.16), there are two sums: the first is the summation over all components and the second is over all sites of the component. The term $X_B^{(\alpha)}$ can be obtained from the

mass-action equation

$$X_B^{(\alpha)} = \left[1 + \sum_{\gamma} \sum_{A \in \Gamma(\gamma)} \rho_\gamma X_A^{(\gamma)} \Delta_{AB}^{(\alpha\gamma)}\right]^{-1} \tag{5.2.17}$$

and the term $\Delta_{AB}^{(\alpha\gamma)}$ is defined by

$$\begin{aligned} \Delta_{AB}^{\alpha\gamma} =& \int g_R^{(\alpha\gamma)}(r) f_{AB}^{(\alpha\gamma)}(r)\, \mathrm{d}\mathbf{r} \\ =& 4\pi \int g_R^{(\alpha\gamma)}(r) f_{AB}^{(\alpha\gamma)}(r)\, r^2 \mathrm{d}r \end{aligned} \tag{5.2.18}$$

$f_{AB}^{(\alpha\gamma)}(r) = \exp(-\beta\Phi_{AB}^{(\alpha\gamma)}(r)) - 1$ is the Mayer f-function, $g_R^{(\alpha\gamma)}(r)$ is the radial distribution function for the reference fluid and $\Phi_{AB}^{(\alpha\gamma)}(r)$ is the attractive interaction between site A on species α and site B on species γ. With the knowledge of $g_R^{(\alpha\gamma)}(r)$ for the reference fluid, the properties of the associating fluid can be calculated. A detailed explanation of the association theory using diagrammatic expressions is provided by Wertheim [1, 2].

The association theory has been shown to be in good agreement with MC simulation results [10, 11] for various systems with strong short-ranged attractions, such as water with its hydrogen bonding interactions.

5.2.3 A New Theory for the Restricted Primitive Model

The new theory presented here splits the interaction potential described earlier in this chapter and then uses association theory to treat the short-ranged attractions. The aim is to provide better predictions of the thermodynamic properties of the restricted primitive model. As discussed in Chapter 3, existing theories suffer from certain defects when treating long-ranged Coulombic interactions. HNC lacks solutions when the temperature goes too low and gives poor results when the density goes high [7]. EXP gives good prediction of $g_{++}(\sigma)$ but for the unlike pairs(+ -), the prediction is poor, as shown in Fig. (5.1). In fact, all these theories overestimate the value of $g_{+-}(\sigma)$. As the temperature goes further down, the discrepancies get bigger and bigger. A likely reason is that the attraction between the unlike pairs is very strong when the pair is only separated by a short distance. This effect gets stronger as the Bjerrum length gets bigger (e.g. as l_B approaches the critical region). One might consider defining the pair potential for the

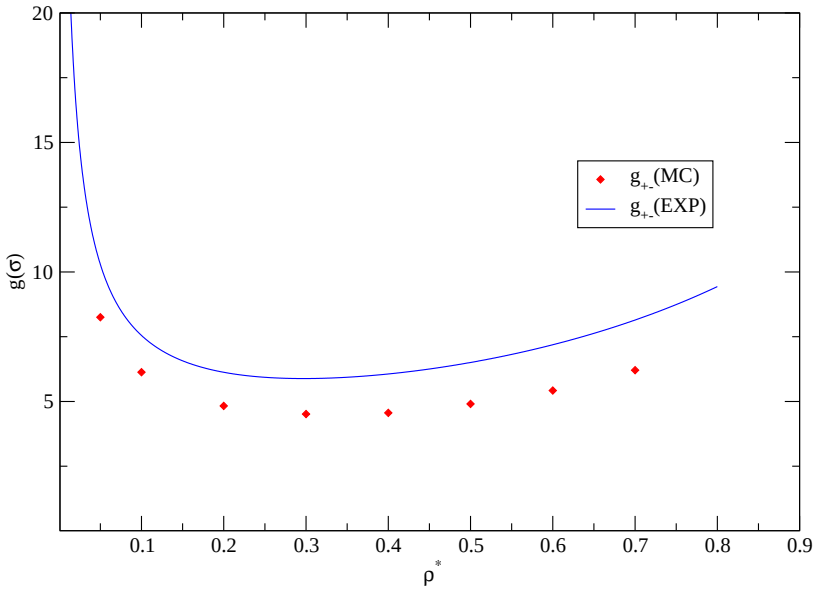

Figure 5.1: The radial distribution function at contact for unlike pairs given by Monte-Carlo simulation and EXP theory, $l_B/\sigma = 2.5$.

reference system as

$$\beta u^{ref}_{like}(r) = \begin{cases} \beta u^{HS}, & r < \sigma \\ l_B/r, & r \geq \sigma \end{cases} \tag{5.2.19}$$

$$\beta u^{ref}_{unlike}(r) = \begin{cases} \beta u^{HS}, & r < \sigma \\ 0, & r \geq \sigma \end{cases} \tag{5.2.20}$$

In this case, however, the attractive interaction is $-l_B/r$. If this were to be used in the association expression, one obtains a divergent integral in $\Delta^{\alpha\gamma}_{AB}$ as shown in Eq. (5.2.18), and the method fails.

As a result of this discussion, we construct a reference system with the full-range of Coulombic repulsion for the like-pairs and only the long-range part of the attraction for the unlike-pairs,

which can be expressed as

$$\beta u^{ref}_{like}(r) = \begin{cases} \beta u^{HS}, & r < \sigma \\ l_B/r, & r \geq \sigma \end{cases} \tag{5.2.21}$$

$$u^{ref}_{unlike}(r) = \begin{cases} \beta u^{HS}, & r < \sigma \\ -(l_B/r)\text{erf}(\kappa r), & r \geq \sigma \end{cases} \tag{5.2.22}$$

where the strong short-ranged attraction can be properly treated as the association. An example of the split potential for the unlike pairs can be seen in Fig.(5.2). The long-range part of the attractive Coulombic potential is used in the reference fluid, while the short-range part is treated by the association theory. As shown in Fig.(5.2), the range and strength of the attraction is controlled by the split parameter κ.

We borrow the concept of 'association' from the proper association theory [1, 2]. A good analogy to the association is that of chemical bonds between two active groups. The groups may be different in shapes and they may have different positions for the sites between which chemical bonds can form. For instance, CO_2 has a bond angle of 180^o while NO_2 has a bond angle of 115^o. This indicates that with the same spherical shape, different particles (C or N in this case) may have their association sites at different positions. However, with our theory for the RPM model, the attraction does not depend on the position of the 'association sites'. Moreover, we artificially put the 'virtual association sites' on the centres of ions and counterions. The advantages of constructing such a reference system are: (1) The thermodynamic properties of the reference system can be easily compared with Monte-Carlo simulations; (2) Given a proper choice of the splitting parameter 'κ', HNC can produce a solution for a wide range of densities even at a low temperature. Looking at the first advantage, in Monte-Carlo simulations the Ewald summation [12–14] is used to calculate the total electrostatic interactions, where a similar split of potential is used. The short-range interactions are calculated in real space while the long-range part is calculated in Fourier space. The Monte-Carlo simulation can be easily tuned to match the reference system so that we can verify the accuracy of the HNC solution for such a reference system. Looking at the second advantage, without the strong short-range attraction HNC gives a good solution for the reference system over a wide range of temperatures

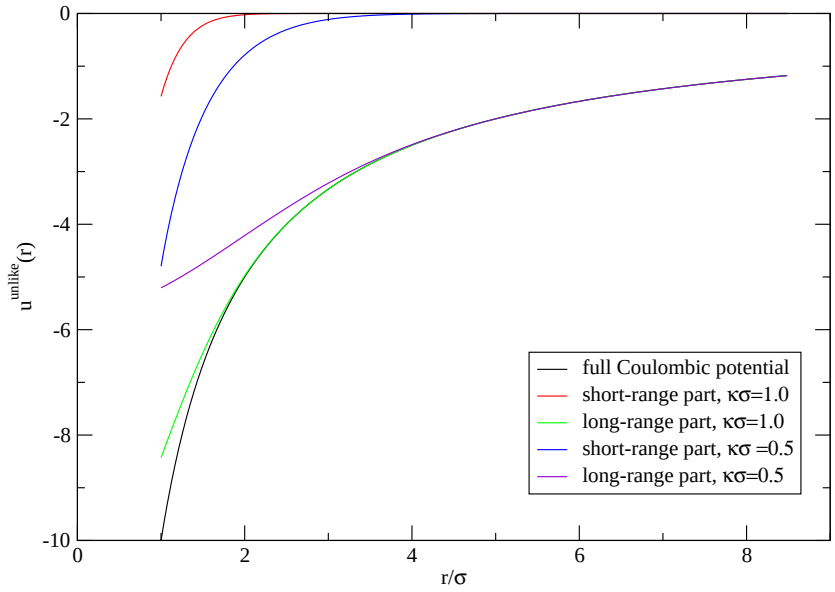

Figure 5.2: An example of the split potential for unlike pairs outside the core, $l_B/\sigma = 10.0$.

and densities.

Fig. (5.3) clearly shows the two advantages of such a split. HNC gives a good prediction for the radial distribution functions of the reference fluid with a slight overestimate of the $g_{+-}(\sigma)$. The Bjerrum length of the reference system is 9.0σ with a reduced density $\rho^* = 0.3$. In the full-potential system, HNC fails to give a solution. The value of the split parameter $\kappa\sigma \approx 0.558$ corresponding to the best choice of the MC simulation.

The excess Helmholtz energy density given by HNC has an explicit analytical expression [15–17], written as

$$\begin{aligned} f^{ex} = &-\frac{1}{2}\sum_{\alpha\gamma}\rho_\alpha\rho_\gamma\int \mathrm{d}\mathbf{r}\{h_{\alpha\gamma}(r) - e_{\alpha\gamma}(r)\} \\ &+\frac{1}{2}\int \mathrm{d}\mathbf{r}\{\mathrm{Tr}[\mathcal{E}(r)\rho\mathcal{H}(r)\rho] - \frac{1}{2}\mathrm{Tr}[\mathcal{H}(r)\rho]^2 + \mathrm{Tr}[\mathcal{C}(r)\rho\mathcal{H}(r)\rho]\} \\ &+\frac{1}{2}\int \frac{\mathrm{d}\mathbf{k}}{(2\pi)^3}\{\mathrm{Tr}[\rho\hat{\mathcal{C}}(k)] + \ln\det[1-\rho\hat{\mathcal{C}}(k)]\} \end{aligned} \tag{5.2.23}$$

$\mathcal{H}(r)$ and $\mathcal{C}(r)$ are matrices containing the pair and direct correlation functions respectively and are defined in Eq.(3.3.22) and Eq.(3.3.23). $\hat{\mathcal{C}}(k)$ is the Fourier transform of $\mathcal{C}(r)$. 'Tr' denotes the trace of a matrix. $\mathcal{E}(r)$ denotes the auxiliary function matrix. In the case of the RPM model,

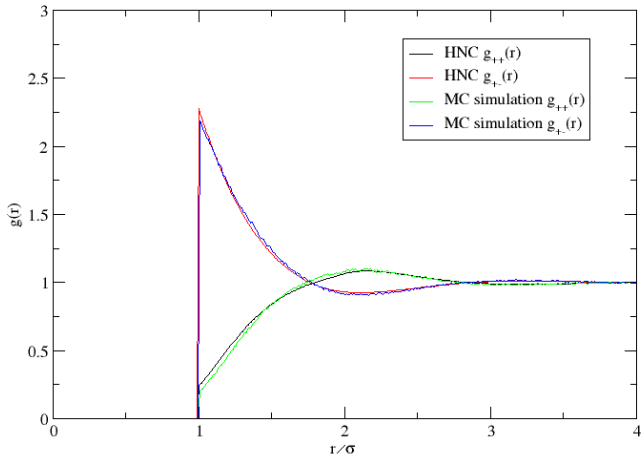

Figure 5.3: Comparison of radial distribution functions for the reference fluid by MC and HNC, $l_B/\sigma = 9.0, \rho^* = 0.3, \kappa\sigma = 0.558$.

this is given by

$$\begin{aligned}\mathcal{E}(r) &= \begin{pmatrix} e_{++}(r) & e_{+-}(r) \\ e_{-+}(r) & e_{--}(r) \end{pmatrix} \\ &= \begin{pmatrix} h_{++}(r) - c_{++}(r) & h_{+-}(r) - c_{+-}(r) \\ h_{-+}(r) - c_{-+}(r) & h_{--}(r) - c_{--}(r) \end{pmatrix}\end{aligned} \tag{5.2.24}$$

Since the RPM model only has two components: the positively charged hard spheres and the negatively charged hard spheres, Eq. (5.2.23) can be simplified to

$$\begin{aligned}\beta f^{ex} = &- \pi\rho^2 \int \mathrm{d}r(c_{++}(r) + c_{+-}(r))r^2 \\ &+ \frac{\rho^2}{2} \int \mathrm{d}r(h_{++}^2(r) + h_{+-}^2(r))r^2 \\ &+ \frac{1}{8\pi^2} \int \mathrm{d}k[\rho(\hat{c}_{++}(k) + \hat{c}_{+-}(k)) + \ln((1 - \rho\hat{c}_{++}(k)/2)^2 - (\rho\hat{c}_{+-}(k)/2)^2)]k^2\end{aligned} \tag{5.2.25}$$

There is an alternative expression given in [18], which uses Parseval's theorem to give a slightly different but equivalent expression. The numerical result are identical in both cases.

The total Helmholtz energy density then is written as:

$$f^{tot} = f^{id} + f^{ex}_{ref} + f^{assoc} \tag{5.2.26}$$

In this case, the site-site attraction for the association is $\Phi^{\alpha,\gamma}_{AB}(r) = -l_B \text{erfc}(\kappa r)/r$. Because of the approximations, the total Helmholtz energy density depends on the choice of the split parameter 'κ' (as shown in Fig.(5.2)). The true Helmholtz energy, naturally, is independent of 'κ'. Instead of an arbitrary choice (like Bjerrum did in his association theory for RPM [19]), one reasonable choice is to ensure

$$\left(\frac{\partial f}{\partial \kappa}\right)_{\kappa=\kappa_0} = 0 \tag{5.2.27}$$

Eq. (5.2.27) gives two reasons for such a choice:
(I) With this condition, the first order perturbation of the Helmholtz free energy with respect to κ is zero

$$(df)_{\kappa_0} = \left(\frac{\partial f}{\partial \kappa}\right)_{\kappa_0} d\kappa = 0 \tag{5.2.28}$$

(II) it turns out to correspond to a local minimum of the Helmholtz energy. As shown in Fig. (5.4), f is high when κ is sufficiently small. It goes down to the minimum at the specific value κ_0, and then goes up again. This briefly demonstrates that when κ is small, a large part of the Coulombic attractive interaction has been treated as the association. The system becomes a reference fluid with very weak long-range interactions plus a 'long-range' strong association. This disobeys the presumption that the association should be short-ranged. On the other hand, when κ becomes large, the association interaction is sufficiently short-ranged and weak, leaving the reference fluid with almost identical to the full range Coulombic interaction, in which case HNC cannot find a solution at low temperatures.

5.3 Results and Discussions

The procedure we follow is as follows: We fix the density and temperature of the system and then vary the value of κ. We calculate the Helmholtz energy density corresponding to each κ to

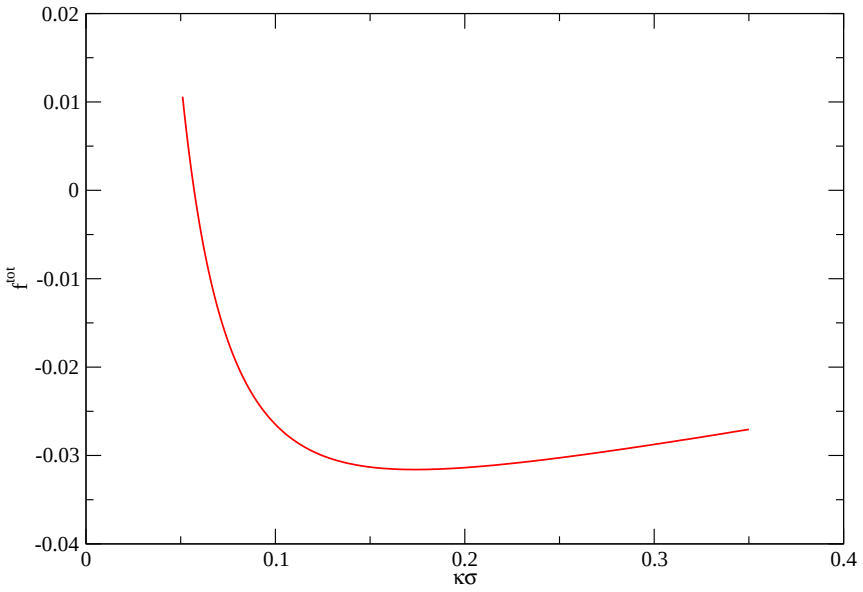

Figure 5.4: An example of the total Helmholtz energy density with different κ values, $l_B/\sigma = 5.0, \rho^* = 0.1$, with one-site.

find the minimum κ_0. The corresponding f, μ and P are recorded. The procedure is repeated over a wide range of densities ρ and also repeated over a range of temperature T in order to find the phase equilibrium. Therefore in this section, we are going to show some calculation results based on the association model for the restricted primitive electolyte solutions. As we mentioned before, the association concept is borrowed from the real association systems, therefore we are going to follow the assumptions that the number of the association sites can only be integer numbers. However, the positions of the sites are not restricted (i.e. the spherical shape does not play a part here). We should note that, Eq. (5.2.17) usually needs computer regression for multiple association sites in the conventional association theory. Fortunately, due to the special association we choose here, it can be solved analytically.

In order to find the phase separation below the critical temperature, two conditions should be satisfied

$$\begin{cases} P^1 &= P^2 \\ \mu^1 &= \mu^2 \end{cases} \tag{5.3.1}$$

with the same temperature, assuming the two phases are denoted as 1 and 2. Given a temperature under which phase separation happens, if we plot the chemical potential μ against the pressure P (this also being applicable in reduced units), we may find a loop in the graph indicating such

a phase separation. This is shown in Fig. (5.5).

5.3.1 One-site Theory

The straight forward expression for the number of association sites between a positively charged ion and a negatively charged ion is 1 (i.e. $n(\Gamma^{(+)}) = n(\Gamma^{(-)}) = 1$). This means the only aggregated configuration that can exist in the system is the (+ -) pair. This is reasonable since various studies have given the snap shots [20] of systems near the critical region where a good number of pairs are formed (even for size-asymmetric case). Another proof would be the high peak of $g_{+-}(\sigma)$for the RPM model[21], indicating the high possibility of forming an unlike pair. Since only one association site is allowed on each particle, we can easily solve Eq.(5.2.17):

$$X^{(+)} = X^{(-)} = \frac{-1 + \sqrt{1 + 2\rho\Delta^{+-}}}{\rho\Delta^{+-}} \tag{5.3.2}$$

The problem is that when the temperature is below the critical point, the theory cannot give a solution for the liquid line of the phase diagram. We fail to find a κ_0 for which Eq.(5.2.27) is satisfied. The reason is with a relatively high density as in the liquid line, the κ_0 value should be quite big as shown in Fig. (5.12). With such a κ_0 value, the long range part of the Coulombic potential is very close to the full Coulombic potential therefore HNC cannot produce the solution for the reference fluid. Further study shows that under those circumstances $\kappa_0 \to \infty$. However, taking into account that HNC does not do well for a high density from the classical theories, if we take MSA on the liquid side, the phase prediction is surprisingly good apart from missing solutions in the critical region (see Fig. (5.7)). The phase equilibrium can be found by a similar plot to Fig.(5.5), but we do not have the spinodal information. As a result of the 'hybrid' theory, we have the plot as shown in Fig.(5.6). We thus calculated the vapour properties as described previously (HNC + association), but used the MSA for the liquid properties.

The gap in the critical region is due to the fact that we have used two independent theories for the two legs of the binodal curve. Inside that gap, we cannot get a pair of density points on the binodal curve for a given temperature. Within that region, two theories cannot provide any pairs of density points such that with those densities, the system has the same chemical

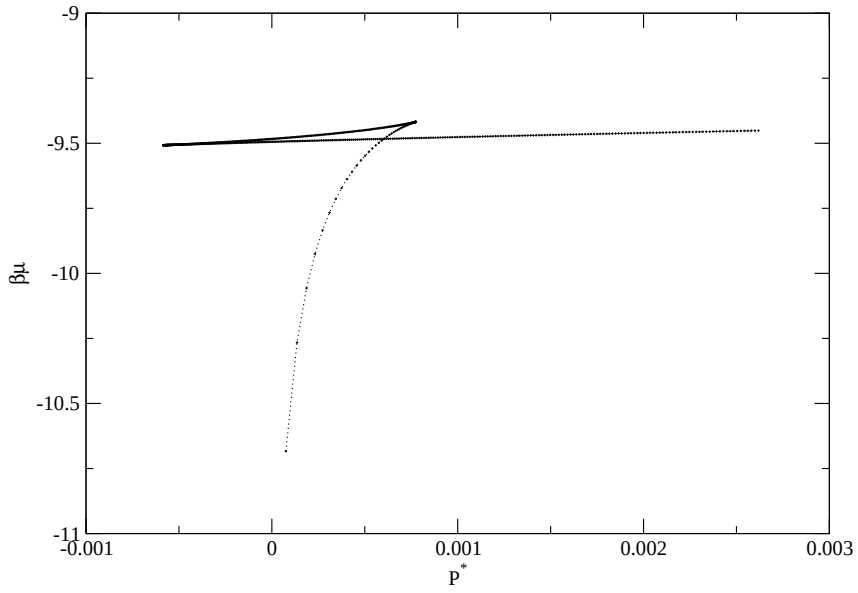

Figure 5.5: An example of the plot of the chemical potential against the pressure indicating a phase separation from MSA theory, $l_B/\sigma = 13.5$.

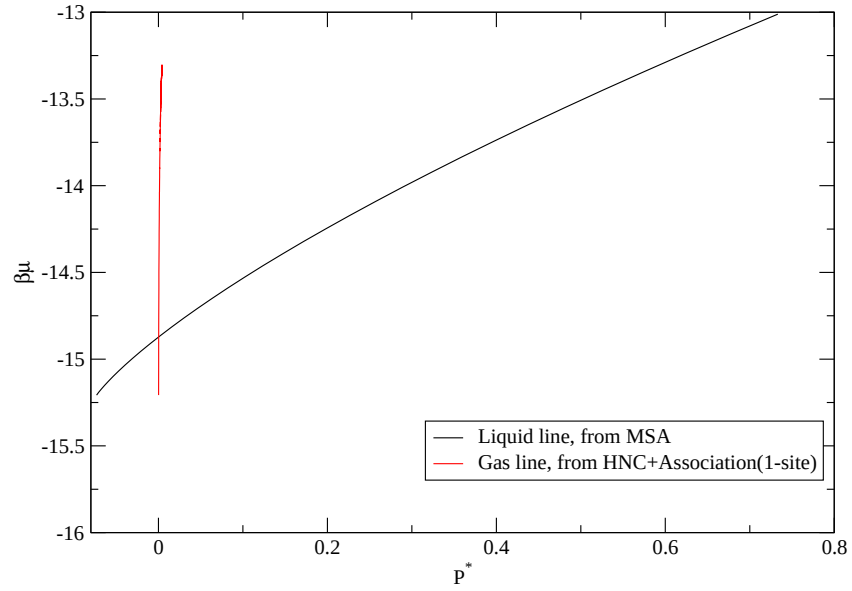

Figure 5.6: An example of the plot of the chemical potential against the pressure for a phase separation from MSA + (HNC + Association with 1-site), $l_B/\sigma = 23.0$.

potential and pressure.

In addition, we also compare our results to some MD simulation results [23] for a soft-repulsive primitive model. The repulsive potential is given as

$$V(r) = \begin{cases} 4\epsilon\left[\left(\frac{\sigma}{r}\right)^{12} - \left(\frac{\sigma}{r}\right)^{6}\right] + \epsilon, r < 2^{\frac{1}{6}}\sigma \\ 0, r \geq 2^{\frac{1}{6}}\sigma \end{cases} \tag{5.3.3}$$

where σ is the diameter of the soft core, and ϵ is the well depth of the potential. The simulation parameters are given as $\sigma = 4.9 \times 10^{-10}$m, $\epsilon = 3.61862$kJ/mol. These parameters correspond to

$$\frac{\epsilon}{k_B T} = 1.0017\frac{l_B}{\sigma} \tag{5.3.4}$$

In order to solve the liquid side of the phase line by MSA, we use Barker's approximation [3] to convert the soft-core into an equivalent hard core by calculating

$$d_B = \int_0^\infty \{1 - \exp[-\beta V(r)]\}\, \mathrm{d}r \tag{5.3.5}$$

The results for the soft repulsive particles are not as good as the results for the hard sphere ones. The gas-line underestimates the equilibrium density but still it is much better than the pure MSA solutions.

5.3.2 Two-sites Theory

Fig .(4.11) indicates that at low temperatures, $g_{++}(r)$ shows a strong peak at around $r = 2\sigma$. This suggests that at low temperatures, the electrolytes may well form short chain structures (e.g. +-+-) or triplets (e.g. +-+) instead of pairs (+-). Or put another way, one charged particle may bind with more than one counterion when the temperature gets lower. At least two association sites are needed for such structures. The nature of the association theory is that even we have two association sites on each particle, those sites are not necessarily occupied. In the case of two association sites, we not only add in the possibility of short chain structure formation but we also allow for simple pair structures at low temperature. The interaction between each

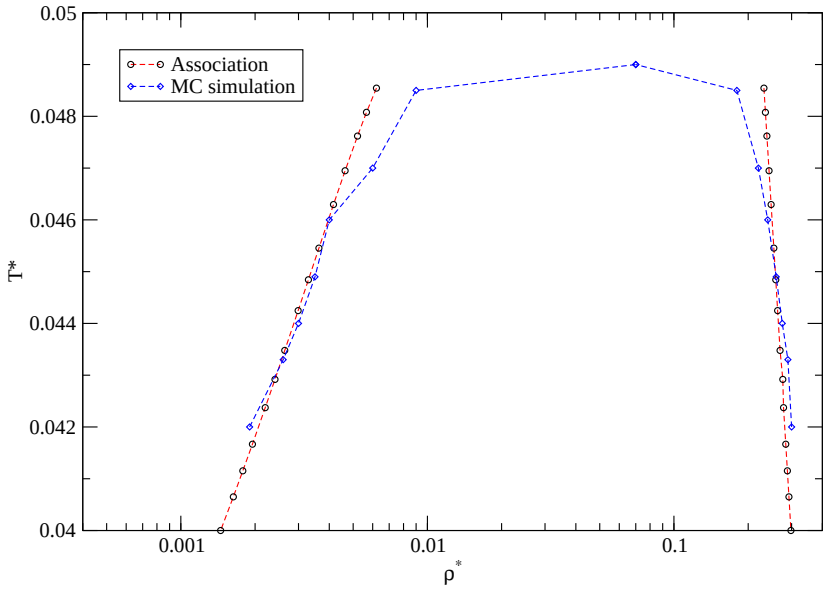

Figure 5.7: The phase diagram given by the one-site association theory for the restricted primitive model, Monte-Carlo results are from Panagiotopoulos et. al.[22].

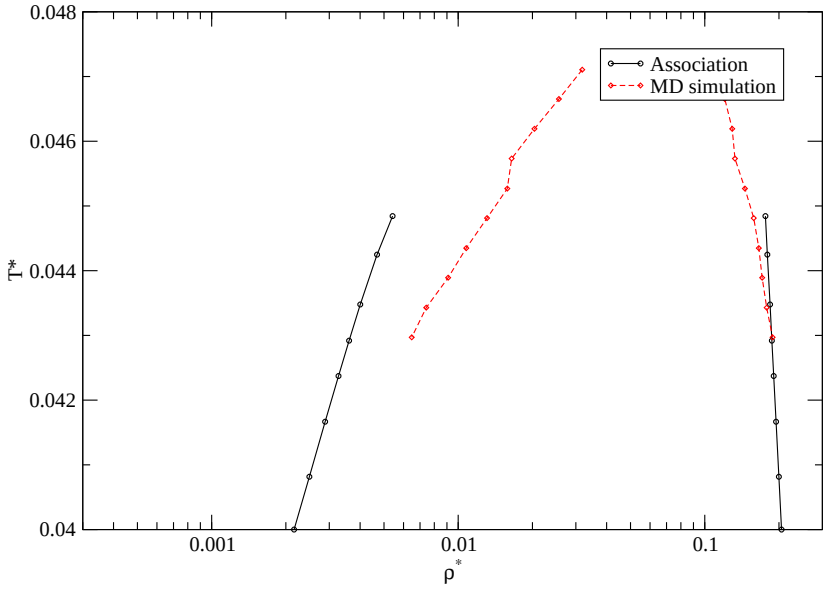

Figure 5.8: The phase diagram given by the one-site association theory for a soft repuslive primitive model, the MD results are from Karantrantos[23].

pair of association sites is identical. By using two association sites, our theory works in fact for both the gas phase and the liquid phase. Thus, we obtain solutions for both the gas and liquid phases using HNC and association theory. With two association sites, the theory can produce a full phase diagram (including the critical point) for the gas-liquid phase separation of the RPM electrolytes, as shown in Fig. (5.9). Effectively, the attraction in the system has increased due to the increase in the number of association sites. As a result, the gas-line largely overestimates the equilibrium density for the gas phase. The reason is that those two association sites give a better opportunity for the particles to associate which pushes the equilibrium density to a higher value for the gas-phase. However, with such assumption, the reduced critical density $\rho_c^* \approx 0.0698$ is very close to the simulation result; correspondingly the critical temperature is calculated to be $T_c^* \approx 0.0723$, also qualitatively correct. These results are reasonably good comparing with the MSA, though both this association theory and the MSA do not get a good prediction for the gas-phase. The MSA gives extremely low coexisting gas-phase densities, while our association theory overestimates the coexisting gas-phase densities.

5.3.3 Multiple Sites Theory

In order to get a better understanding of the short-range association, we hereby tune the number of association sites, n, to other values ($n \neq 1$ or 2).

Considering the fact that: (i) The interaction between the like pairs are already calculated in the reference fluid; (ii) In the two-sites theory, the maximal association interaction caused by a particle is namely $2u^{\alpha\gamma}(r)$, we therefore constrain the interaction between the associating sites to be $\frac{2u^{\alpha\gamma}}{n}$.

The reason to renormalise the attractive potential is that: for a given value of $\kappa\sigma$, more interaction sites simply mean stronger association free energy (which is negative). Therefore for in order to meet $\frac{\partial f}{\partial \kappa} = 0$, more interaction sites will lead to higher value of $\kappa\sigma$. However, as shown in Fig.(5.4), a greater $\kappa\sigma$ means the reference potential gets closer to the full Coulomb potential. HNC will fail to find a solution for the reference fluid for those high values of $\kappa\sigma$. Therefore we have to renormalise the attractive potential on an empirical basis ($n = 3$ still works with the raw potential but fails with $n = 4$.).

With this renormalised potential, we have tried the cases where the number of association

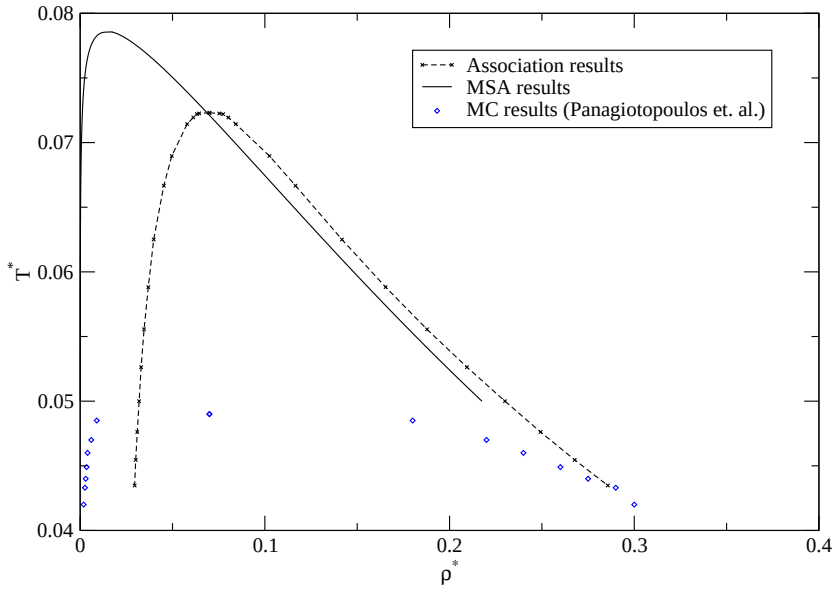

Figure 5.9: The phase diagram given by the association theory with 2 association sites, the MC results are from Panagiotopolous et. al.[22, 24].

sites n equals 3 and 4. These situations correspond to the high-order clustering of the electrolytes in the critical region [20]. The phase diagrams are shown in Fig. (5.10).

With the increasing number of associating sites, the binodal curve fits better and better with the simulation results. As shown in Fig. (5.10), the prediction of the gas-phase line is improving as the increasing number of sites. The critical temperature is moving towards the simulation result as well. The reason might be that, with the increasing number of associating sites, based on our assumption, the association energy between each pair of associating sites are effectively reduced and therefore a weaker association is achieved. This helps to better characterise the gas-phase for the RPM electrolytes. In addition, the multiple association sites allow more complicated structure to form in the critical region, where snaps shots [20] under such conditions suggest the same. However, when $n > 4$, the code itself cannot give a full range of the binodal curve but only part of it. As shown in the figure, when $n = 5$, the critical temperature goes higher than the value gained by setting $n = 4$, however, the shape of the critical region is quite close to the MC results where the plateu in the critical region gets quite broad. In comparison with the classical theories, where for the case of MSA, the reduced critical temperature is approximately $T^*_{crit} \approx 0.0786$ [25, 26]; for BIMSA-EXP, $T^*_{crit} \approx 0.0627$ [27], where $g(r)$ of the RPM system is treated by EXP theory (as we did in the last chapter); our theory gives a much better prediction about the critical temperature, especially for the association results with $n = 4$,

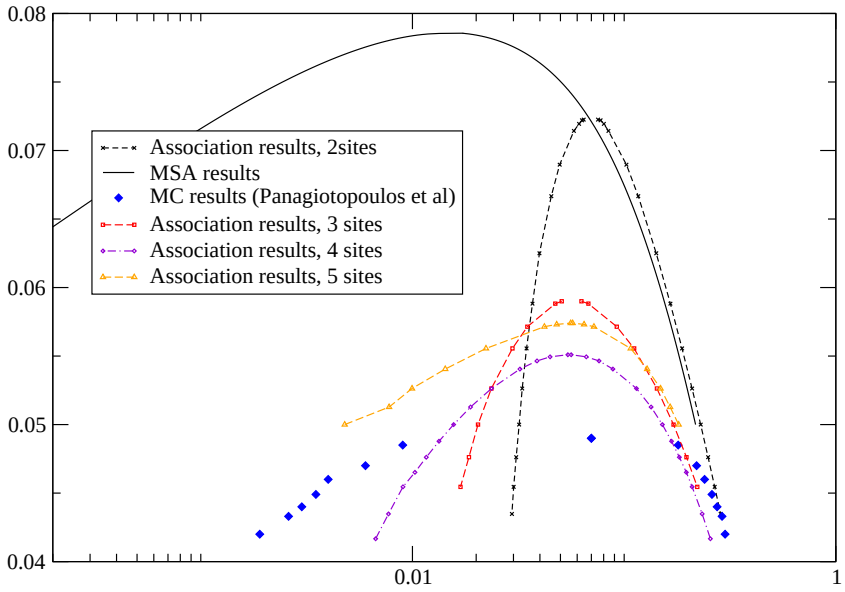

Figure 5.10: Phase diagrams given by the association theory with multiple association sites, MC results are from Panagiotopoulos et. al.[22, 24].

where the critical temperature $T^*_{crit} \approx 0.0551$. This result is better than most of the theories, including the results from Kalyuzhnyi [28], which is perhaps the best available. Kalyuzhnyi's theory is based on the polymer mean-spherical approximation, which is used to study linear polymers. A similar concept of splitting the potential is used in his theory.

Regarding the critical density, our theory gives reasonably good results as well. The reduced density given are correspondingly: $n = 2, \rho^*_{crit} \approx 0.0698; n = 3, \rho^*_{crit} \approx 0.0553; n = 4, \rho^*_{crit} \approx 0.0548$ and $n = 5, \rho^*_{crit} \approx 0.0565$. These results are as good as some of the most sophisticated theories, such as DHBjCIHC (Debye-Hückel + Bjerrum association + Cluster-Ion interaction + Hard core) theory given by Fisher et. al. [29] which is based on the Debye-Hückel theory plus ion-clustering treatment or the associating-MSA theory proposed by Kalyuzhnyi [28].

Another important critical property for the RPM model is the vapour pressure, which is shown in Fig. (5.11).

Fig. (5.11) shows that the association theory gives qualitatively correct predictions about the vapour pressure of the RPM system. The 2-sites theory has largely overestimated the vapour pressure. As the number of sites increases, the results are getting better. The 4-sites theory gives the closest fit as compared to MC results. In addition, the vapour pressure given by the 4-sites theory is closer to the ones from MC data [30], than any other theory. It overestimates the vapour pressure by a factor of about 2.

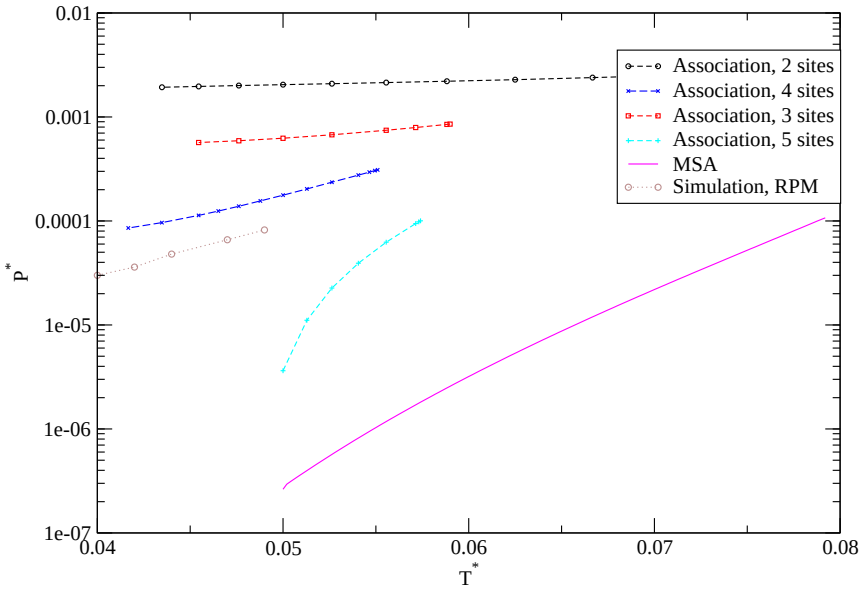

Figure 5.11: The vapour pressure given by the association theory with various sites.

5.3.4 Discussion about the Parameter κ_0

For the one-site association theory, the behaviour of κ_0 is shown in Fig. (5.12). It shows that the value of κ_0 increases as the density of the system increases. This means when the system becomes dense, the range of the association gets shorter. In addition, the strength of the short-range potential gets weaker as κ_0 increases. This effect is analogous to the Debye screening effect. When the temperature is high, κ_0 indicates there to be weaker association compared to the system at a lower temperature. The short range interaction $l_B \text{erfc}(\kappa_0 r)/r$ gets weaker as κ_0 gets bigger. The behaviour of κ_0 for the multiple sites theory is shown in Fig. (5.13). Since the behaviour of κ_0 for the multiple site theories are similar, here we take $n = 4$ as an example. κ_0 exhibits a similar behaviour to the inverse Debye screening length. The value becomes big as the density or Bjerrum length gets big. Physically, κ_0 tries to maintain the strength of the short range association as the temperature goes up, which makes the association theory valid at high temeratures. However, in very dilute systems at a low temperature, we see some crossover points on the κ_0 curve. This behaviour is undesirable and it possibly is due to the renormalisation of the association potential. The exact analytical expression for the κ_0 value in this multiple sites association theory is not available.

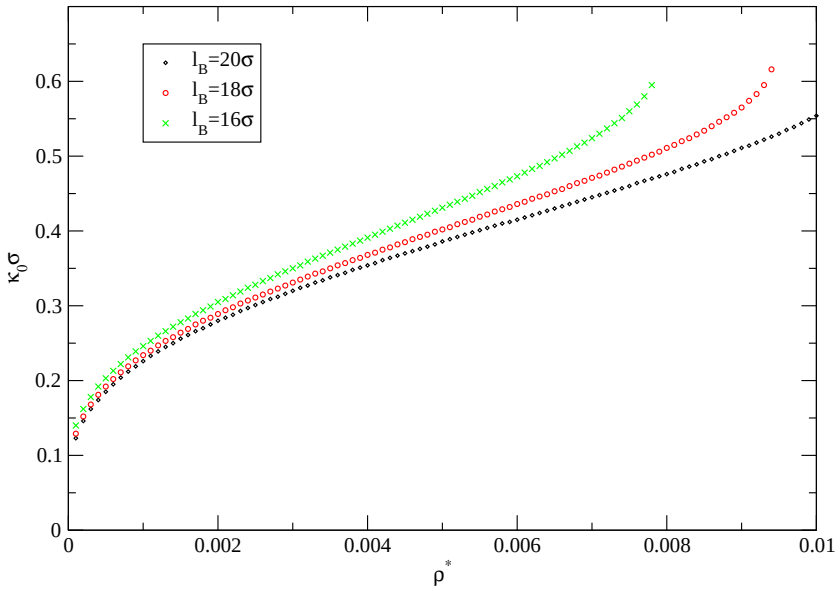

Figure 5.12: An example of the value of κ_0 with different ρ^* under different temperatures with one association site.

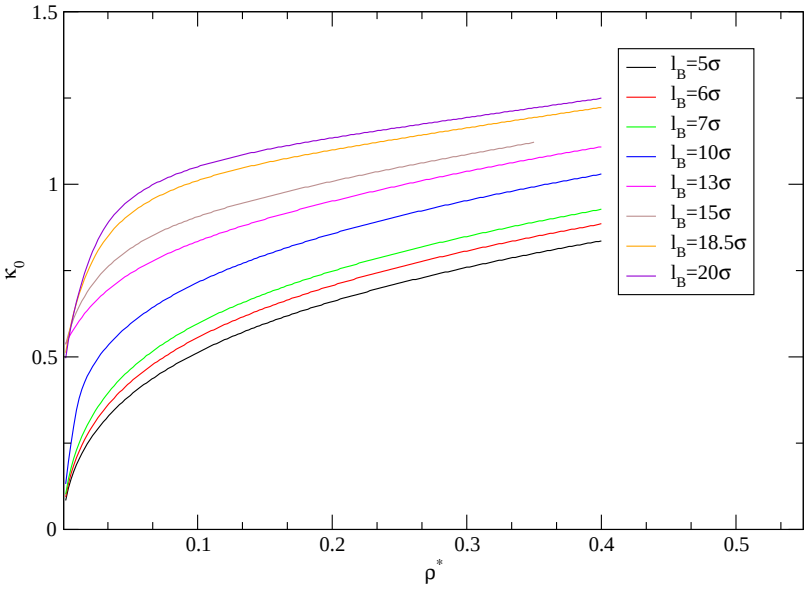

Figure 5.13: A typical behaviour of κ_0 with multiple bonding sites ($n = 4$).

5.3.5 Primitive Model and the Extension of the Association Theory

A primitive model treats the solvent (normally water) as a dielectric continuum, but the solute electrolytes may have different diameters and charges. According to the the differences between the electrolytes, the primitive model can be further divided into size-asymmetric [31] and charge-asymmetric [32, 33] categories. Theories such as mean spherical approximation or Debye-Hückel theory give fairly good predictions for the simple RPM model, but fail for either kind of asymmetric case.

Further to the definition given above, we define the reduced variables for the primitive model as follows:

$$T^* = \frac{\bar{\sigma}}{l_B|z_+z_-|} \tag{5.3.6}$$

$$\rho^* = \rho\bar{\sigma}^3 \tag{5.3.7}$$

$$P^* = \beta P\bar{\sigma}^3 T^* \tag{5.3.8}$$

where $\bar{\sigma} = (\sigma_+ + \sigma_-)/2$ is the average diameter.

Charge-asymmetric Primitive Model

The charge-asymmetric primitive model has been studied [32, 33] to give a further understanding of the physical basis for of electrolyte phase separation [34, 35]. One usually defines the system as $z:1$ charge-asymmetry, indicating one component of the system carries only one elementary charge e, while the other component carries ze with the opposite sign. The diameter of both types of particles are identical, denoted as σ. Monte-Carlo simulations have suggested that as z increases, the reduced critical temperature drops [33]. In addition, the gas-phase line moves to a higher density as z increases. However, from the definition given above, the critical temperature and density do not change according to DH theory [36]. Other theories such as MSA, cannot give a proper prediction of the phase separation either [19]. In fact, the phase diagrams given by MSA for the $z:1$ charge-asymmetric primitive model are exactly identical to the restricted primitive model. The situation is the same for DH theory.

The only theory which can predict such a trend is the so-called "DHBjDIHC" theory (Debye-Hückel theory + Bjerrum association + Dipole-Ion interaction + Hard Core) proposed by Fisher

et. al [33]. An important part of that theory is the calculation of the dipole-ion interaction. The calculation involves some complications with the spherical approximation where they treat the pair (+-) as a spherical dipole while triplets (+(2-)+) are taken to be spherical quadrupoles. The approximation of the spherical dipole depends on the type of the $z:1$ system and thus a general expression is hard to obtain. On the other hand, our association theory can also semi-quantitatively predict the phase behaviour of the charge-asymmetric primitive model.

The assumption we are making in the theory is the same as that for the restricted primitive model: For a particle carrying one elementary charge with 2 sites, it can associate with a maximum of two counterpart sites, with each association potential given by

$$\begin{aligned} u_{ij}^0(r) &= l_B z_i z_j \text{erfc}(\kappa_0 r)/r \\ &= l_B z \text{erfc}(\kappa_0 r)/r \end{aligned} \tag{5.3.9}$$

Therefore for a 2-sites particle, the total association potential is $2u_{ij}^0(r)$. If we increase the number of association sites, the association potential on each site should be $u_{ij}(r) = 2u_{ij}^0(r)/n$, where n is the number of association sites on the particle carrying the elementary charge. This assumption ensures the total association potential on the particle with an elementary charge is constantly $2u_{ij}^0(r)$. As for the particle carrying a charge of ze, the number of association sites is then naturally nz. In order to maintain electrical neutrality, we have

$$\rho_+|z_+| = \rho_-|z_-| \tag{5.3.10}$$

and this relation naturally leads to

$$\rho_+ n_+ = \rho_- n_- \tag{5.3.11}$$

which means in the system we have equal numbers of total association sites on both cations and anions.

The assumption made above means that in a charge-asymmetric primitive model, if we have component A with $(+2e)$ and B $(-e)$, each A particle will have 4 association sites while a B particle has 2. When association happens, the maximal association potential upon B is

$2 \times 2l_B\text{erfc}(\kappa_0 r)/r$ while for A it is $4 \times 2l_B\text{erfc}(\kappa_0 r)/r$.

Recalling Eq. (5.2.16)(5.2.18) and (5.2.17), for a $z:1$ charge-asymmetric primitive model, Eq. (5.2.17) can be re-written as

$$X^+ = \left[1 + \rho_- n_- X^+ \Delta^{+-}\right]^{-1} \tag{5.3.12}$$

$$X^- = \left[1 + \rho_+ n_+ X^- \Delta^{+-}\right]^{-1} \tag{5.3.13}$$

Considering Eq. (5.3.11), the above two equations are symmetric, which indicates $X^+ = X^-$. Hence from Eq. (5.2.16), we have

$$\begin{aligned} f^{assoc} = \rho_+ &\left[n_+ \left(\ln X^+ - \frac{X^+}{2}\right) + \frac{n_+}{2}\right] \\ + \rho_- &\left[n_- \left(\ln X^- - \frac{X^-}{2}\right) + \frac{n_-}{2}\right] \end{aligned} \tag{5.3.14}$$

Given Eq. (5.3.11), the association contribution from cations equals the contribution by anions, indicating the self-consistency of the theory.

For the restricted primitive model, 4-sites association seems to be a good choice and hence we only focus on 4-sites association here. In this case, the association potential for the $2:1$ primitive model is $u(r) = \frac{4l_B\text{erfc}(\kappa_0 r)}{4r}$, while for the $3:1$ primitive model, it is correspondingly $u(r) = \frac{6l_B\text{erfc}(\kappa_0 r)}{4r}$.

The binodal curves are shown in Fig. (5.14). When z increases, the phase separation happens at a lower reduced temperature. This is in reasonable agreement with the Monte-Carlo simulation results [33]. In addition, the critical point moves to a lower reduced temperature and higher density as z increase from 1 to 3, This is also qualitatively consistent with the simulation results. However, it seems that the theory largely overestimates the gas-line density but underestimates the critical temperature.

The critical properties given by various theories are shown in Fig. (5.15) and (5.16). The association theory produces better results than the classical theories and the results are comparable to those of DHBjCI theory [29]. The DHBjCI theory has been extensively studied by Fisher et. al [33]. (DHBjCI means Debye-Hückel theory with Bjerrum association and Cluster-Ion interactions.) That theory uses a different perspective to study the electrostatic system but shows good agreement with the simulation results.

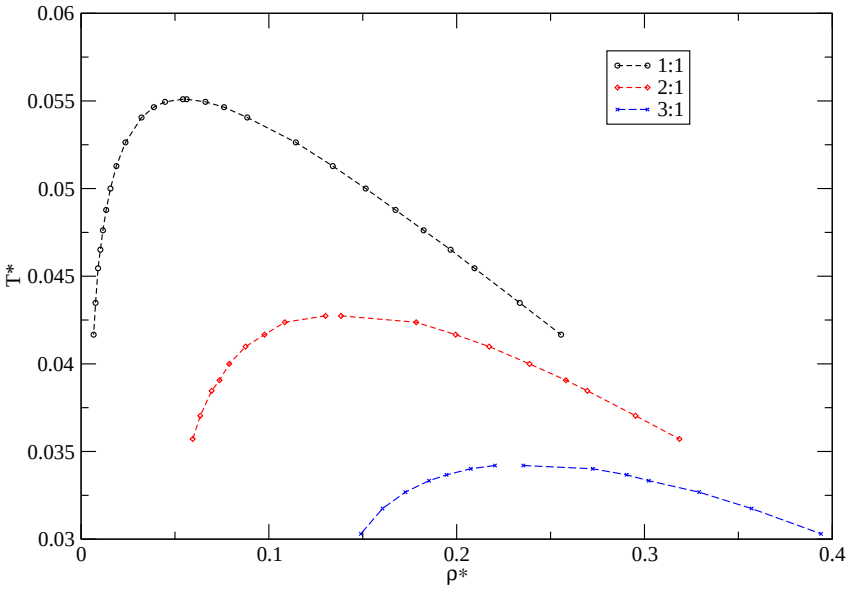

Figure 5.14: Binodal curves for $z:1$ charge-asymmetric primitive models calculated from the association theory.

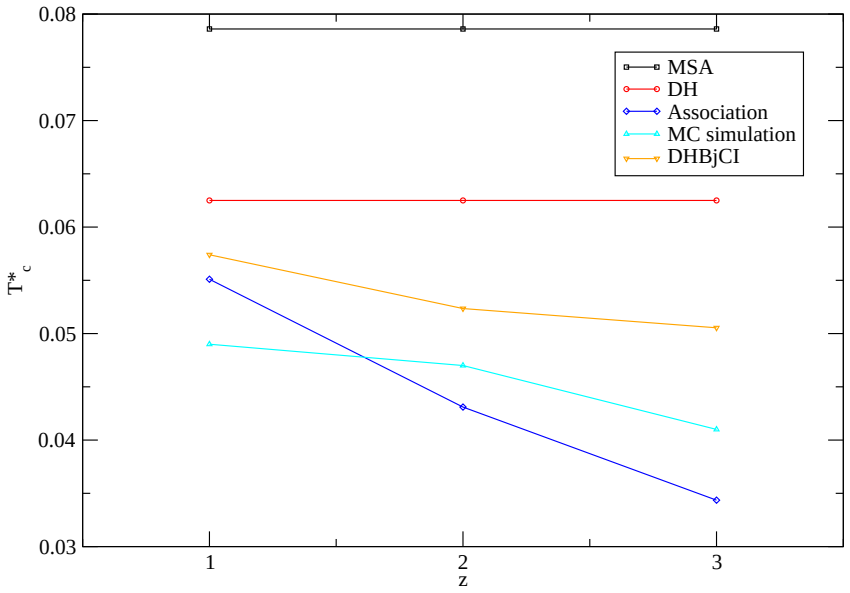

Figure 5.15: The critical temperature prediction for a $z:1$ system obtained from various theories.

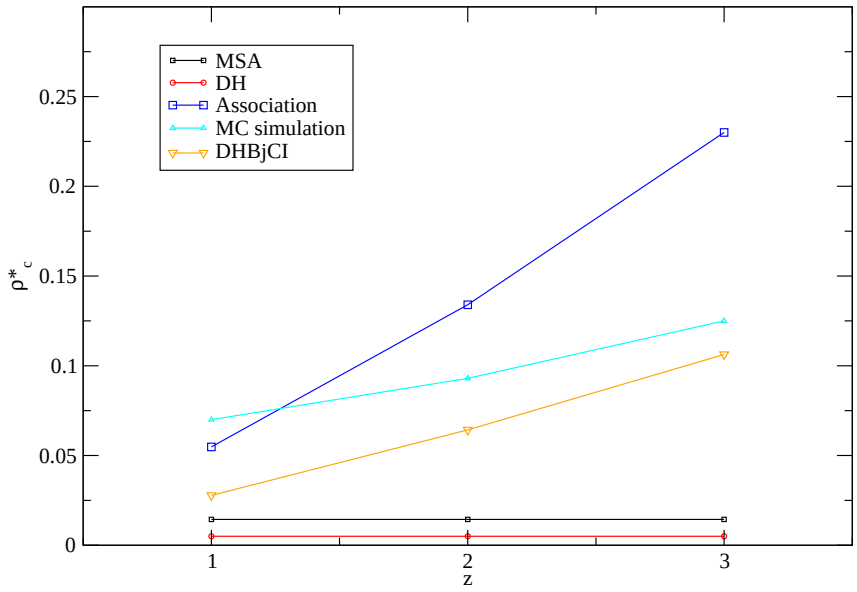

Figure 5.16: The critical density prediction for a $z:1$ system obtained from various theories.

Size-asymmetric Primitive Model

The size-asymmetric primitive model is a difficult problem for theoretical studies. In a typical size-asymmetric primitive model, one assumes all the particles carry a charge of either $+e$ or $-e$. One important parameter in such systems is the diameter ratio λ, which is normally defined as

$$\lambda = \frac{\sigma_+}{\sigma_-} \tag{5.3.15}$$

In such a binary system, swapping the signs of the particles does not change the property of the system, therefore $\lambda \geq 1$ is normally assumed. Computer simulations have suggested that as λ increases, T_c^* goes down and the phase separation happens at a lower T^* [20, 31]. However, classical theories such as MSA suggests otherwise. The MSA predictions are shown in Fig. (5.17). Currently neither the most sophisticated theories such as DHBjCIHC (DHBjCI plus Hard Core interaction) nor other theories give a good phase predictions for the size-asymmetric primitive systems. Surprisingly, our association theory gives a good qualitative prediction of the phase diagrams of such size-asymmetric system. It successfully predicts that as λ increases, both T_c^* and ρ_c^* decrease.. In addition, the binodal curves get narrower in the critical region which is consistent with the Monte-Carlo simulation results.

Regarding the size-asymmetric primitive model, our association theory seems better than

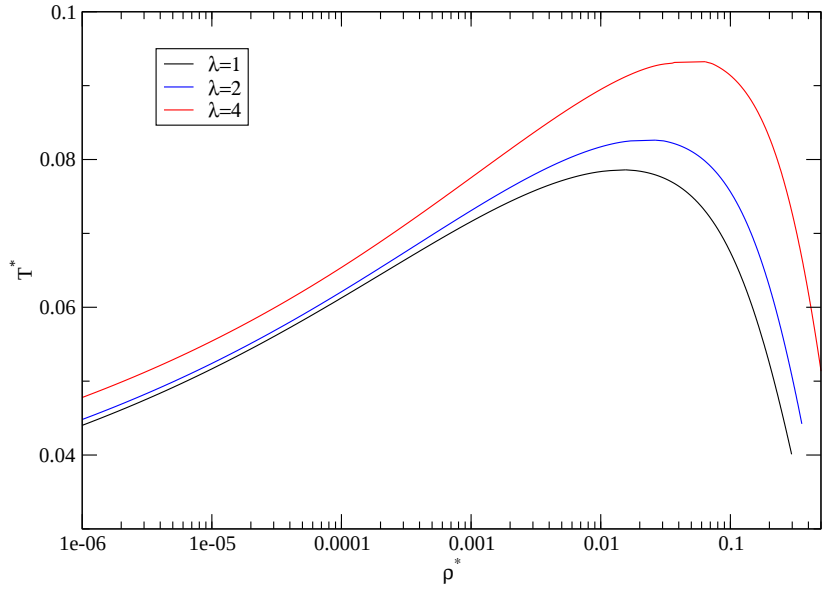

Figure 5.17: Binodal curves given by MSA for size-asymmetric systems.

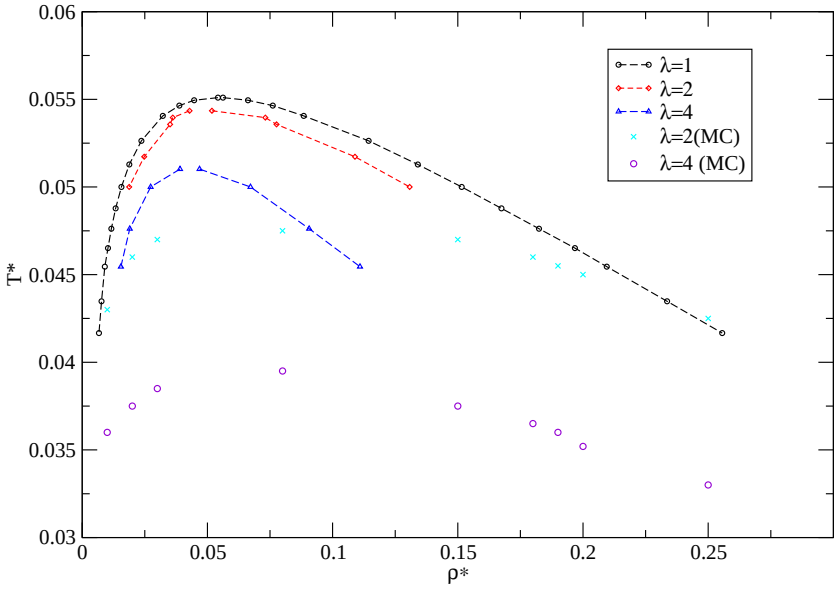

Figure 5.18: Binodal curves given by 4-site association theory for size-asymmetric systems, MC results are from Panagiotopolous[31].

other theories (4-sites association is used). It is the only theory which predicts the decrease of critical temperature when the size asymmetry gets bigger.

5.4 Further discussion

The calculation of the reference system in our association theory indicates that it is the attractive part of the electrostatic interaction that makes there is no HNC solution at low temperature. This is reasonable since we can find solutions for system at extremely low temperatures (i.e. large Γ_{OCP}) for the OCP model where effectively the attractive electrostatic interaction is zero.

In this new theory, we borrow the concept of association from the classical association theory [1, 2, 10]. Our results show that this approximate theory works reasonably well for the restricted primitive model. This theory is also in reasonably good agreement with Monte Carlo simulation results for primitive models. It gives semi-quantitatively correct predictions for the phase separation. However, the short-range part of the Coulombic interaction is different from the traditional association interactions. In this case, the number of "association sites" should not be a fixed value for the restricted primitive model. Instead, it may be expected to be the number of unlike particles within some characteristic length, which can be written as

$$n = \int_0^{l(\rho;l_B)} \rho g_{+-}^{ref}(r)\,\mathrm{d}\mathbf{r} \tag{5.4.1}$$

where $l(\rho; l_B)$ is the characteristic length as a function of the density and of Bjerrum length of the system. This concept is analogous to Bjerrum's association theory [37]. In Bjerrum's theory, he chose the characteristic length to be half of the Bjerrum length which is fairly arbitrary. Therefore our issue is how do we define this characteristic length. One numerical approach is that we may determine the distance l by which erfc(κl) is close enough to 0. Another consideration is that Eq. (5.4.1) would definitely lead us to a real number n, instead of an integer. This goes against the assumption in the classical association theory.

The other issue is the renormalisation of the association interaction. In the results shown above, we have made our own assumptions. Though the result is reasonably good, our assumption seems to be semi-empirical. In order to get better description of the system properties, a

better description of the association interaction will certainly help.

The main disadvantage of applying this association theory is the computational work involved. This theory is based on an HNC calculation so that it can only be solved numerically. Since we do not have an explicit analytical expression for the value of κ_0 with given conditions, we need to search for a new κ_0 whenever the condition is changed. The computational work is quite time-consuming compared to other analytical theories. With each trial value of κ, we will carry out a root search for the reference system first and then calculate the association energy. Apart from this, the accuracy of the results depend on the step length we use in search of κ_0. Large step lengths brings low accuracy but cost less time.

However, it may be possible to use our association theory in combination with other classical theories such as the MSA. This may produce a totally analytical theory. This work is ongoing. In the author's opinion, this association theory is very promising in treating the electrostatic systems and should have a bright future.

5.5 Conclusion

In this section, we proposed a new approximate theory to cope with Coulombic systems. The new theory borrows the concept of association from the classical association theory proposed by Wertheim. We treat the Coulombic system as a reference fluid plus short-range associations between the unlike pairs. The properties of the reference fluid are calculated by the hypernetted chain route. We have varied the number of association sites and association potential to see how they affect the results. Finally, we have shown the binodal curves given by our association theory and compared them with the Monte-Carlo simulation results. For the restricted primitive model, we have found the results better than the classical theories and as good as some of the most sophisticated theories. For the charge-asymmetric primitive model, our results are reasonably good as compared with Monte Carlo results. For the size-asymmetric primitive model, our results are also semi-quantitatively correct, better than most other theories. Our theory gives the correct prediction that as the size ratio increases, the critical temperature decreases. Association theory has a simple physical underpining and we hope it may be used, in the future, as a basis for the study of polyelectrolyte systems.

5.6 References

[1] M.S. Wertheim. “Fluids with Highly Directional Attractive Forces. III. Multiple Attraction Sites”. In: *Journal of Statistical Physics* 34 (1986), pp. 459–476. See pp. 71, 74, 75, 77, 97.

[2] M.S. Wertheim. “Fluids with Highly Directional Attractive Forces. IV. Equilibrium Polymerization”. In: *Journal of Statistical Physics* 42 (1986), pp. 477–492. See pp. 71, 74, 75, 77, 97.

[3] J.P. Hansen and I.R. McDonald. *Theory of Simple Liquids*. Academic Press, 1976. See pp. 71, 72, 74, 84.

[4] D. Forciniti and C.K. Hall. “Structural properties of mixtures of highly asymmetrical electrolytes and uncharged particles using the hypernetted chain approximation”. In: *Journal of Chemical Physics* 100 (1994), pp. 7553–7566. See p. 72.

[5] V. Schwarz et al. “Hypernetted Chain Calculations for Two-Component Plasmas”. In: *Contrib. Plasma Phys.* 47 (2007), pp. 324–330. See p. 72.

[6] K.C. Ng. “Hypernetted chain solutions for the classical one-component plasma up to Γ=7000”. In: *The Journal of Chemical Physics* 61 (1974), pp. 2680–2689. See pp. 72, 74.

[7] E. Lomba and J.L. Lòpez-Martin. “On the Solutions of the Hypernetted Chain Equation Inside the Gas-Liquid Coexistence Region”. In: *Journal of Statistical Physics* 80 (1995), pp. 825–839. See pp. 72, 75.

[8] J.F. Springer, M.A. Pokrant, and F.A. Stevens. “Integral equation solutions for the classical electron gas”. In: *Journal of Chemical Physics* 58 (1973), pp. 4863–4867. See p. 73.

[9] W.H. Press et al. *Numerical recipes: The art of scientific computing*. Cambridge University Press, 2007. See p. 74.

[10] W.G. Chapman, G. Jackson, and K. Gubbins. “Phase equilibria of associating fluids Chain molecules with multiple bonding sites”. In: *Molecular Physics* 65 (1988), p. 1057. See pp. 74, 75, 97.

[11] W.G. Chapman et al. “SAFT: Equation-of-State Solution Model for Associating Fluids”. In: *Fluid Phase Equilibria* 52 (1989), pp. 31–38. See pp. 74, 75.

[12] M.P. Allen and D.J. Tildesley. *Computer Simulation of Liquids*. Clarendon Press, Oxford, 2002. See p. 77.

[13] S.W. de Leeuw, J.W. Perram, and E.R. Smith. “Simulation of Electrostatic Systems in Periodic Boundary Conditions. I. Lattice Sums and Dielectric Constants”. In: *Proceedings of the Royal Society of London, Series A, Mathematical and Physical Sciences* 373 (1980), pp. 27–56. See p. 77.

[14] S.W. de Leeuw, J.W. Perram, and E.R. Smith. “Simulation of Electrostatic Systems in Periodic Boundary Conditions. II. Equivalence of Boundary Conditions”. In: *Proceedings of the Royal Society of London, Series A, Mathematical and Physical Sciences* 373 (1980), pp. 57–66. See p. 77.

[15] L. Lue and D. Blankschtein. “Proper integral equations for interaction-site fluids: Exact free-energy expressions”. In: *Journal of Chemical Physics* 100 (1994), pp. 3002–3012. See p. 78.

[16] T. Morita and K. Hiroike. “A New Approach to the Theory of Classical Fluids. I”. In: *Progress of Theoretical Physics* 23 (1960), pp. 1003–1027. See p. 78.

[17] K. Hiroike. “A New Approach to the Theory of Classical Fluids. II Multicomponent Systems”. In: *Progress of Theoretical Physics* 24 (1960), pp. 317–330. See p. 78.

[18] C.G. Gray and K.E. Gubbins. *Theory of Molecular Fluids Fundamentals*. Oxfod University Press, 1984. See p. 79.

[19] Y. Levin. “Electrostatic correlations: from plasma to biology”. In: *Reports on Progress in Physics* 65 (2002), pp. 1577–1632. See pp. 80, 91.

[20] J. J. Weis and D. Levesque. “Thermodynamic and structural properties of size-asymmetric charged hard spheres”. In: *Chemical Physics Letters* 336 (2001), pp. 523–528. See pp. 82, 87, 95.

[21] J. Sýs, S. Labík, and A. Malijevský. “Parameterization of the radial distribution function and thermodynamic properties of the restricted primitive model of electrolyte solutions”. In: *Czech. J. Phys. B* 33 (1983), pp. 763–771. See p. 82.

[22] G. Orkoulas and A.Z. Panatiotopoulos. “Free energy and phase equilibria for the restricted primitive model of ionic fluids from Monte Carlo simulations”. In: *Journal of Chemical Physics* 101 (1994), pp. 1452–1459. See pp. 85, 87, 88.

[23] A. Karatrantos. PhD thesis. University of Manchester, 2010. See pp. 84, 85.

[24] A.Z. Panagiotopoulos. “Simulations of phase transition in ionic systems”. In: *Journal of Physics: Condensed Matter* 17 (2005), pp. 3205–3212. See pp. 87, 88.

[25] L. Blum. “Mean spherical model for asymmetric electrolytes. I. Method of solution”. In: *Molecular Physics* 30 (1975), pp. 1529–1535. See p. 87.

[26] L. Blum and J.S. Hoye. “Mean spherical model for asymmetric electrolytes. 2. Thermodynamic properties and the pair correlation function”. In: *The Journal of Physical Chemistry* 81 (1977), pp. 1311–1316. See p. 87.

[27] O. Bernard and L Blum. “Binding mean sperical approximation for pairing ions: An exponential approximation and thermodynamics”. In: *The Journal of Chemical Physics* 104 (1996), pp. 4746–4754. See p. 87.

[28] Y.V. Kalyuzhnyi. “Thermodynamics of the polymer mean-spherical ideal chain approximation for a fluid of linear chain molecules”. In: *Molecular Physics* 94 (1998), pp. 735–742. See p. 88.

[29] M.E. Fisher and Y. Levin. “Criticality in ionic fluids: Debye-Hückel theory, Bjerrum, and beyond”. In: *Physical Review Letters* 71 (1993), pp. 3826–3829. See pp. 88, 93.

[30] G. Orkoulas and A.Z. Panagiotopoulos. “Phase behavior of the restricted primitive model and square-well fluids from Monte Carlo simulations in the grand canonical ensemble”. In: *Journal of Chemical Physics* 110 (1999). See p. 88.

[31] J.M. Romero-Enrique et al. “Coexistence and criticality in size-asymmetric hard-core electrolytes”. In: *Physical Review Letters* 85 (2000), pp. 4558–4561. See pp. 91, 95, 96.

[32] A.Z. Panagiotopoulos and M.E. Fisher. “Phase Transitions in 2:1 and 3:1 Hard-Core Model Electrolytes”. In: *Physical Review Letters* 88 (2002), p. 045701. See p. 91.

[33] J. Aqua, S. Banerjee, and M.E. Fisher. “Criticality in charge-asymmetric hard-sphere ionic fluids”. In: *Phys. Rev. E.* 72 (2005), p. 041501. See pp. 91–93.

[34] E. Luijten, M.E. Fisher, and A.Z. Panagiotopoulos. “Universality Class of Criticality in the Restricted Primitive Model Electrolyte”. In: *Physical Review Letters* 88 (2002), p. 185701. See p. 91.

[35] Y.C. Kim, M.E. Fisher, and A.Z. Panagiotopoulos. “Universality of Ionic Criticality: Size- and Charge-Asymmetric Electrolytes”. In: *Physical Review Letters* 95 (2005), p. 195703. See p. 91.

[36] Y. Levin and M.E. Fisher. “Criticality in the hard-sphere ionic fluid”. In: *Physica A* 225 (1996), pp. 164–220. See p. 91.

[37] A. Travesset and D. Vaknin. “Bjerrum pairing correlation at charged interfaces”. In: *Europhyiscs Letters* 74 (2006), pp. 181–187. See p. 97.

CHAPTER

SIX

DISSIPATIVE PARTICLE DYNAMICS STUDY OF NEUTRAL POLYMERS

6.1 Introduction

Dissipative Particle Dynamics (DPD) is a simulation technique which links atomistic level and large network simulations [1]. DPD has been established as a robust way to investigate mesoscopic behaviour, such as micellization. Warren [1], Glotzer [2], den Otter [3] and many other researchers have applied DPD simulations to various systems such as surfactants and tethered polymers [4–6]. One important advantage of DPD is that it includes the hydrodynamic interactions which should be considered on the length-scale larger than the atomistic level. In this chapter we are going to use DPD to investigate different systems with semi-flexible polymers of specific shapes. Firstly, we are going to use DPD to study rod-like molecules and rod/sphere mixtures and discuss what liquid crystal phases they might form. Secondly, we use DPD to simulate some di-block and tri-block co-polymers, in order to find a possible route for spider silk fibroin formation. Many previous simulation studies of liquid crystal use MC simulations with hard particles [7]. One disadvantage of studying hard bodies using MC is that at high densities, the system is likely to jam in certain configurations. However, since the DPD potential is softly repulsive, the system is more mobile and equilibrates more easily. Besides, it is of fundamental interest to see how these soft-body behave at high density. The second topic on spider silk is developed from an industrial project. Kaplan et. al. [8] have studied the formulation of spider fibroin based on experimental observations and have proposed a possible route towards fibroin formation. We use DPD simulation to help check the viability of this proposal.

6.2 Theoretical Background

Newton's equations of motion for a particle i, are

$$\frac{\mathrm{d}\mathbf{r}_i}{\mathrm{d}t} = \mathbf{v}_i \tag{6.2.1}$$

$$m_i \frac{\mathrm{d}\mathbf{v}_i}{\mathrm{d}t} = \mathbf{f}_i \tag{6.2.2}$$

where $\mathbf{r}_i$ is the position of particle i, $\mathbf{v}_i$ is the velocity, m_i is the mass and $\mathbf{f}_i$ is the force on particle i. For simplicity, the masses of the particles in DPD are all assumed to be 1. Therefore, we rewrite Eq. (6.2.2) as

$$\frac{\mathrm{d}\mathbf{v}_i}{\mathrm{d}t} = \mathbf{f}_i \tag{6.2.3}$$

which means that the force acting on each particle equals its acceleration. On each particle, the total force is the sum of three parts: conservative force, dissipative force and random force.

$$\mathbf{f}_i = \sum_{j \neq i} \left(\mathbf{F}_{ij}^C + \mathbf{F}_{ij}^D + \mathbf{F}_{ij}^R \right) \tag{6.2.4}$$

The total force sums over all other particles within a specific cutoff distance r_c. Since r_c is the only length scale in DPD, it is set as the unit length for simplicity.

The conservative force is a soft repulsive force along the line of the particle centres which is given as

$$\mathbf{F}_{ij}^C = \begin{cases} a_{ij}(1 - r_{ij})\hat{\mathbf{r}}_{ij}, & (r_{ij} < 1) \\ 0, & (r_{ij} \geq 1) \end{cases} \tag{6.2.5}$$

where a_{ij} is the maximum repulsion between particles, analogous to the Hookean constant. $r_{ij} = |\mathbf{r}_{ij}|$ is the distance between the centres of particle i and j, and $\hat{\mathbf{r}}_{ij} = \mathbf{r}_{ij}/r_{ij}$ is the direction of the force.

The dissipative force and the random force are given as

$$\mathbf{F}_{ij}^{D} = -\gamma\omega^{D}(r_{ij})(\hat{\mathbf{r}}_{ij}\cdot\mathbf{v}_{ij})\hat{\mathbf{r}}_{ij} \tag{6.2.6}$$

$$\mathbf{F}_{ij}^{R} = \epsilon\omega^{R}(r_{ij})\theta_{ij}\hat{\mathbf{r}}_{ij} \tag{6.2.7}$$

where ω^D and ω^R are r-dependent weight functions. $\mathbf{v}_{ij} = \mathbf{v}_i - \mathbf{v}_j$ and $\theta_{ij}(t)$ a random fluctuation with Gaussian statistics. These also act along the line of the particle centres.

Warren et. al. [9] have shown that one of the two weight functions are related. Thus

$$\omega^{D}(r) = \left[\omega^{R}(r)\right]^{2} \tag{6.2.8}$$

$$\epsilon^{2} = 2\gamma k_B T \tag{6.2.9}$$

A detailed derivation of these relations can be found in Ref.[9]. Following Groot and Warren [1], we work in the units such that $k_BT = 1$. This effectively specifies a unit of time and all the conservative energies are automatically in units of k_BT.

Simple choices for $\omega^D(r)$ and $\omega^R(r)$ are

$$\omega^{D}(r) = \left[\omega^{R}(r)\right]^{2} = \begin{cases} (1-r)^2, & (r<1) \\ 0, & (r\geq 1) \end{cases} \tag{6.2.10}$$

Here we follow Español and Warren [10] where no normalisation factors are included in these functions. The numerical calculation here uses a velocity-Verlet algorithm where the details can be found in [1].

In this study, we also apply some extra interactions between the bonded particles. As in a polymer, the bond between a pair of neighbouring particles (monomers) is modelled as a spring potential where

$$u_{spring}(r) = \frac{1}{2}k_{spring}(r-r_e)^2 \tag{6.2.11}$$

where k_{spring} is the spring constant and r_e is the average equilibrium distance between the two bonded neighbours.

In order to add stiffness to the polymeric chain, a bending potential is also introduced. The

bending potential is given by

$$u_{bending}(\phi) = k_{bend}(1 - \cos(\phi - \phi_0)) \tag{6.2.12}$$

where the angle ϕ is defined by the two bonds connecting the three consecutive particles, k_{bend} is the bending constant and ϕ_0 is the preferred angle.

6.3 Simulation of Pure Rod Systems

DPD is a useful simulation technique because it can be mapped to various systems by adjusting the interaction parameters [1]. Meanwhile, it can also cope with some ideal models for theoretical studies. We start with a simple semi-flexible rod system where each rod is made up of a fixed number of DPD particles. The simulation is done in an NVT ensemble, where we fix the total number of DPD particles (N), the volume of the bulk system (V) and the temperature (T). In order to check the size-dependence of our observation, we also carry out our simulations at various box-sizes. By changing the density of the system, we are able to observe some phase transition behaviour. Various simulations (see, e.g., a review from Allen [11]) have shown phase transitions for hard rod systems. Normally, spherocylinders(i.e. a cylinder of length L and diameter D, with hemispherical caps of diameter D at both ends) are used to simulate the rod-like molecules in the Monte Carlo simulation. Allen has found that for a spherocylinder system with an aspect ratio $L/D = 5$, the nematic phase is stable relative to the isotropic liquid at about $\rho^* \approx 0.45$ and a smectic phase form in the regions $0.6 < \rho^* < 0.75$. ($\rho^* = \rho/\rho_{cp}$ where ρ_{cp} is the close-packing density for the spherocylinders.) To sum up, as the density increases, hard rod system undergoes an isotropic-nematic-smectic phase transition.

Since the DPD particles have a softly repulsive potential, the phase transitions are different from the hard body system, as we discuss below.

6.3.1 Short Rod Systems

The short rods are made up of 8 DPD particles, where the interaction parameters are set as: $a_{ij} = 25, \gamma = 4.5$. The bonding parameters are $k_{spring} = 128, r_e = 0.5$ and the bending potential is set as: $k_{bend} = 128, \phi_0 = 0$. The chain length in this case is approximately 4.5

(note that the diameter of the DPD particle is set to be 1). The cubic box length is set to be $L_x = L_y = L_z = 15$, which is more than 3 times that of the chain length. The temperature is set as $T = 1$. The time step is $\Delta t = 0.01$ and the total simulation time is $t = 3000$ DPD units. To vary the system density, we start our simulation from a DPD density of $\rho = 0.5$ which means on average in each unit volume there are 0.5 DPD particles. We increase this density in steps of $\Delta\rho = 0.5$, till it reaches $\rho = 5.0$. All rods are randomly placed in the initial configuration. The different colours of the rods in the figures are for the purpose of differentiating different chains. The reason is that at high densities, it is very hard to identify different rods using a single colour.

Fig. (6.1) is the snapshot of a DPD rod system at a density of $\rho = 1.5$. At this density and at densities lower than this, an isotropic phase is found. The rods are lying in random directions and there are a lot of overlaps. Due to the overlaps, we rescale the thickness of the rods in the snapshots, in order to get a better view (the thickness of the rods are adjusted to $r = 0.15$. This applies to all the following snapshots as well).

As the density increases, the rods tend to align in an ordered way. For the system with a density $\rho = 2.5$, the rods tend to form a partially orientationally ordered phase in the cubic box, (Fig.(6.2)). At this density (pressure), a number of chains are still bent due to their semi-flexibility.

If we push the density up further, a full nematic phase can be observed. As shown in Fig. (6.3), at this higher density, the rods are relatively straight and all the rods tend to align in a uniform direction. The relatively high pressure restrains the translational movement of the semiflexible chains.

Up to this point, the phase behaviour follows an isotropic - nematic route. The short rods inside the system become better ordered as the density increases. This is consistent with the hard rod or hard cylinder systems [12]. However, as the density goes further up, we may see the ordered configuration start to collapse, as shown in Fig. (6.4) and Fig. (6.5). The rods at the bottom-right corner of the Fig. (6.4) are lying almost perpendicular to the the rest of the rods. As the density reaches $\rho = 5.0$ the system becomes isotropic again. This behaviour is different from the hard system. Since hard objects cannot overlap, there is a maximum value for the packing fraction. The liquid crystal phase transition for hard objects is purely entropy-driven. In our case, the DPD density can take any arbitrary value which means we may put as many

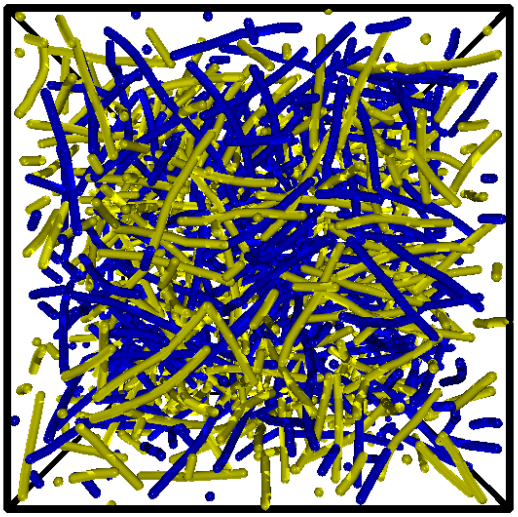

Figure 6.1: A snapshot of a short rod system with its density $\rho = 1.5$ at $t = 3000$.

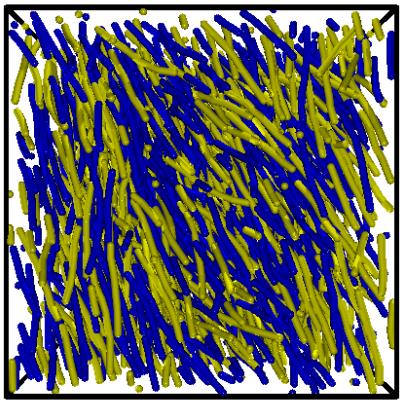

Figure 6.2: A snapshot of a short rod system with its density $\rho = 2.5$ at $t = 5000$.

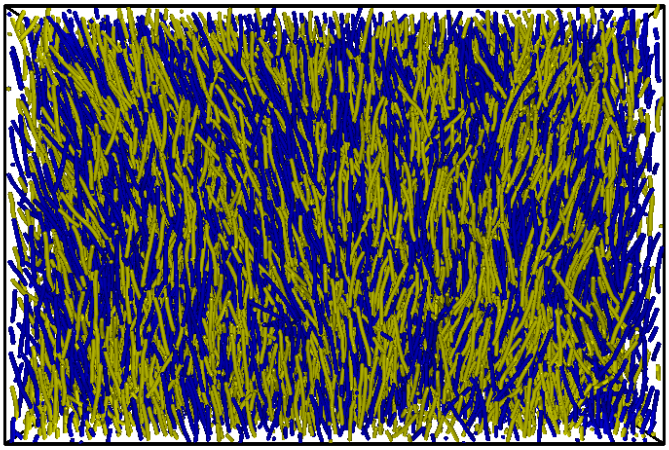

Figure 6.3: A snapshot of a short rod system with its density $\rho = 3.0$ at $t = 5000$.

particles as we want in the box. As the density goes up, more and more DPD particles have to overlap, which brings in extra repulsive interactions to balance the entropy loss. Moreover, due to the large number of pairwise repulsive interaction, the free energy contribution from the entropy will be insignificant compared with the enthalpic contribution. Therefore the rods have no preference to align in an ordered way or in an isotropic way. In order to prove this, we also start our simulation where all the rods are initially aligned parallel. After 5000 DPD time units, the snapshots show it also goes to an isotropic phase.

Our step size $\Delta\rho = 0.5$ might be too big to find the smectic phase. The smectic phase may appear between $\rho = 3.0$ and $\rho = 4.0$. Therefore for short soft DPD rods, the change of liquid crystal phases are isotropic - nematic (-possibly smectic) - nematic -isotropic as the DPD density increases. The missing of the smectic phase might also be a result of the low 'aspect ratio'.

The order parameter S is often used to describe the orientational order of a liquid crystal. It is usually defined as the average of the second Legendre polynomial by

$$S = \langle P_2(\cos\theta)\rangle = \left\langle \frac{3\cos^2\theta - 1}{2} \right\rangle \tag{6.3.1}$$

where θ is the angle between the direction of the rod and the director of the system. Since the chains are semi-flexible, we are unable to give a direction which is defined as in the hard

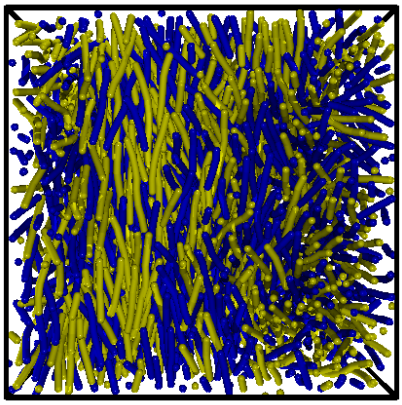

Figure 6.4: A snapshot of a short rod system with its density $\rho = 4.0$ at $t = 5000$.

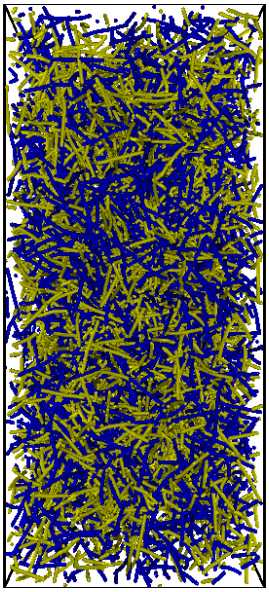

Figure 6.5: A snapshot of a short rod system with its density $\rho = 5.0$ at $t = 5000$.

object system. Instead, we use ($\mathbf{r_{head}} - \mathbf{r_{tail}}$) to approximate the orientation of the rods. This approximation is quite rough since most chains are slightly bent but we can still use this to get some structual information (order parameter is shown in Fig.(6.6)).

6.3.2 Long Rod Systems

In order to get a better idea how soft repulsive DPD rods form liquid crystal phases, we increase the number of DPD particles inside each rod. For a 'long rod' system, each rod is made up of 16 DPD particles, which leads to the aspect ratio of $l/\sigma \approx 8.0$. We no longer use the cubic box in the simulation but instead we choose two boxes with different lengths but the same volume in order to investigate the box size effects. The size of the two boxes are respectively $15 \times 30 \times 60$ and $20 \times 30 \times 45$. The other parameters remain the same as we used for the short rod systems.

At low densities, the system still forms an isotropic phase. Since the rods get longer, we expect the nematic phase to appear at a lower density than the case for short rod systems. As shown in Fig. (6.7), a good nematic phase has formed when the density reaches 1.5.

However, as the density increases, we approach an interesting phase. As shown in Fig. (6.8), in a short range, the long rods form layers as may be seen in a smectic phase. However, over long ranges, the chains are not facing in the same direction. As we can see, those blocks formed by the packed chain molecules are aligning either parallel or perpendicular to others. Inside the layers, the rods are oriented along the layer normal which is the same as the smectic A phase.

We stop at density $\rho = 3.0$ because when the density is pushed higher, the simulation time to reach the equilibrium is significantly longer, due to the fact that we need a big simulation box for the long rod systems. In addition, like the short rod system, the long rod system finally goes back to isotropic phase if the density goes very high.

6.3.3 Equilibration Time and Size Effects

The time required for equilibrating the system can be approximated in the following way. According to Einstein's law of diffusion, the definition of the diffusion constant D in the solu-

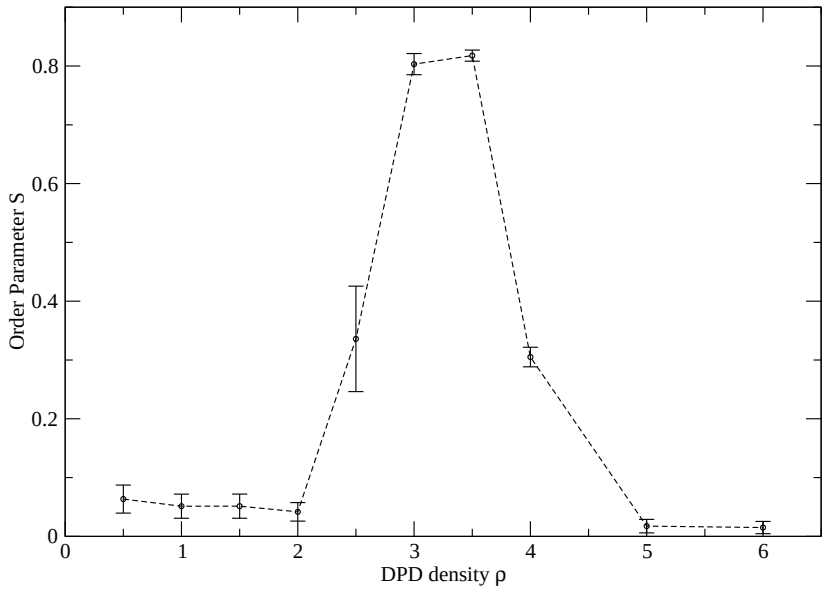

Figure 6.6: Order parameters of the short rod system with various DPD densities

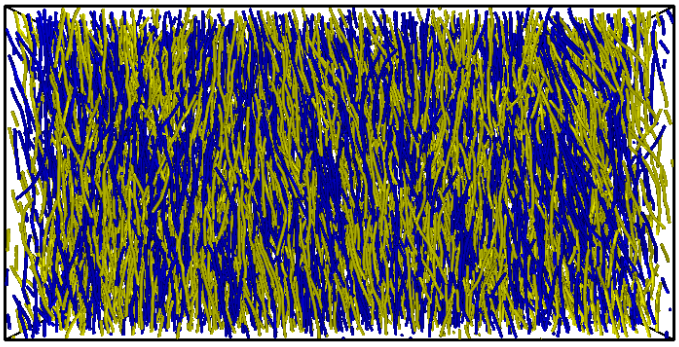

Figure 6.7: A snapshot of a long rod system with its density $\rho = 1.5$ at $t = 5000$.

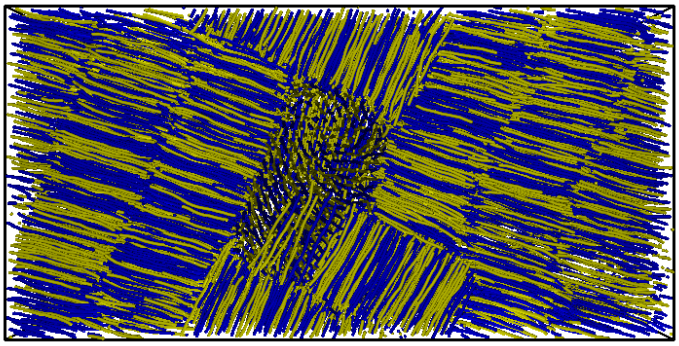

Figure 6.8: A snapshot of a long rod system with its density $\rho = 2.5$ at $t = 5000$.

tion can be written as:

$$D = \frac{< \Delta r^2 >}{6t} \tag{6.3.2}$$

where Δr is the displacement of a particle, t is the time for diffusion, $< \cdots >$ denotes the statistical average. It is sufficiently long for a particle to diffuse over the shortest box dimension. Therefore we may set the Δr as the shortest dimension (e.g. 15 in the $15 \times 15 \times 15$ and $15 \times 30 \times 60$ cases). In this case, the time needed for equilibration should be on order of

$$t = \frac{15^2}{6D} \tag{6.3.3}$$

The diffusion constant D can be estimated from the simulation, using Eq.(6.3.2) and the results are shown in Fig. (6.9) and Fig. (6.10).

For short rods, as the system density goes high (e.g. $\rho = 5.0$), the minimum diffusion constant is about $D \approx 0.02$. This value corresponds to an equilibrated time of $t \approx 2000$. We may consider the system equilibrated as long as the simulation time is on the same order. For $\rho = 5.0$ a simulation time of $t = 5000$ seems a reasonable choice. In fact the system may be equilibrated much earlier as we may see the diffusion constant reaches a relatively constant value long before this calculated time.

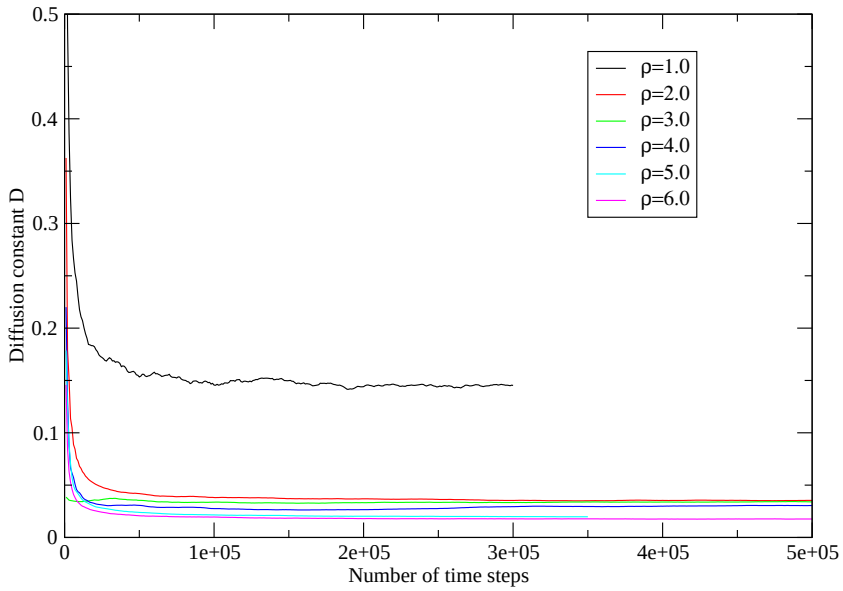

Figure 6.9: The diffusion coefficient for short rods with various densities.

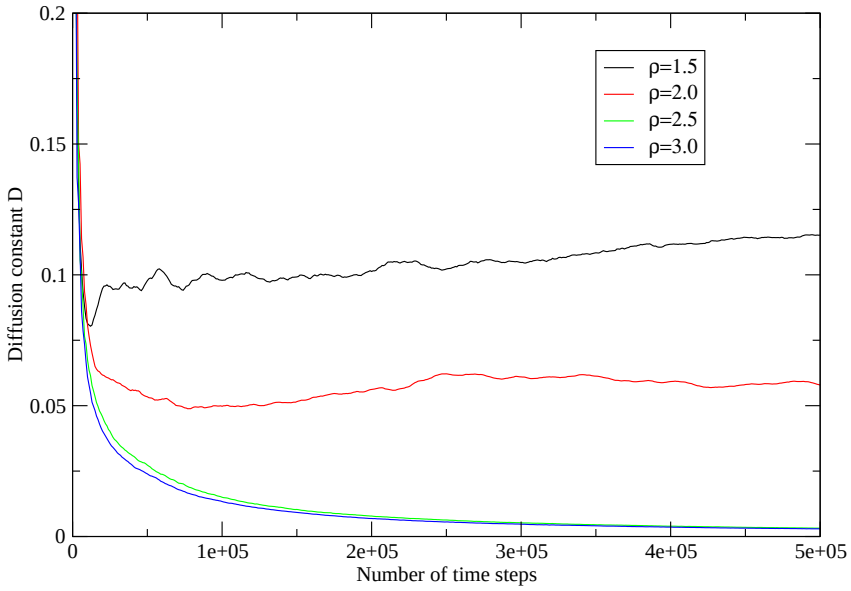

Figure 6.10: The diffusion coefficient for long rods with various densities.

For long rods, the situation is similar. However, with the layered structure, the long rods are much more difficult to move, and have a much lower diffusion constant. The calculated equilibration time is much longer. $t \approx 7000$ is obtained through calculation for a long rod system with a density of $\rho = 3.0$. However, the time variation of the order parameter S indicates system may have reached an equilibrated state long before this.

Apart from investigating the time used to equilibrating the systems, we also study the size effect of the box. We use the order parameter to see whether the box size affect the formation of the liquid crystal phases. For systems in an isotropic phase, the order parameters are slightly different for different sized boxes (Fig. (6.11)). But the values are close to zero in both cases, indicating isotropic phases.

For systems in a nematic phase, the situation is quite simple. Even with different box sizes, the order parameters are almost the same under the same DPD density (Fig. (6.12) and Fig. (6.13)). The size of the box may only affect the time to reach the equilibrium state.

When the layered structures form, the order parameters for different boxes show discrepancies (Fig. (6.14)). A possible reason is that the rods are forming blocks and layers but the orientations of the blocks and the layers are strongly affected by the box dimensions. This leads to the difference in order parameters.

In order to ensure the system is at its equilibrium state, the simulation time we use is at least on the order of $t = \frac{<\Delta r^2>}{6D}$. This criterion also applies to the other simulations in this chapter.

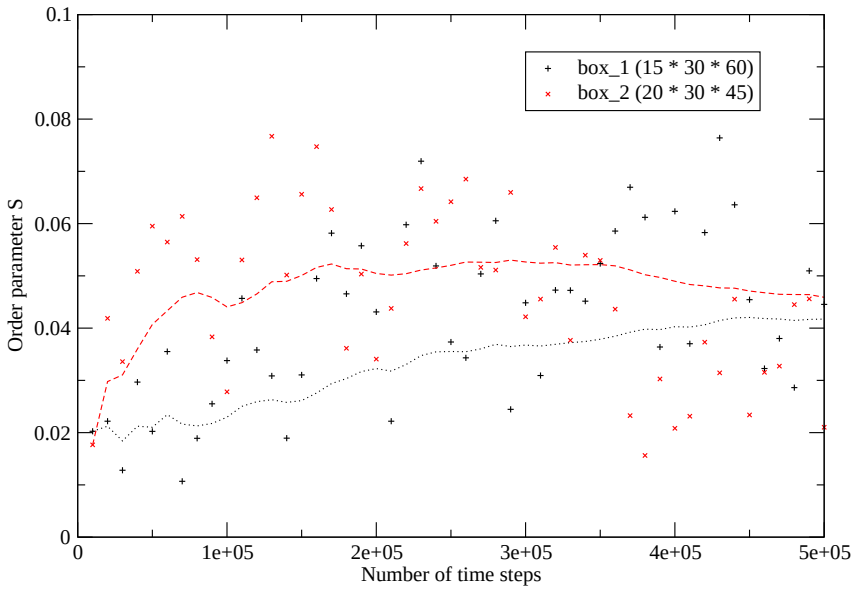

Figure 6.11: An example of order parameters of a short rod system in an isotropic phase of different box sizes, $\rho = 2.0$. The dashed and dotted lines are the average values of the corresponding order parameters.

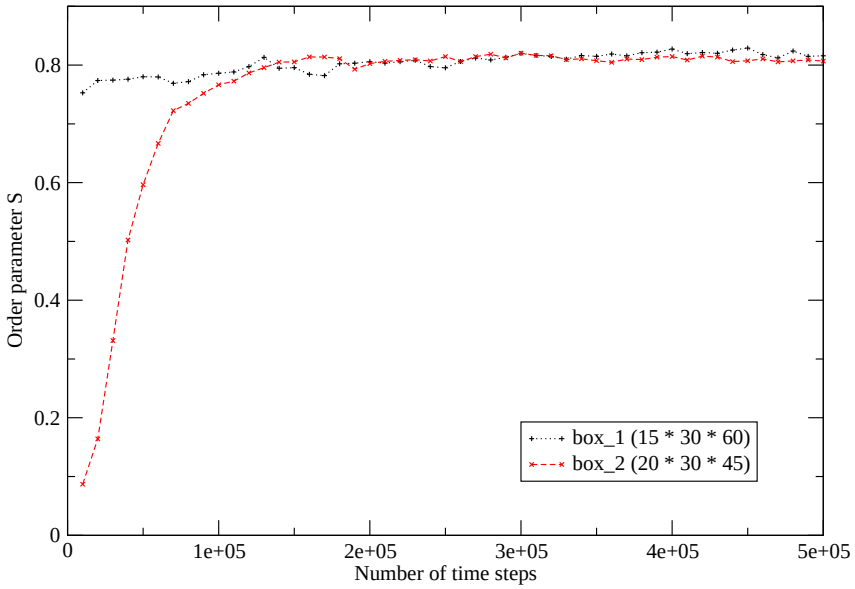

Figure 6.12: An example of order parameters of a short rod system in the nematic phase of different box sizes, $\rho = 3.0$.

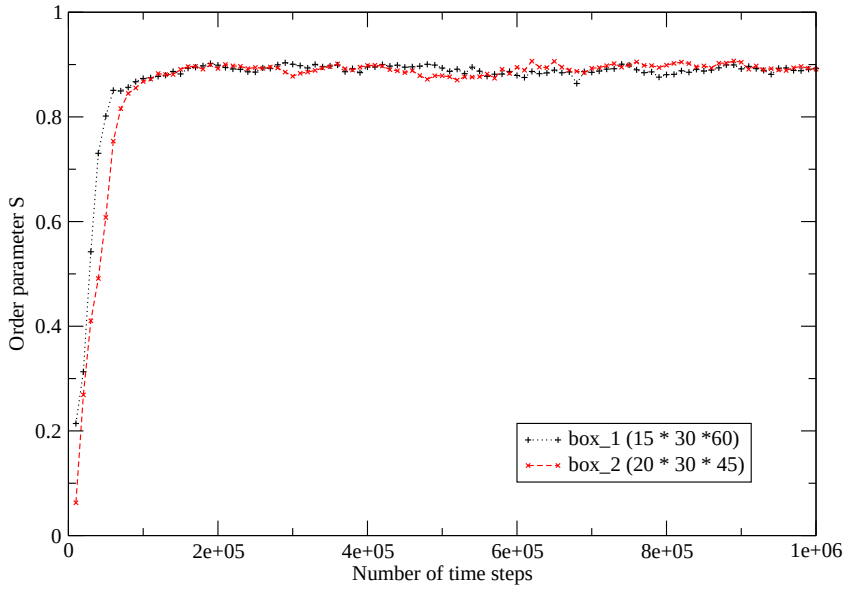

Figure 6.13: An example of order parameters of a long rod system in the nematic phase of different box sizes, $\rho = 1.5$.

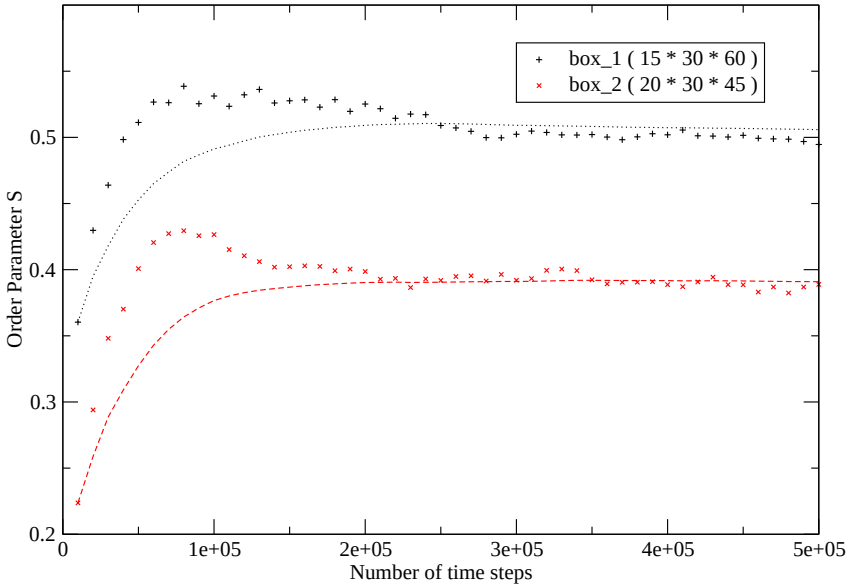

Figure 6.14: An example of order parameters of a long rod system in the layered structure of different box sizes, $\rho = 3.0$. The dotted and dashed lines are the running average of the dots with corresponding colours.

6.4 Simulation of Rod and Sphere Mixtures

As we have seen, For long rod systems, the sequence of phases is isotropic to nematic to smectic as the density goes up. When spherical particles are added in, new liquid crystal phases may form, such as a lamella phase [13]. The colloidal phase behaviour of hard rod and sphere mixtures has been studied by theory [14], simulation and experiment[15]. The addition of spherical particles to rod-like molecules disfavours the formation of nematic phase. It also causes the formation of a wide bi-phasic region, where nematic and isotropic phases coexist [13, 16]. However, at high densities, it is found that the addition of spheres helps to stabilise the lamellar phase [17]. Computationally, this rod-sphere mixture behaviour has been studied by MC and MD extensively with hard objects [16]. Since hard objects are impenetrable, the driving force for such phase transitions is purely entropic. In this section, we are trying to approach this behaviour from a different angle by applying DPD studies to a rod-sphere mixture. Both rods and sphere molecules are made up of basic DPD particles. All the basic DPD particles are identical so that there is no preferential interaction between a like particle pair and an unlike particle pair. All the interaction parameters have the same value as in the pure rods systems. The rods used in this study are the 'long' rod molecule mentioned in the previous section, containing 16 DPD particles. We use a 17-particle dendrimer to simulate the 'sphere' molecules, which is sketched in Fig. (6.15).

Within the system, the dendrimer will collapse to a sphere-like molecule due to the elastic spring interaction and the repulsive interaction between particles. A 'sphere' molecule has a diameter D where $D/r_c \approx 2.0$. They are not perfectly spherical but are able to provide some useful information for theoretical studies on rod/sphere mixture.

The simulation is performed with the long rod model described above and these dendrimer sphere molecules. Again, the blue and yellow stripes represent the rods (we use different colours to distinguish different molecules). The red spheres represent the central particles of the dendrimer molecules. The size of the particles are re-scaled in order to fit the snapshots and to give a better visualisation of the system. In the figures, n_{rod} indicates the number of rod molecules while n_{sphere} indicates the number of sphere molecules.

At low DPD densities up to $\rho = 1.0$, the rods and the spheres are fully miscible. Depending on the relative proportion of rods and spheres, the system can be treated as rod molecules fully

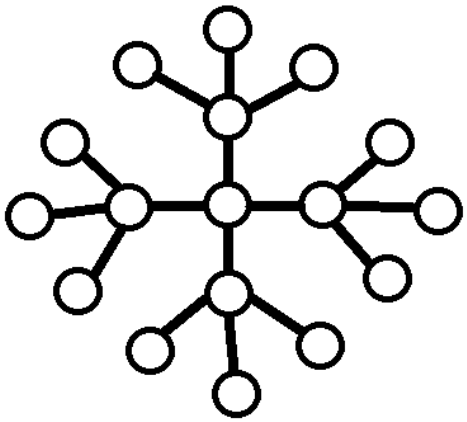

Figure 6.15: A schematic of the dendrimer-like sphere particles.

dissolved in sphere molecule (Fig. (6.16)) solvent or sphere molecules fully dissolved in rod molecule solvent(Fig. (6.17)). As a result of the low pressure (or density), some rods shown in the snapshots are quite flexible. The rods are in an isotropic phase.

As the DPD density increases, to $\rho = 1.5$, the molecules are more closely packed. In the system where there are more rod molecules, the sphere molecules are miscible in the rods as shown in Fig.(6.18). Due to the higher pressure, the rods are less bent and form a proper nematic phase. If we increase the number of sphere molecules, a phase separation can be observed as seen in Fig.(6.19). The sphere molecules tend to aggregate to form a sphere-rich phase while the rods align parallel to the sphere layer. If we increase the number of sphere molecules further, the rods dissolve in the sphere molecules. The rods are facing in random directions as shown in Fig.(6.20).

At DPD density $\rho = 2.0$, layered structures start to form as the number of sphere molecules increases. Initially, when the proportion of 'spheres' is very low, the rods are forming a nematic phase (Fig.(6.21)). As we increase the number of 'spheres', the rods start to form smectic phase. The boundaries of the layers are slightly bent as in Fig.(6.22). The 'sphere' molecules aggregate and stay between the layers. If we increase the number of sphere molecules further, we may see the lamellar phase which has been reported in the experiments (see Fig.(6.23)). A good layered structure is formed where the rods and the spheres are in a 'rod-sphere-rod-sphere' type of structure. The sphere molecules have some fluidity so they are able to move from one layer

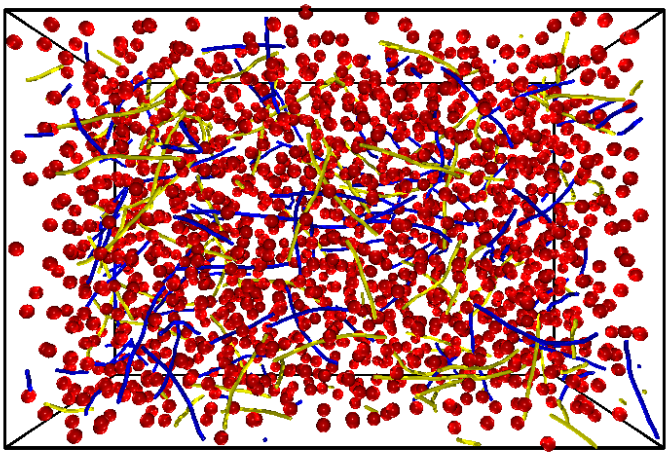

Figure 6.16: A snapshot of a medium rod/sphere system with a density $\rho = 1.0$ at $t = 9000$, $n_{rods} : n_{sphere} = 1 : 9$.

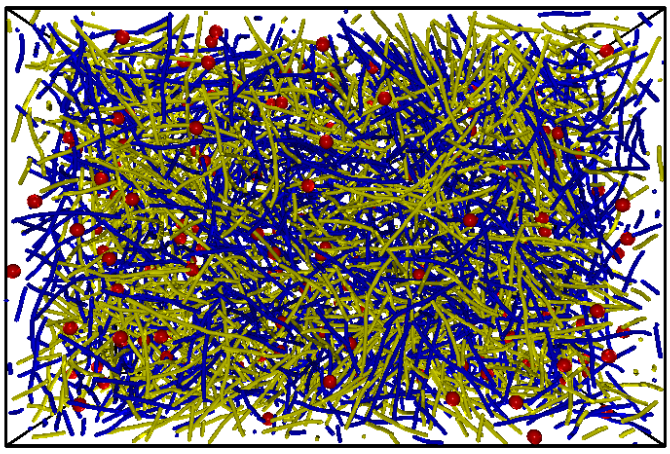

Figure 6.17: A snapshot of a medium rod/sphere system with a density $\rho = 1.0$ at $t = 9000$, $n_{rods} : n_{sphere} = 9 : 1$.

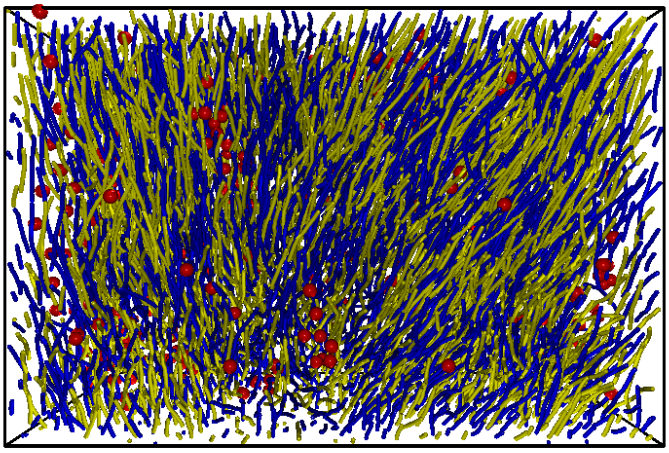

Figure 6.18: A snapshot of a medium rod/sphere system with a density $\rho = 1.5$ at $t = 9000$, $n_{rods} : n_{sphere} = 9 : 1$.

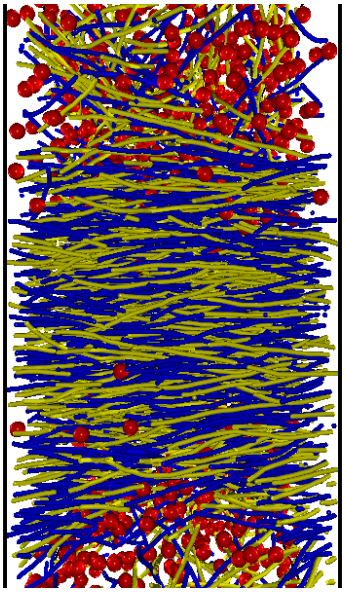

Figure 6.19: A snapshot of a medium rod/sphere system with a density $\rho = 1.5$ at $t = 9000$, $n_{rods} : n_{sphere} = 6 : 4$, a phase separation can be observed.

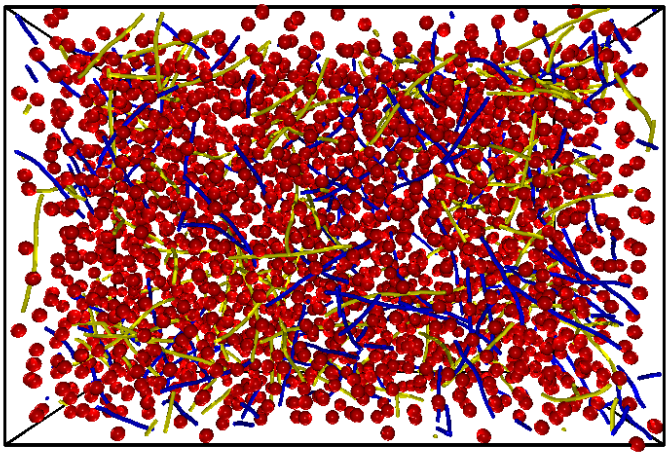

Figure 6.20: A snapshot of a medium rod/sphere system with a density $\rho = 1.5$ at $t = 9000$, $n_{rods} : n_{sphere} = 9 : 1$.

to another. In such a system where the 'sphere' molecules are dominant in number, due to the pressure of the system, the rods naturally form an ordered bundle. A phase separation can be observed where small amount of the rods are dissolved in the 'sphere' molecule solvent leaving the majority of the rods form a well-structured phase (see Fig.(6.24)).

As the DPD density further increases to $\rho = 2.5$, the phase behaviour becomes more interesting. In a system where the rods are dominant, they form similar structures to those in the pure rod system. The layers tend to be either parallel or perpendicular to each other to minimise the system energy. However, this time we no longer see the phase where the layers can point in all 3 directions but instead, only 2 direction can be seen on the snapshot through the simulation (see Fig.(6.25)). The sphere molecules are dispersed alongside the boundary of the rod layers. As we increase the proportion of the sphere molecules, the rod layers tend to align with better order to form a lamellar phase (see Fig.(6.26)). The existence of more sphere molecules in fact increases the mobility of the rod bundles. When the number of sphere molecules is low, the rod bundles sometimes are perpendicular to each other. Even when the parallel structure is preferred, their lack of mobility restrains them from rotating 90° to form such structure. However, when there are more sphere molecules, the extra mobility provided by them allows the rods to form a good lamellar phase. But as the number of the sphere molecules increases further, the rod layers becomes too mobile to form a stable lamellar phase. Therefore a defected lamellar

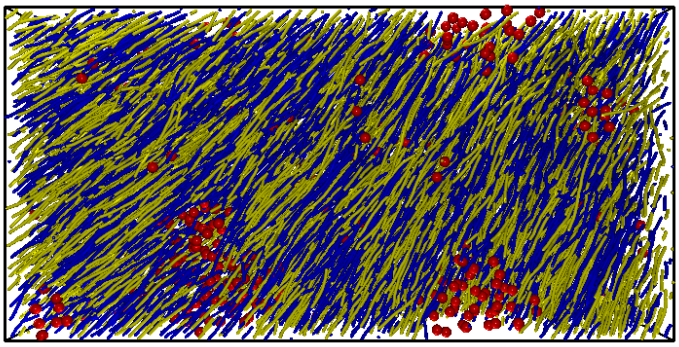

Figure 6.21: A snapshot of a medium rod/sphere system with a density $\rho = 2.0$ at $t = 9000$, $n_{rods} : n_{sphere} = 9 : 1$, a nematic phase can be observed.

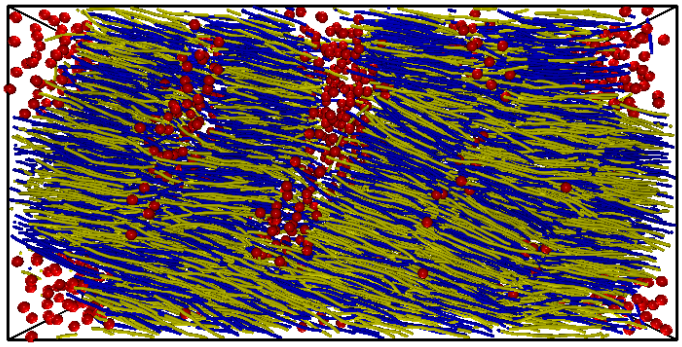

Figure 6.22: A snapshot of a medium rod/sphere system with a density $\rho = 2.0$ at $t = 9000$, $n_{rods} : n_{sphere} = 8 : 2$, the formation of a layered structure.

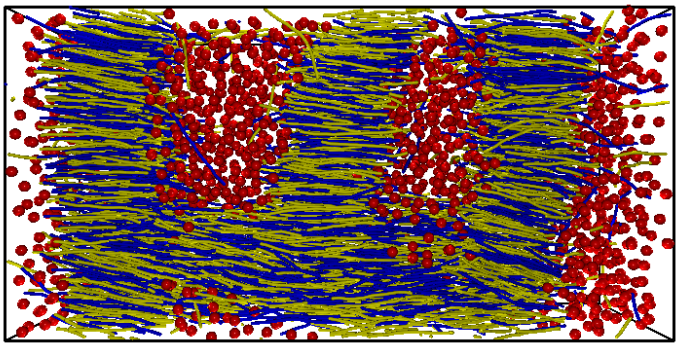

Figure 6.23: A snapshot of a medium rod/sphere system with a density $\rho = 2.0$ at $t = 9000$, $n_{rods} : n_{sphere} = 6 : 4$, a defected lamellar phase.

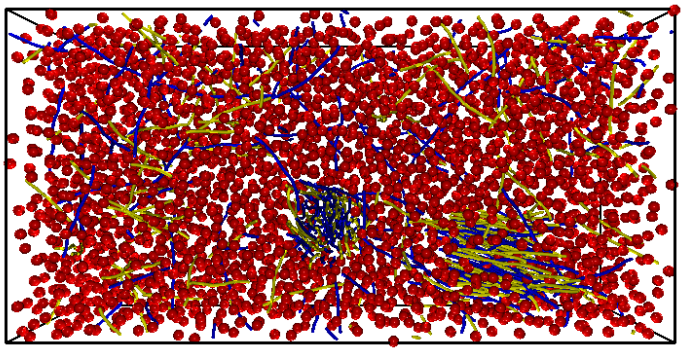

Figure 6.24: A snapshot of a medium rod/sphere system with a density $\rho = 2.0$ at $t = 9000$, $n_{rods} : n_{sphere} = 1 : 9$.

phase is formed, where the rod layers are no longer parallel to each other but tilt at a certain angle. In a system where the spherical particles are dominant, the rods tend to aggregate into small bundles where a phase separation is observed (see Fig.(6.27)).

At a density $\rho = 3.0$, an ordered rod phase can be observed when the number of spheres is small. The spherical particles are well dispersed along the boundaries of the rod layers. The rods form a well-defined layer structure as the whole rod-sphere system forms a lamellar phase (see Fig.(6.28)). These phase behaviour can also be observed in some higher DPD density (up to $\rho = 4.0$) systems.

We also carry out our simulation with a DPD density of $\rho = 5.0$, where such high density results in a phase separation. Even inside the rod-rich regime, the layered structures have disappeared, as shown in Fig. (6.29) and Fig. (6.30). To certain extent, this phase behaviour also proves the previous assumption that with increasing DPD density, a pure rod system goes isotropic - nematic - smectic - nematic -isotropic phase transition.

These phases have been observed experimentally by Adams et. al [15]. In their experiment, spherical polymer molecules such as polyethylene oxide (PEO) or polystyrene latex (PS) are added into the suspension of fd virus (rod-like molecule) in isotropic or nematic phases. At low system densities, when a low concentration of small spheres (diameter of the spheres are on the order of the rods) are added into the pure rod nematic phase, an isotropic and nematic bulk phase separation is observed. When more spheres are added in the nematic rod system, the spheres tend to assemble into columns along the rods' length. As the concentration of the spheres goes higher, the columns disappear while layered structure (lamella phase) of rods and spheres form. The lamella phase is also observed with high system density and a high concentration of rods in the experiment. We have also observed the lamella phase in our simulation. However, in their experiments, they have much bigger spheres and the rods have a much higher aspect ratio. It should be pointed out that in their experiments, the columnar phase can only be observed with sphere diameter in a certain range [15]. The columnar is not observed in our simulation due to two possible reasons: 1) Our sphere molecules have orientational defects, which may result in the impossibility of ever forming a columnar phase; 2) Our sphere molecules are too small.

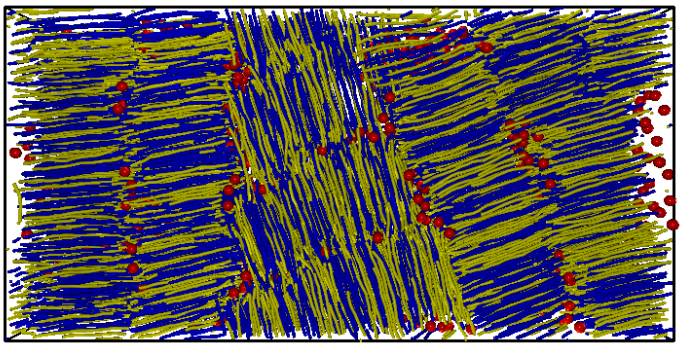

Figure 6.25: A snapshot of a medium rod/sphere system with a density $\rho = 2.5$ at $t = 9000$, $n_{rods} : n_{sphere} = 9 : 1$, rod molecules form blocks.

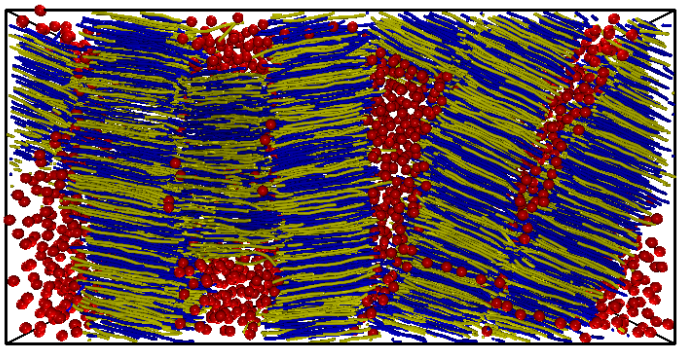

Figure 6.26: A snapshot of a medium rod/sphere system with a density $\rho = 2.5$ at $t = 9000$, $n_{rods} : n_{sphere} = 7 : 3$, tilted layered structure.

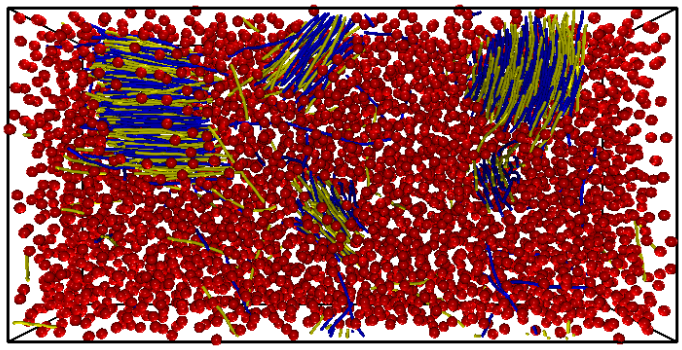

Figure 6.27: A snapshot of a medium rod/sphere system with a density $\rho = 2.5$ at $t = 9000$, $n_{rods} : n_{sphere} = 1 : 9$, rod bundles dissolved in sphere molecules.

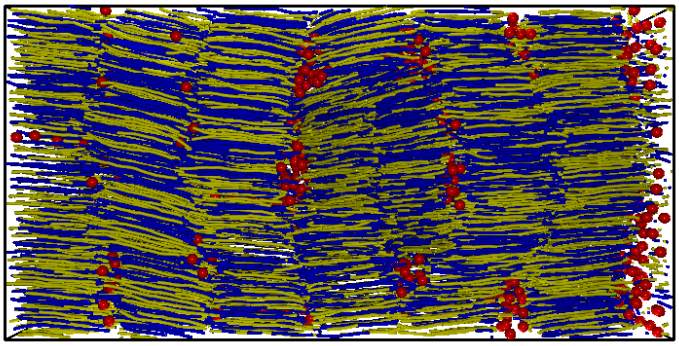

Figure 6.28: A snapshot of a medium rod/sphere system with a density $\rho = 3.0$ at $t = 9000$, $n_{rods} : n_{sphere} = 9 : 1$, a good smectic/lamellar phase.

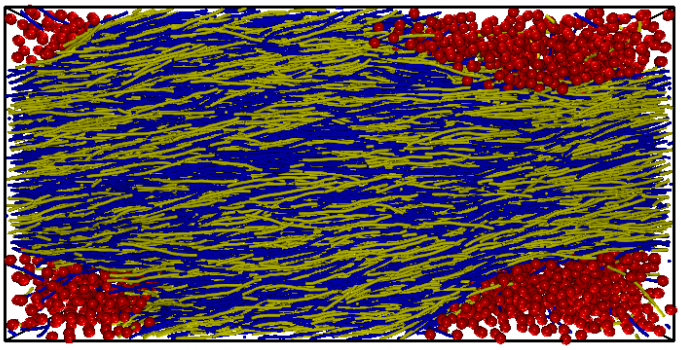

Figure 6.29: A snapshot of a medium rod/sphere system with a density $\rho = 5.0$ at $t = 9000$, $n_{rods} : n_{sphere} = 8 : 2$, a phase separation can be observed.

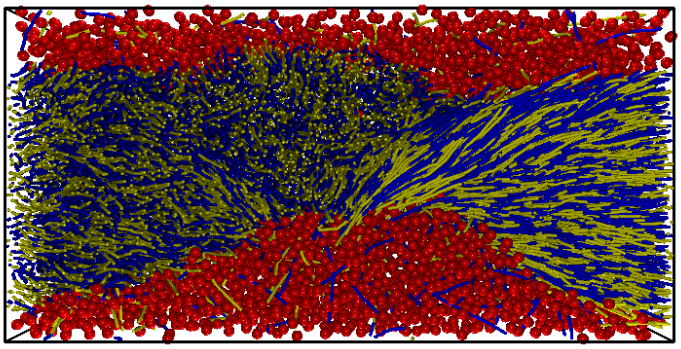

Figure 6.30: A snapshot of a medium rod/sphere system with a density $\rho = 5.0$ at $t = 9000$, $n_{rods} : n_{sphere} = 6 : 4$.

6.5 Simulation of Spider Silk Fibroins

DPD is widely used in the study of surfactants and other materials with different hydrophobicities in solutions. One big advantage of a DPD study is that DPD can simulate water particles quite well. Groot and Warren [1] have found a good DPD relation between the density of the particles and the repulsive parameter, which maps the compressibility of water particles very well. With this context, DPD can be used to simulate polymers in aqueous solution with a good description of the water.

Jin and Kaplan [8] have proposed a model for the formation of spider silk based on experimental observations. In their model, a silk fibroin molecule consists of 13 segments, of which 7 are hydrophilic and 6 are hydrophobic. As shown in Fig.(6.31), the hydrophobic and the hydrophilic segments are arranged in an alternating way which is like an alternating diblock copolymer.

In Fig.(6.31), the yellow segments represent the hydrophobic part while the blue segments represent the hydrophilic part. As shown on the top left corner of Fig.(6.31), the length of each segment is distinctive. This is a possible reason as to how the molecules can form a hydrophilic outer shell for the fibroin and multiple molecules aggregate inside the shell. A globule is thus formed at high fibroin concentration. Experimentally, Jin and Kaplan use a fibroin and polyethylene oxide (PEO) blend in aqueous solution to reproduce and validate their proposition. Microscopic photographs show that their proposed process is likely to be occurring in the formation of the real spider silk.

In our study, we try to use an alternating diblock copolymer to represent the silk fibroin molecule. The copolymer consists of one hydrophobic segment and one hydrophilic segment (one blue and one yellow segment as in Fig.(6.31)). Since the spider fibroin is long (13 segments), we try to reduce the length of the chain, just focusing on the relatively short chains. The hydrophobic segment (denoted as 'o') contains 8 DPD particles and the hydrophilic segment (denoted as 'x') contains 8 DPD particles. We first start our simulation by constructing the chain with only one hydrophobic segment and one hydrophilic segment ('ox') in water (denoted as 'w'). The DPD density is chosen to be $\rho = 3.0$ with $a_{oo} = a_{xx} = a_{ww} = 25, \gamma = 4.5$, corresponding to the aqueous solution. The favoured 'xw' interaction is set through $a_{xw} = 0$ while the unfavoured 'ow' interaction is set through $a_{ow} = 50$. The repulsive parameter for

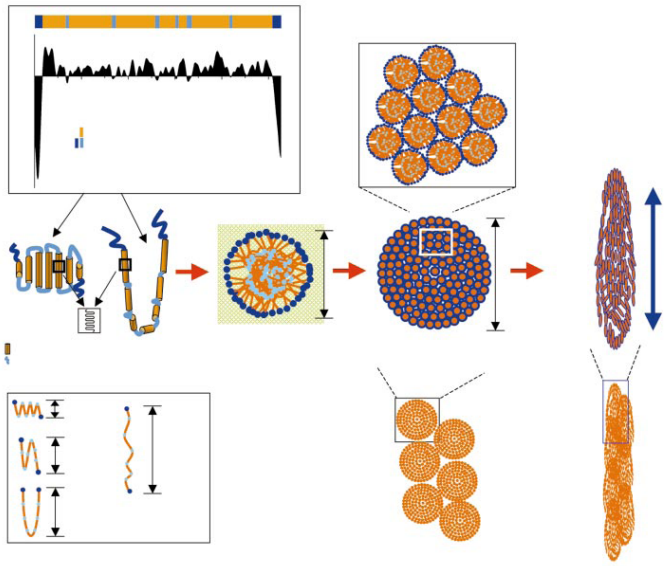

Figure 6.31: The spider silk formulation propose by Jin and Kaplan[8].

'ox' pair is set as $a_{ox} = 30$. The elastic spring constants between the chained particles are $k^{ox}_{spring} = k^{xx}_{spring} = k^{oo}_{spring} = 128$. The equilibrium distance is $r^{ox}_0 = r^{oo}_0 = r^{xx}_0 = 0.5$. We use a cubic box for the simulation where the length of the box is $L = 40$ and the time step is chosen $\Delta t = 0.02$.

In the simulation, we try to vary the proportion of the copolymer with respect to the water content. In addition, we also tune some of the parameters which will be discussed below.

We start the simulation with the number proportion of the copolymer to be 0.1%, with an increment of 0.1% till 0.9%. The copolymer will form micelles inside the solution. Within our density region, the increase in the proportion does not change the formation of the micelles. As shown in Fig. (6.32), the hydrophobic particles form the core of the micelles, leaving the hydrophilic particles trying to wrap them up. Since both the 'ox' and 'ow' interactions are less favoured, the hydrophilic particles are not really closely covering the hydrophobic part. There is some free water around the micelles. If we apply the mixing rule, the enthalpy gain by forming the 'ox' pair is approximately to

$$\begin{aligned} \Delta H_{mix} &= H_{ox} - \frac{1}{2}\left(H_{ow} + H_{xw}\right) \\ &\sim 30 - 50/2 = 5 > 0 \end{aligned} \tag{6.5.1}$$

Therefore the formation of the 'ox' pairs is not favoured. This gives a possible reason why the

'x' segments are moving into the water phase instead of the micelles.

As we increase the hydrophobicity of the 'x' particles by setting $a_{xw} = 15$ and further $a_{xw} = 25$, where we still call the 'x' segment hydrophilic, the size of the micelles changes. In the case of $a_{xw} = 25$, obviously the 'ox' interaction is more favoured than forming 'ow' + 'xw' interfaces. As a result, more 'o' segments tend to aggregate to form the core of the micelle, while 'x' segments are trying to cover the surface of the micelles, blocking the contact between water and the hydrophobic particles. Due to this reason, the micelle size is significantly larger than the previous case, as shown in Fig. (6.34). Since the 'x' segments cannot fully cover the surface area of the hydrophobic core, the size of the micelle is a balance between the number of 'ow' pairs on the surface of the core and chain dimension.

We also add some stiffness to the hydrophobic segments, where $k_{bend} = 128, \phi_0 = 0$. The chain stiffness puts some extra order for the 'o' segments to form the hydrophobic core for the micelles. The stiff segments tend to align in a parallel way which increases the 'oo' contacts and therefore attracts more chain molecules to form a micelle core, as shown in Fig. (6.35).

Our next step is to test the effect brought in by the polymerisation. The model we construct consists of six alternating segments, of which three are hydrophobic and the other three are hydrophilic. Each segment consists of 6 particles. Therefore the full chain can be denoted as 'oxoxox'. Since the chain is significantly longer, we re-adjust the box length to $L = 60$.

As the chain gets longer, the chain itself will fold to form the micelle core. In addition, the micelles are no longer dispersed all over the box but tend to form a stable structure at the centre of the box(Fig. (6.36)). As the repulsive parameter for 'xw' pair increases to $a_{xw} = 25$, the micelles come together and forms a hollow shell structure, as shown in Fig. (6.37). This possibly indicates that as the chain gets longer, the micelles tend to get closer to each other in order to get rid of unfavoured 'ow' interaction by sharing the hydrophilic outer layer of the micelles. Especially when the hydrophilic outer layer cannot fully cover the hydrophobic core, this sharing behaviour is more likely to happen. This also suggests that by carefully choosing the interaction parameters and the length of each segment, it is very likely that the micelles can form the globule as described by Jin and Kaplan.

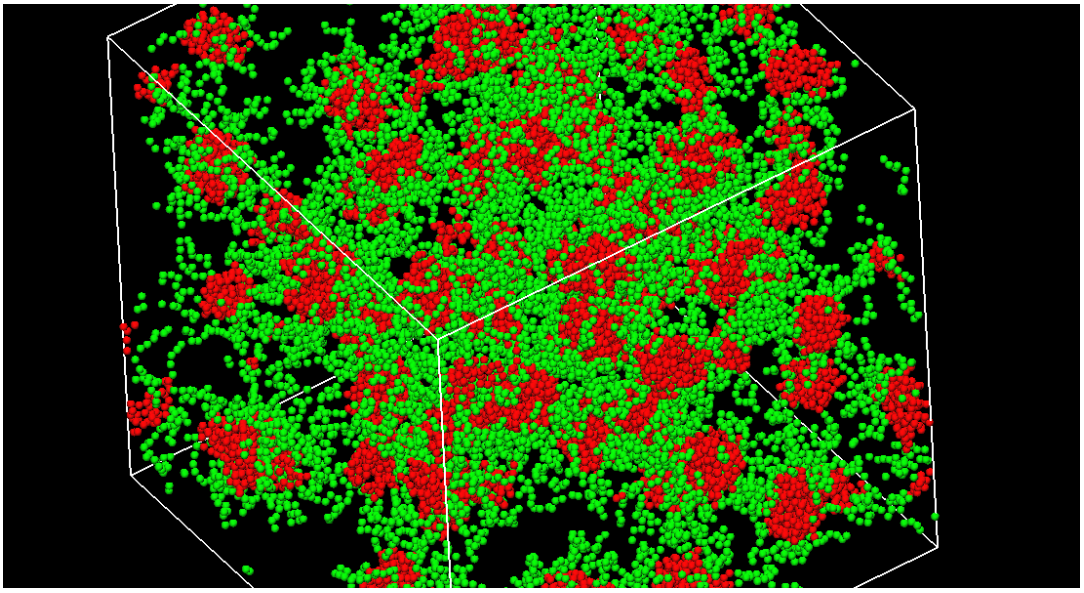

Figure 6.32: A snapshot of the micellation behaviour of 'ox' chains after $t = 5000$, n_{chain} : $n_{water} = 8 : 992$ and $a_{xw} = 0$. The red particles are hydrophobic and the green particles are hydrophilic, water molecules are not displayed.

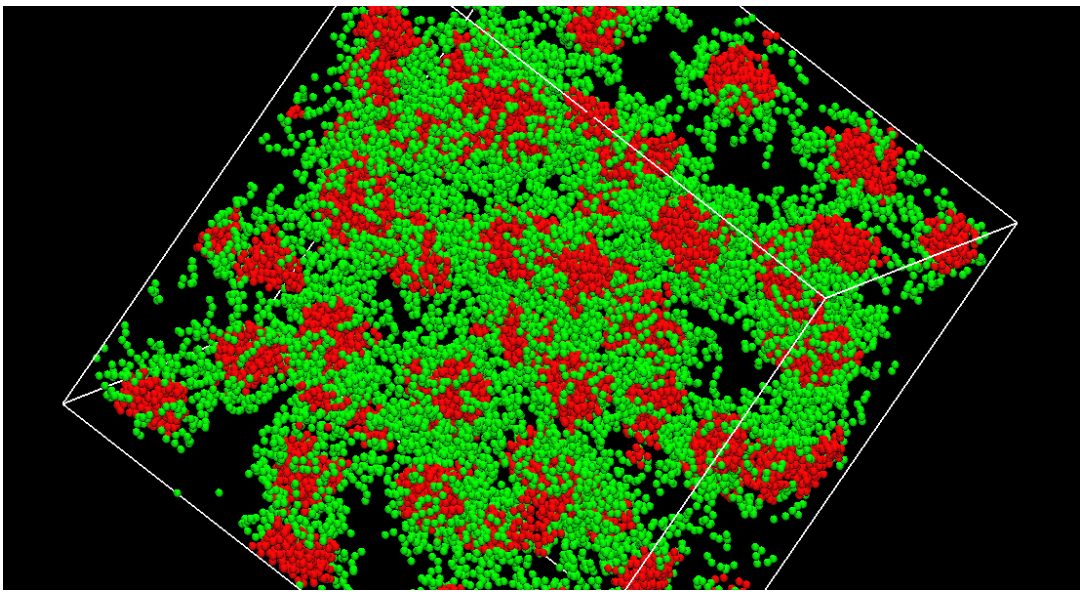

Figure 6.33: A snapshot of the micellation behaviour of 'ox' chains at $t = 5000$, n_{chain} : $n_{water} = 8 : 992$ and $a_{xw} = 15$. The red particles are hydrophobic and the green particles are hydrophilic, water molecules are not displayed.

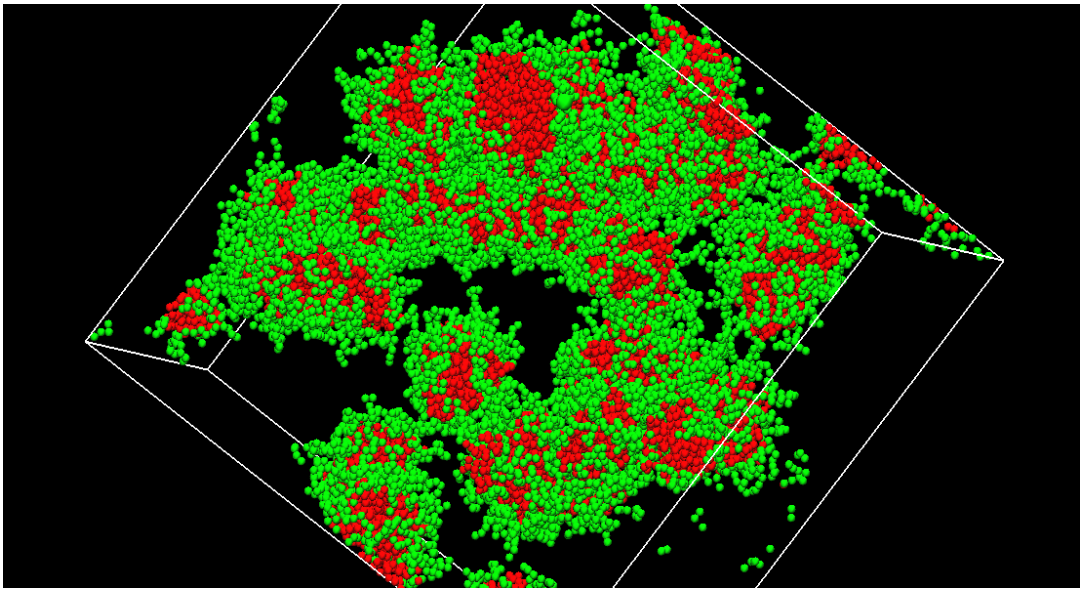

Figure 6.34: A snapshot of the micellation behaviour of 'ox' chains at $t = 5000$, n_{chain} : $n_{water} = 8 : 992$ and $a_{xw} = 25$. The red particles are hydrophobic and the green particles are hydrophilic, water molecules are not displayed.

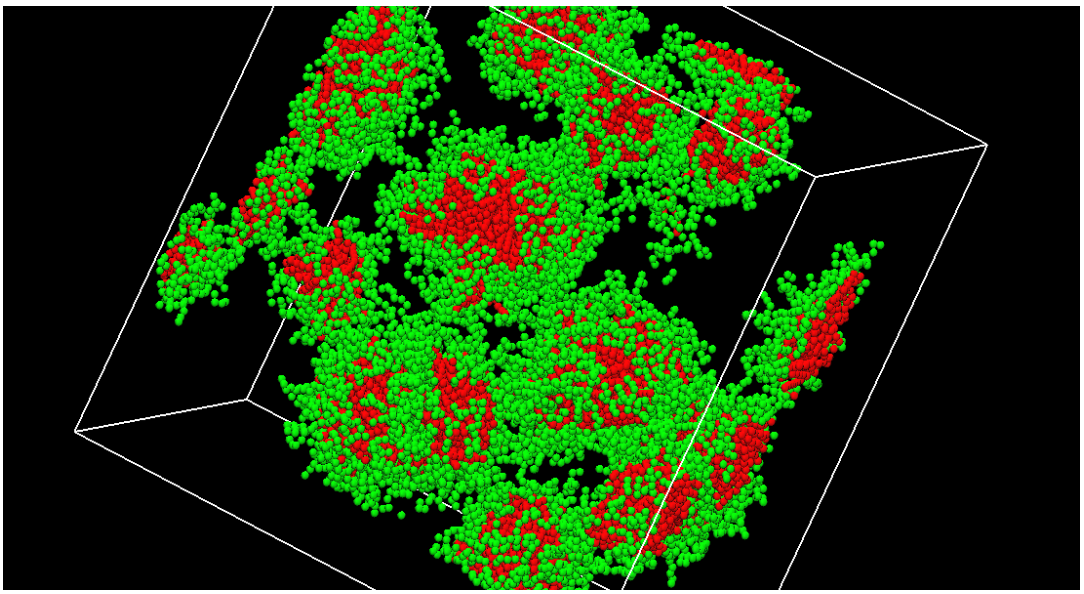

Figure 6.35: A snapshot of the micellation behaviour of stiff 'ox' chains at $t = 3000$, n_{chain} : $n_{water} = 8 : 992$ and $a_{xw} = 25$. The red particles are hydrophobic and the green particles are hydrophilic, water molecules are not displayed.

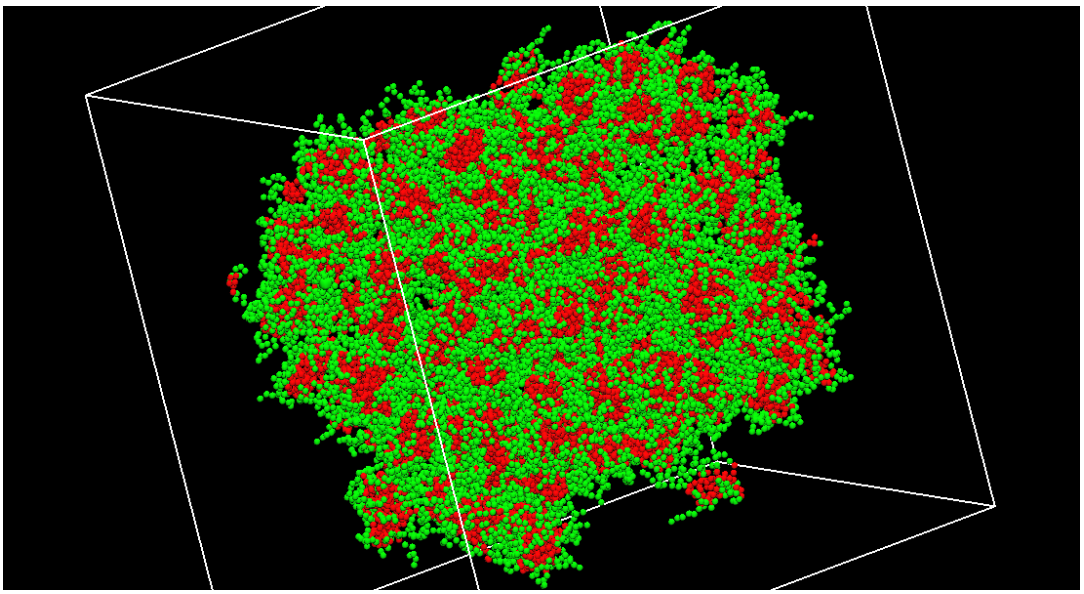

Figure 6.36: A snapshot of 'oxoxox' chains at $t = 3000$, $n_{chain} : n_{water} = 3 : 997$ and $a_{xw} = 0$. The red particles are hydrophobic and the green particles are hydrophilic, water molecules are not displayed.

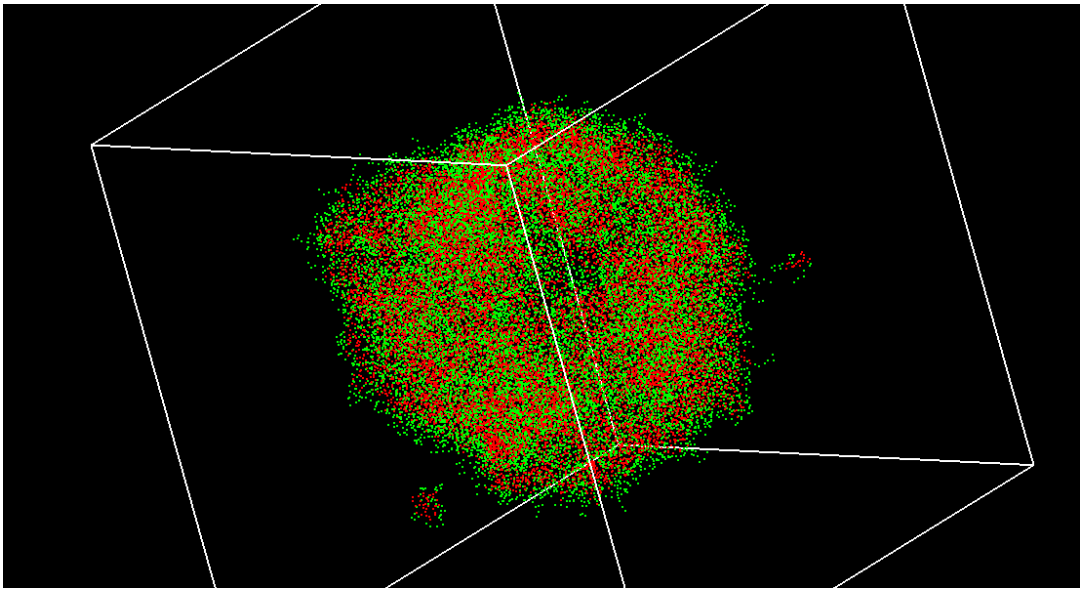

Figure 6.37: A snapshot of 'oxoxox' chains at $t = 3000$, $n_{chain} : n_{water} = 3 : 997$ and $a_{xw} = 25$. Particles are only displayed as dots to see the hollow structure inside. The red dots are hydrophobic and the green dots are hydrophilic, water molecules are not displayed. The black in the centre shows the area where much less particles appear.

6.6 Conclusion

In this section, we use dissipative particle dynamics (DPD) to simulate multiple systems. We start from a pure rod system to study its liquid crystal phases. For short rods, the system goes from an isotropic phase to a nematic phase when the density increases. But if the system density goes beyond a certain value, the ordered nematic phase becomes unstable and the system goes back to an isotropic phase. If the aspect ratio of the rods is greater than a certain critical value, we can see a clear phase transition from isotropic to nematic and to a further layered structure. The layered structure is analogous to a tilted smectic phase but the directors of different layers are perpendicular to each other. Unlike the hard rods or spherocylinders, as we further increase the system density (the same as increasing the system pressure), again the long rods system goes from an ordered structure back to isotropic. Due to the soft nature of the DPD particles, this layered/blocked structure was not observed in the hard spherocylinder systems. This suggests that, experimentally, a well-ordered structure might form in aqueous solution if we carefully use chained molecules with a soft repulsive potential.

Secondly, we simulate a rod/sphere mixture. The presence of the sphere molecules brings extra mobility to the rod molecules and therefore helps the phase transition. The rods start from an isotropic phase. At a higher DPD density, the system undergoes an isotropic - nematic transition. As the proportion of sphere molecules increases, the rods form a layered structure just like the smectic phase. However, the sphere molecules stay at the boundary of the rod layers. The boundary of the rod layers may not be well-defined depending on the composition of the rods and spheres. On the other hand, with high rods composition, the layers may align perpendicular to each other to form blocks. With a proper composition of rods and spheres, a lamella phase can be observed where the boundaries of the rod layers are parallel to each other and spheres are dispersed between the boundaries. By increasing the sphere composition, the lamella phase will be deformed and the rod layers tilt. If the DPD density goes very high, the layered structure disappears and we expect a phase separation for rods and spheres to occur, where the rods form an isotropic/nematic phase. These results give a good indication that small spherical particles play the role of a lubricant among rod-like molecules. The addition of spherical paricles may not result in a phase separation but may help the system to form a stable liquid crystal phase/structure. Soft particles exhibit more liquid crystal phases than the hard

objects. This might be tested further in experiments in the future.

In the last part of the simulation work, we try to simulate the formation of spider silk fibroin. The hydrophobic and hydrophilic diblock copolymer will micellise in water solution. The micelle has a hydrophobic core with a hydrophilic outer layer in order to minimize the water-hydrophobic contact. The hydrophobicity of the particles as well as the stiffness of the hydrophobic segments will affect the size of the micelles. As the number of blocks in the chain structure increases, the hydrophobic parts are likely to fold to form the cores of the micelles. Another effect brought by increasing the number of blocks is that the micelles tend to share their hydrophilic outer layers to form a globule-like shell. In order to compare simulation results with experiments, it is also important to study how the length of each segment of the molecule affects the formation process.

6.7 References

[1] R.D. Groot and P.B. Warren. “Dissipative particle dynamics: Bridging the gap between atomistic and mesoscopic simulation”. In: *Journal of Chemical Physics* 107 (1997), pp. 4423–4435. See pp. 103, 105, 106, 129.

[2] R.P. Carney et al. “Size limitations for the formation of ordered striped nanoparticles”. In: *JACS Communication* 130 (2008), pp. 798–799. See p. 103.

[3] A. AlSunaidi, W.K. den Otter, and J.H.R. Clarke. “Liquid-crystalline ordering in rod-coil diblock copolymers studied by mesoscale simulations”. In: *Philosophical Transactions: Mathematical, Physical and Engineering Sciences* 362 (2004), pp. 1773–1781. See p. 103.

[4] P. Prinsen, P.B. Warren, and Michels. M.A.J. “Mesoscale simulations of surfactant dissolution and mesophase formation”. In: *Phys. Rev. Lett.* 89 (2002), p. 148302. See p. 103.

[5] C.R. Iacovella, M.A. Horsch, and S.C. Glotzer. “Local ordering of polymer-tethered nanospheres and nanorods and the stabilization of the double gyroid phase”. In: *The Journal of Chemical Physics* 129 (2008), p. 044902. See p. 103.

[6] M.A. Horsch, Z. Zhang, and S.C. Glotzer. “Self-assembly of Laterally-Tethered Nanorods”. In: *Nano Letters* 6 (2006), pp. 2406–2413. See p. 103.

[7] D.L. Cheung et al. “Computer simulation of liquid and liquid crystals”. In: *Computer Physics Communications* (2008), pp. 61–65. See p. 103.

[8] H. Jin and D.L. Kaplan. “Mechanism of silk processing in insects and spiders”. In: *Nature* 424 (2003), pp. 1057–1061. See pp. 103, 129, 130.

[9] P. Espanõl and P.B. Warren. “Statistical Mechanics of Dissipative Particle Dynamics”. In: *Europhyiscs Letters* 30 (1995), pp. 191–196. See p. 105.

[10] P. Espanõl and P.B. Warren. “Statistical properties of Dissipative Particle Dynamics”. In: *Europhys. Lett.* 30 (1995), p. 191. See p. 105.

[11] M.P. Allen. “Simulations using hard particles”. In: *Philosophical Transactions: Mathematical, Physical and Engineering Sciences* 344 (1993), pp. 323–337. See p. 106.

[12] S. Chandrasekhar. *Liquid Crystals*. Cambridge University Press, 1994. See p. 107.

[13] G. Cinacchi and L. de Gaetani. “Diffusion in the lamellar phase of a rod-sphere mixture”. In: *Journal of Chemical Physics* 131 (2009), p. 104908. See p. 118.

[14] L. Onsager. “The effects of shape on the interaction of colloidal particles”. In: *Annals of the New York Academy of Science* 51 (1949), pp. 627–659. See p. 118.

[15] M. Adams et al. “Entropically driven microphase transition in mixtures of colloidal rods and spheres”. In: *Nature* 393 (1998), pp. 349–352. See pp. 118, 125.

[16] D Antypov and D.J. Cleaver. “Orientational and phase-coexistence behavior of hard rod-sphere mixtures”. In: *Chemical Physics Letters* 377 (2003), pp. 311–316. See p. 118.

[17] T. Koda, M. Numajiri, and S. Ikeda. “Smectic-A Phase of a Bidisperse System of Parallel Hard Rods and Hard Spheres”. In: *Journal of the Physical Society of Japan* 65 (1996), pp. 3551–3556. See p. 118.

CHAPTER

SEVEN

FUTURE WORK

In this thesis, Wertheim's association theory has been used to treat the strong short-range attraction in an electrolyte system. With one association site, our theory still suffers from a lack of solution for the hypernetted chain (HNC) closure for the reference fluid in the dense liquid phase. It is possible to instead use the mean spherical approximation (MSA) closure rather than HNC. One problem is that in the MSA, there is no direct analytical expression for the Helmholtz free energy. Instead we have to calculate the internal energy U and do an integral over temperatures to get the Helmholtz free energy. The calculation will be quite tedious but it can be an alternative way of treating the electrolyte system. On the other hand, MSA can be solved analytically for the full-range Coulombic potential by using Baxter's method. It is therefore possible that by choosing an appropriate splitting potential, an analytical solution may be found for the reference fluid. In this case, an analytical expression for the total Helmholtz free energy should also be a possibility. A further detailed analysis for the choice of the splitting potential is thus approachable. This will definitely be helpful in giving a better understanding about the association theory as well as the electrostatic interactions in the electrolyte and polyelectrolyte solutions.

The association theory may also be useful in describing polyelectrolytes. With a proper choice of the splitting parameter, the HNC can give a good description of the reference fluid with a split potential. Therefore a polyelectrolyte chain can be described as a big polymer chain with multiple association sites on it. The additional energy of forming such a polymer chain can be calculated by the method we use in the SAFT. The $g(\sigma)$ value can be obtained from the HNC calculation for the reference fluid. This approach should also be possible using the MSA closure (which might be less accurate, however).

Dissipative particle dynamics (DPD) has the great advantage of permitting rapid equilibration compared to conventional simulations of hard-body models. For the study of liquid crystalline phase transition, however, a future development will be better to use an NPT ensemble instead of an NVT. In an NVT-ensemble, one not only may find phase co-existence but also the liquid crystal phase will be affected by the fixed box dimensions. For instance, a smectic phase might be deformed simply because of the equilibrium layer spacing is incommensurate with the box dimensions. Therefore, in the future, an NPT version of the DPD code should be developed. With an NPT ensemble, the dimension of the box can be varied, so ordered phases may be more easily accommodated. It also helps to better define the boundary of the liquid crystal phases for the soft repulsive particles. The theoretical expressions for the DPD in the NPT ensemble should also be studied. In addition, a further development on the external force field should be applied to the DPD system. This should be helpful in dealing with shear force and other external interactions which are worthy of study. As a result, the next step of the formation of spider silk fibres can be simulated.

APPENDIX

A

NUMERICAL ITERATION METHODS

A.1 Ng's Numerical Iteration Method

Consider the equation

$$f = Af \tag{A.1.1}$$

where $f(x)$ is any function of real variables and A is a non-linear operator defined in the functional space.

An iterative process can be written as

$$f_{n+1} = Af_n \tag{A.1.2}$$

where the subscript n indicates the n-th iteration. If the sequence f_n converges uniformly, the $\lim_{n\to\infty} f_n$ is the solution of Eq. (A.1.1). A standard procedure to do the iteration is

$$f_{n+1} = \alpha A f_n + (1-\alpha) f_n \tag{A.1.3}$$

The parameter α is determined empirically in order to achieve fast convergence. The convergence can be speeded up by using Broyle's extrapolation method[1].

A faster converging process is proposed by Ng[2]. Define the following

$$g_n \equiv Af_n \tag{A.1.4}$$

$$d_n \equiv g_n - f_n = (A-1)f_n \tag{A.1.5}$$

For $n \geq 3$, the $(n-2)$th, $(n-1)$th and nth iterations are known. Therefore, it is reasonable to consider

$$\bar{f} = (1 - c_1 - c_2)f_n + c_1 f_{n-1} + c_2 f_{n-2} \tag{A.1.6}$$

and choose the optimal value for c_1 and c_2 in order that $\bar{f}$ is the solution of Eq. (A.1.1). In the case when the operator A is linear, the optimal choice is

$$A\bar{f} = (1 - c_1 - c_2)g_n + c_1 g_{n-1} + c_2 g_{n-2} \tag{A.1.7}$$

$$\Delta = ||A\bar{f} - \bar{f}|| = ||d_n - c_1 d_{01} - c_2 d_{02}|| \tag{A.1.8}$$

where

$$d_{01} = d_n - d_{n-1} \tag{A.1.9}$$

$$d_{02} = d_n - d_{n-2} \tag{A.1.10}$$

The parameter c_1 and c_2 corresponding to the minimum Δ^2 can be obtained by solving simultaneously

$$\begin{aligned}(d_{01}, d_{01})c_1 + (d_{01}, d_{02})c_2 &= (d_n, d_{01}),\\ (d_{01}, d_{02})c_1 + (d_{02}, d_{02})c_2 &= (d_n, d_{02}),\end{aligned} \tag{A.1.11}$$

where (u, v) is the inner product defined by

$$(u, v) = \int u(x)v(x)\,dx \tag{A.1.12}$$

The $(n+1)$th iteration is then given as

$$f_{n+1} = (1 - c_1 - c_2)g_n + c_1 g_{n-1} + c_2 g_{n-2} \tag{A.1.13}$$

Generally the operator A is nonlinear, but we may approximate A by a different linear operator for every iteration step n. To further speed up the convergence, instead of using only two parameters c_1 and c_2, we may use more parameters. In this study, six parameters are used. The empirical parameter α is chosen to be 0.2.

A.2 References

[1] A.A. Broyles. “Radial distribution functions from the Born-Green Integral Equation”. In: *The Journal of Chemical Physics* 33 (1960), p. 458. See p. 141.

[2] K.C. Ng. “Hypernetted chain solutions for the classical one-component plasma up to Γ=7000”. In: *The Journal of Chemical Physics* 61 (1974), pp. 2680–2689. See p. 142.

APPENDIX

B

DATA POINTS FOR PHASE SEPARATION BY ASSOCIATION THEORY

In this section, we list some of the phase coexistance points given by the association theory for various association sites.

Table B.1: Phase equilibrium data of 1-site association theory for the restricted primitive model, ρ_1 is calculated using the 1-site association theory, ρ_2 is calculated using mean spherical approximation.

T^*	ρ_1	ρ_2	P^*	μ^*
0.048543689	0.006213	0.231724	0.003278	-12.3876
0.048076923	0.005662	0.235008	0.003075	-12.5093
0.047619048	0.005205	0.238255	0.002897	-12.6314
0.046948357	0.004636	0.243084	0.002639	-12.8149
0.046296296	0.004160	0.247867	0.002415	-12.9991
0.045454545	0.003631	0.254175	0.002148	-13.2459
0.044843049	0.003291	0.258830	0.001969	-13.4312
0.044247788	0.002990	0.263447	0.001807	-13.6174
0.043478261	0.002639	0.269479	0.001612	-13.8667
0.042918455	0.002408	0.276412	0.001479	-14.0543
0.042372881	0.002198	0.278367	0.001359	-14.2425
0.041666667	0.001951	0.284200	0.001213	-14.4942
0.041152263	0.001784	0.288475	0.001113	-14.6837
0.040650407	0.001633	0.292693	0.001022	-14.8738
0.040000000	0.001451	0.298264	0.000911	-15.1280

Table B.2: Phase equilibrium data of 2-sites association theory for the restricted primitive model.

T^*	ρ_1	ρ_2	P^*	μ^*
0.072254335	0.06440	0.07530	0.002565	-10.1164
0.072202166	0.06323	0.07074	0.002563	-10.1217
0.071942446	0.06125	0.08024	0.002554	-10.1483
0.071428571	0.05790	0.08430	0.002536	-10.2016
0.068965517	0.0496	0.1025	0.002457	-10.4707
0.066666667	0.04528	0.1166	0.002390	-10.7445
0.062500000	0.0398	0.14175	0.002285	-11.3051
0.058823529	0.0369	0.1654	0.002205	-11.8816
0.055555556	0.0346	0.1878	0.002143	-12.4724
0.052631579	0.0333	0.2094	0.002090	-13.0759
0.050000000	0.03192	0.2300	0.002045	-13.6907
0.047619048	0.03091	0.2493	0.002004	-14.3157
0.045454545	0.03007	0.2678	0.001967	-14.9499
0.043478261	0.02950	0.2857	0.001931	-15.5924

Table B.3: Phase equilibrium data of 3-sites association theory for the restricted primitive model.

T^*	ρ_1	ρ_2	P^*	μ^*
0.05899705	0.05072	0.06288	0.0008541	-12.6225
0.058823529	0.04730	0.06778	0.0008479	-12.6548
0.057142857	0.03490	0.09233	0.0007918	-12.9405
0.055555556	0.02968	0.11150	0.0007450	-13.2305
0.052631579	0.02360	0.14284	0.0006735	-13.8218
0.050000000	0.02040	0.17110	0.0006243	-14.4266
0.047619048	0.01848	0.19700	0.0005903	-15.0431
0.045454545	0.01687	0.22160	0.0005681	-15.6699

Table B.4: Phase equilibrium data of 4-sites association theory for the restricted primitive model.

T^*	ρ_1	ρ_2	P^*	μ^*
0.055096419	0.054222	0.056218	0.000309953	-14.0691
0.054945055	0.044703	0.066223	0.000304792	-14.0983
0.054644809	0.038779	0.076102	0.000294797	-14.1570
0.054054054	0.032192	0.088467	0.000276075	-14.2747
0.052631579	0.023635	0.114380	0.000235803	-14.5718
0.051282051	0.018813	0.134042	0.000203315	-14.8724
0.050000000	0.015650	0.151550	0.000177082	-15.1763
0.048780488	0.013350	0.167435	0.000155799	-15.4833
0.047619048	0.011627	0.182418	0.000138538	-15.7931
0.046511628	0.010276	0.196770	0.000124513	-16.1054
0.045454545	0.009024	0.209490	0.000113099	-16.4202
0.043478261	0.007703	0.233589	0.000096417	-17.0567
0.041666667	0.006695	0.255590	0.000085589	-17.7104

Table B.5: Phase equilibrium data of 5-sites association theory for the restricted primitive model.

T^*	ρ_1	ρ_2	P^*	μ^*
0.05740528	0.0559	0.0571	0.000100373	-14.4194
0.05730659	0.0481	0.0647	0.000098058	-14.4369
0.05714286	0.0420	0.0721	0.000094368	-14.4660
0.05555556	0.02224	0.1074	0.000062504	-14.7597
0.05405405	0.01429	0.1284	0.000039251	-15.0571
0.05263158	0.009958	0.1487	0.000022662	-15.3575
0.05128205	0.007756	0.1649	0.000011083	-15.6611
0.05000000	0.004787	0.18104	0.000003633	-15.9676

Table B.6: Phase equilibrium data of 4-sites association theory for the 2:1 charge-asymmetric primitive model.

T^*	ρ_1	ρ_2
0.0427350	0.13016	0.1384
0.0423729	0.10850	0.17846
0.0416667	0.09770	0.19945
0.0409836	0.08758	0.21732
0.0400000	0.07889	0.2388
0.0390625	0.07374	0.25818
0.0384615	0.06953	0.2696
0.0370370	0.06350	0.29528
0.0357143	0.05944	0.3186

Table B.7: Phase equilibrium data of 4-sites association theory for the 3:1 charge-asymmetric primitive model.

T^*	ρ_1	ρ_2
0.034013605	0.2075	0.2725
0.033670034	0.1946	0.29053
0.033333333	0.1853	0.30228
0.032679739	0.17265	0.32912
0.031746032	0.16052	0.3571
0.03030303	0.149	0.394

Table B.8: Phase equilibrium data of 4-sites association theory for the $\lambda = 2$ size-asymmetric primitive model.

T^*	ρ_1	ρ_2
0.054347826	0.04289	0.051806
0.053956835	0.03618	0.073136
0.053571429	0.0351	0.077625
0.051724138	0.02475	0.108945
0.050000000	0.01875	0.130781

Table B.9: Phase equilibrium data of 4-sites association theory for the $\lambda = 4$ size-asymmetric primitive model.

T^*	ρ_1	ρ_2
0.051020408	0.03906	0.046875
0.050000000	0.02734	0.067188
0.047619048	0.01898	0.090625
0.045454545	0.01545	0.110938